Flow Analysis and Control in a Subsonic Inlet

by

Serge Tournier

Diplôme d'Ingénieur des Arts et Manufactures, École Centrale Paris, 2003
Diplôme d'Études Approfondies en Énergétique: Physique des Transferts et Combustion, École Centrale Paris, 2003

Submitted to the Department of Aeronautics and Astronautics
in partial fulfillment of the requirements for the degree of

Master of Science in Aeronautics and Astronautics

at the

MASSACHUSETTS INSTITUTE OF TECHNOLOGY

September 2005

© Massachusetts Institute of Technology 2005. All rights reserved.

Author ....
Department of Aeronautics and Astronautics
August 19th, 2005

Certified by ....
James D. Paduano
Principal Research Engineer
Thesis Supervisor

Accepted by ....
Jaime Peraire
Professor of Aeronautics and Astronautics
Chair, Committee on Graduate Students

MASSACHUSETTS INSTITUTE OF TECHNOLOGY
DEC 01 2005
LIBRARIES

ARCHIVES

Flow Analysis and Control in a Subsonic Inlet

by

Serge Tournier

Submitted to the Department of Aeronautics and Astronautics
on August 19th, 2005, in partial fulfillment of the
requirements for the degree of
Master of Science in Aeronautics and Astronautics

Abstract

S-duct inlets are commonly used on subsonic cruise missiles, as they offer a good compromise between compactness, low observability and aerodynamic performance. Though currently used S-ducts exhibit good performance in terms of distortion and pressure recovery at the AIP, the situation can degrade drastically when the inlet is put in off-design conditions, with the risk of compressor instabilities.

Flow control is considered as a promising way to maintain inlet efficiency in off-design flight conditions. Industrial interest for flow control techniques is therefore rising, and a need for their comparative evaluation has been expressed. In response to this need, an experimental setup has been designed and fabricated, and flow control experiments have been carried out at MIT, on the selected off-design case of forebody boundary layer ingestion.

The first set of experiments focused on the characterization of the inlet in a clean configuration. Then, a distortion device was added in order to simulate thick forebody boundary layer. This proved to have a strong detrimental effect on the inlet performance, as the separation bubble grew in size, the pressure recovery dropped down and the distortion level increased drastically. The selected flow control techniques were then implemented. The Vortex Generators, tried in different configurations, did improve the pressure recovery and significantly decrease the distortion level. They had a strong impact on the flow structure, delaying or even suppressing separation. Injection was done with Coanda-type injectors, upstream of the separation line. Steady injection led to significant improvement of the pressure recovery, which increased with increasing injection mass flow. Separation was eliminated at least for the highest injection mass flows. The distortion level decreased with increasing injection mass flow. Overall, the results also highlighted the importance of the secondary flows as a source of distortion and pressure recovery loss.

Thesis Supervisor: James D. Paduano
Title: Principal Research Engineer

Acknowledgments

First I would like to thank my advisor, Dr. James D. Paduano, for his guidance and his support. I am very grateful for his helpful insights and advice during the course of this experimental work. I would also like to thank Didier Pagan, from MBDA-France, for his kindness and constant motivation. Many thanks, also, to him and Yan Kergaravat for giving me the opportunity to work on this project.

I would like to thank Jack Costa, Viktor Dubrowski and James Letendre for always providing a helping hand, for their patience, valuable advice and kindness, and for always finding the solution and the right tool to solve all my problems (It's amazing what one can do with some epoxy resin and some aluminum tape). I am also thankful to the entire Gas Turbine Lab staff for their kindness.

I would like to thank my family back in France for their love and constant support. I would like to express my gratefulness to my parents, who taught me the value of a good education, and I would like to address a "spéciale dédicace" to my brother, Rayane, for all the time we spent on the phone rebuilding the world, or just trying to understand it, and last but far from the least, I would like to show all my love to my sister, Maude, who is going to make me an uncle some time in October. The eight wonder of the world will be spoiled, I swear.

Many thanks to all the people who made my stay at MIT such an unforgettable experience. Et puis on va continuer en Français, pour remercier tous les bouffeurs de grenouilles du MIT, de Cambridge ou d'alentours, pour les moments inoubliables (et c'est peu dire) que nous avons passés ensemble au cours de ces deux années. Alors sans ordre particulier: Thomas, Amandine, Jean-Marie, Jean-Baptiste, Jean-François, Richard, Pierre (Dakhel), Thierry, Pierre (Leroyer), François, Célia, Jérome, Camille, Claire, Gregory, Jeff, Théo, Henry, sans oublier la bande de marathoniens de Harvard: Adrien, Riadh et Guillaume ainsi que tout ceux que j'ai oubliés (ouf!). À bientôt sur Paname. Et je garde mes dernières pensées pour ma petite chérie, qui était tout simplement là, ce beau soir de septembre...

This work was fully funded by MBDA-France, under the supervision of Didier Pagan.

Contents

Abstract 3

Acknowledgements 5

Table of Contents 10

List of Figures 13

List of Tables 15

Nomenclature 17

1 Introduction 19
- 1.1 Background and motivation . . . 19
- 1.2 Prior work . . . 21
- 1.3 Research objectives . . . 23
- 1.4 Thesis outline . . . 24

2 Experimental Setup 27
- 2.1 Hardware . . . 27
  - 2.1.1 Facility . . . 27
  - 2.1.2 The transonic Inlet . . . 29
  - 2.1.3 The bellmouth . . . 32
  - 2.1.4 Parts fabrication . . . 35
  - 2.1.5 Operating range . . . 37
- 2.2 Instrumentation . . . 37
  - 2.2.1 Instruments . . . 38
  - 2.2.2 Traverser setup . . . 40
  - 2.2.3 Data acquisition . . . 40

2.3 System calibration 41
    2.3.1 Scani-valve calibration 41
    2.3.2 Bellmouth calibration setup 42
    2.3.3 The Venturi 43
    2.3.4 Bellmouth calibration curve 45
    2.3.5 Mass flow deduction 47
2.4 Data reduction 48
    2.4.1 Inlet operating conditions 48
    2.4.2 Inlet performance descriptors 49

3 Inlet Flow Characterization 53
3.1 Bare inlet: flow structure 53
    3.1.1 Flow structure in S-ducts 53
    3.1.2 Oil flow visualization 55
    3.1.3 Boundary layer separation 57
    3.1.4 Flow reattachment 60
    3.1.5 Secondary flows 61
    3.1.6 AIP flow properties 61
3.2 Bare inlet: CMF sensitivity 62
    3.2.1 Pressure recovery 62
    3.2.2 Pressure profile 63
    3.2.3 Separation bubble location 66
    3.2.4 Distortion 66
3.3 BLI configuration : flow structure 68
    3.3.1 Screen design 69
    3.3.2 Screen distortion characterization 71
    3.3.3 Oil flow visualization 72
    3.3.4 Separation location 74
3.4 BLI configuration: performance 75
    3.4.1 Pressure recovery 75
    3.4.2 Distortion 76

4 Control Implementation 79
4.1 Vortex Generators 79
    4.1.1 VG design 79

4.1.2 VG results 82
4.2 Injection 88
4.2.1 Injection setup 88
4.2.2 Injector blocks 90
4.2.3 Injection setup mass flow measurement 93
4.2.4 Steady injection results 95
4.2.5 Pulsed injection results 99
4.3 Control techniques comparisons 102

5 Conclusions **105**

A MBDA Inlet Geometric Details **115**

B MBDA Presentation **119**
B.1 History 119
B.2 Geographical situtation 120
B.2.1 In the world 120
B.2.2 In France 121
B.3 Activities 121
B.3.1 Anti-tank missiles 121
B.3.2 Anti-ship missiles 122
B.3.3 Ground-to-air missiles 122
B.3.4 Air-to-ground missiles 122
B.3.5 Air-to-air missiles 123
B.3.6 Nuclear missiles 123
B.3.7 Target vehicles 123
B.3.8 Other products 124
B.4 Key-figures 124

C DeLaval Compressor Run Sheet **127**

D Matlab Codes and Data Structure **133**
D.1 Data structure 133
D.2 data_treatment_BASELINE code 135
D.3 Bell_CMF code 138
D.4 distortion_descriptors code 138

D.5 make_map code 140

List of Figures

1-1 The Exocet MM40 Block 3 missile 19

2-1 Facility configuration 28
2-2 Test section 28
2-3 Inlet geometrical parameters 30
2-4 Inlet SLA parts 32
2-5 Bellmouth elliptical contraction 33
2-6 Bellmouth SLA part 33
2-7 Constant area duct SLA parts 34
2-8 SLA apparatus 35
2-9 Assembled SLA parts 36
2-10 The Instrumentation Can 39
2-11 The traverser setup 40
2-12 The bellmouth calibration setup 42
2-13 The Venturi tube 43
2-14 The bellmouth calibration curve 45
2-15 The bellmouth vena contracta 47
2-16 Bellmouth calibration check 48
2-17 Typical ring total pressure plot 50

3-1 Secondary flows in S-ducts 54
3-2 Boundary layer separation 55
3-3 Oil flow visualization results for the bare inlet configuration 56
3-4 Textbook “owl face of the second kind” separation structure [2] . . . 57
3-5 Oil flow visualization interpretation for the baseline case 57
3-6 Textbook 3d-view of the separation structure [1] 58
3-7 Textbook 3d-view of a boundary layer take off [1] 59

3-8 Textbook 3-D view of the reattachment structure [1] 60
3-9 Secondary flows 61
3-10 AIP total pressure map at $CMF = 1.67kg.s^{-1}$ for the baseline case . 62
3-11 AIP Pressure recovery as a function of CMF for the baseline case . . 63
3-12 Pressure profile along centerline for the baseline case 64
3-13 Inlet and bellmouth pressure profiles at choked conditions for the baseline case 65
3-14 Pressure and effective area profiles at separation in duct flows 66
3-15 AIP total pressure maps for the baseline case 67
3-16 AIP circumference static pressure for the baseline case 68
3-17 Circumferential distortion as a function of CMF for the baseline case 69
3-18 The distortion screen setup 70
3-19 Screen pressure recovery 71
3-20 Oil flow visualization results for the BLI configuration 72
3-21 Oil flow visualization interpretation for the BLI configuration 73
3-22 Textbook "owl face of the first kind" separation structure 73
3-23 Static pressure profiles for bare and "screen on" configurations 74
3-24 Pressure recovery for the bare and the "screen on" configurations . . 75
3-25 Circumferential distortion for the bare and the "screen on" configurations 76
3-26 AIP total pressure maps for the "screen on" case 77

4-1 The VGs in use 80
4-2 Counter- and co-rotating VG arrangements 81
4-3 Pressure recovery for the VG-controlled cases 82
4-4 Circumferential distortion for the VG-controlled cases 83
4-5 Pressure profiles at $CMF = 1.67kg.s^{-1}$ for the VG-controlled cases . 84
4-6 AIP total pressure maps for the VG-controlled cases 85
4-7 AIP circumference static pressure for the VG-controlled cases 86
4-8 Oil flow visualization results for the VG1-controlled case 87
4-9 The injection setup on test bench 88
4-10 CAD view of the rotary valve body [51] 89
4-11 CAD view of the rotary valve rotor [51] 90
4-12 CAD view of an injector [41] 90
4-13 CAD cross-sectional view of the injector mounted on the inlet wall . . 91
4-14 Injection angle 92

4-15 The variable area flowmeter 93
4-16 Pressure recovery as a function of steady injection mass flow 95
4-17 Circumferential distortion as a function of steady injection mass flow 97
4-18 AIP total pressure maps at $CMF = 1.67kg.s^{-1}$ for the steady injection-controlled cases 98
4-19 Pressure recovery and distortion results as a function of the injection mass flow for the pulsed injection-controlled cases 99
4-20 AIP total pressure maps at $CMF = 1.67kg.s^{-1}$ for the pulsed injection-controlled cases 100
4-21 Pressure recovery as a function of the injection feeding total pressure 101
4-22 Pressure recovery as a function of inlet mass flow for the VG- and injection-controlled cases 102
4-23 Circumferential distortion as a function of inlet mass flow for the VG- and injection-controlled cases 103

A-1 Trapezoidal entrance definition points 116
A-2 Centerlines definition points 116
A-3 CAD view of 6 intermediary slices of the MBDA inlet geometry . . . 118

B-1 Restructuring of the European Defence Industry 119
B-2 MBDA locations 120
B-3 The Eryx missile 121
B-4 The Exocet missile 122
B-5 The Aster missile 122
B-6 The AS30 LASER missile 122
B-7 The MICA-EM and MICA-IR missiles 123
B-8 The ASMP nuclear missile 123
B-9 The C-22 target vehicle 123
B-10 Counter-measure systems 124
B-11 MBDA main clients 124
B-12 The missile market and sales 125

List of Tables

2.1 Test conditions: throat Mach number, CMF and throat Reynolds number 37

4.1 The VG configurations tested 82
4.2 The injectors tested 92

A.1 Lower centerline definition points coordinates 116
A.2 Lower centerline definition points coordinates 117
A.3 Upper centerline definition points coordinates 117
A.4 Cross sectional area as a function of axial distance 117

Nomenclature

AIP	Aerodynamic Interface Plane
A_1	Inlet entrance section area, m^2
A_2	AIP area, m^2
CMF	Corrected Mass Flow, $kg.s^{-1}$
D	Inlet exit diameter, m
$DPCP_{avg}$	Circumferential distortion descriptor, $non-dimensional$
d_H	Hydraulic diameter of trapezoidal entrance, m
ΔY	Inlet entrance to exit vertical offset, m
IC	Instrumentation Can
L	Inlet entrance to exit planes distance, m
$\dot{m}$	Physical mass flow in inlet duct, $kg.s^{-1}$
p	Static pressure, Pa
P_{ref}	Reference pressure: $P_{ref} = 101\,327Pa$
P_{Te}	Area weighted average total pressure at the AIP, Pa
P_{T0}	Freestream total pressure, Pa
PAV_i	Total pressure average of IC ring i, $non-dimensional$
$PAVLOW_i$	Total pressure average of low total pressure region for ring i, $non-dimensional$
PR	Pressure Recovery, $non-dimensional$
s	Curvilinear coordinate along the inlet bottom centerline, m
SLA	Stereolitography
T_{ref}	Reference temperature: $T_{ref} = 288.17K$
T_{T0}	Free stream total temperature, K
VG	Vortex Generator
VGJ	Vortex Generator Jet
$_{th}$	Subscript for throat
$_1$	Subscript for entrance
$_2$	Subscript for exit

Chapter 1

Introduction

1.1 Background and motivation

Modern tactical aircraft, such as missiles, must be manoeuvrable for a wide range of flying conditions, without sacrificing performance. In the case of aircraft propelled by air-breathing engines, the propulsive system includes some form of inlet to condition the airflow before it reaches the compressor: its role is to slow down the incoming airflow, by converting as much of the airflow kinetic energy as possible into static pressure at the compressor face. Being the first element of the propulsive system, its efficiency is a critical element. Inlet efficiency is mainly set by its design, but can also be heavily affected by external conditions.

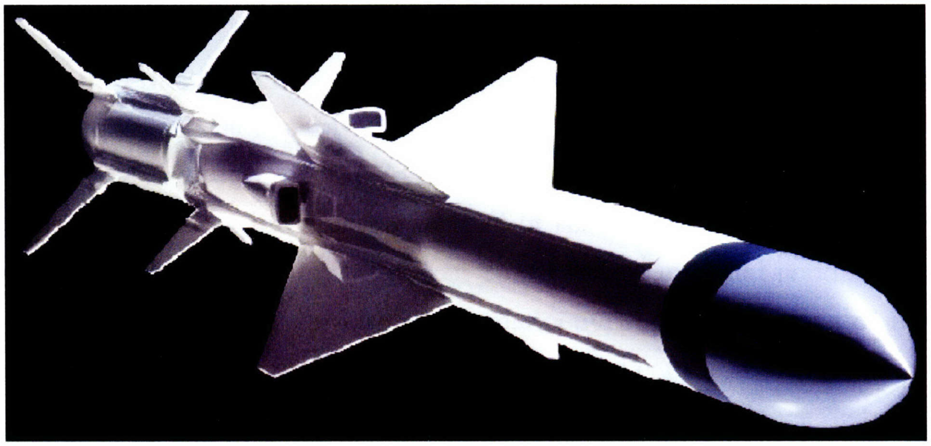

Figure 1-1: The Exocet MM40 Block 3 missile

In the case of transonic flight conditions, inlet design is driven by two sets of constraints:

- Aerodynamic constraints tend to optimize the shape of the inlet duct to get the best efficiency and reduce distortion at the compressor face. This leads to long shapes with low-curvature and slow variation in cross sectional area. The shape being fixed, the inlet is optimized for one particular flight condition, or is a matter of compromise between a few flight conditions.
- Tactical constraints shape the inlet so that the observability of the aircraft is reduced. This leads to a highly curved shape and strong variation in area, mainly in order to prevent direct view of the compressor face. Moreover, in order to increase the volume of fuel tanks and to reduce the system mass, the inlet is constrained to be short and compact, resulting in high exit to entrance area ratio.

These two sets of constraints are clearly conflicting: curved and short inlets that decrease the system observability and respect compactness constraints cause loss of efficiency. On the other hand, the improvement in the flow properties given by a longer, less curved inlet increases the propulsive efficiency of the system and leads to higher vehicle thrust and better manoeuvrability. Inlet length and compactness on one hand and airflow quality on the other hand have to be traded when designing these types of inlets. S-duct air inlets, which represent a decent compromise, are very commonly used on cruise missiles [9]. Figure 1-1 shows the Exocet block 3 missile, which features 4 serpentine air inlets sticking out of the missile body, its turbojet engine being buried in the center of the afterbody.

The flow in S-duct air inlets has been widely studied. It was shown that they are subject to boundary layer separation and secondary flows, because of their particular shape. This leads to a total pressure loss, distortion and instabilities at the compressor face, which can translate into surge and stall of the engine. The performance of the inlet can worsen when the inlet is subject to off-design external conditions, such as those that can occur when the aircraft is manoeuvring. In the case of high angle of attack and high-g maneuvers, forebody interactions can produce large separations leading to important pressure losses as well as high compressor face distortion, with much increased risk of compressor instabilities.

Despite a strong implication in the inlet design process, this problem has traditionally resulted in more stringent surge and stall margins, thus reducing the flight envelope. There is therefore definitely a need for a technology breakthrough that would extend the stable flow range of the compressor. Flow control techniques have received a great deal of interest in the last decade for the great promises they yield. For a correct implementation of those control techniques, a deep understanding of the flow structures is required.

The objectives of this project were to develop a test bed for flow control in an S-duct inlet at flow conditions representative of flight conditions, and to evaluate the performance of two flow control techniques: Vortex Generators and pulsed injection at the separation line. More precisely, the goal was to:

- understand the main characteristics of the separation phenomena in such an inlet,
- analyze the efficiency of mechanical VG and fluid injection on the separated area,
- evaluate the overall aerodynamic performance improvement of the inlet in terms of pressure recovery and distortion at the AIP in order to prepare future experiments with mini-actuators in terms of specifications and implementation.

Highly industry-driven, this project followed a comprehensive and realistic experimental approach.

1.2 Prior work

The flow in S-duct air inlets is subject to two main phenomena which cause the loss of performance and distortion at the compressor face: boundary layer separation and secondary flows. Several studies have focused on understanding the generation of those phenomena, both from a theoretical and experimental point of view.

J. Délery's synthesis [1] on three-dimensional separation is mainly based on Henry Poincarré's singular points in differential equations systems theory. He used this highly abstract grounds to interpret experimentally obtained flow visualizations obtained in wind or water tunnel experiments, and developed a rational tool that one can use to describe and interpret a flow field structure: Several objects that both have a mathematical definition and are experimentally observable are introduced, such as separation lines, separation surfaces, nodes, etc... These elements come with a set of simple rules that describe their organization, or topology, within a three-dimensional separated structure. The theoretical work of Perry and Chong [2] on separation structure description should also be pointed out. The presence of separation structures and secondary flows in S-duct inlets were shown in studies such as Reichert's and Vakili's, who approached the problem both experimentally [4, 6] and numerically [5, 7], Bradshaw's [8] and Brear's [10].

The effect on the engine of compressor face distortion is very well presented in Greitzer [3], which is constructed as a tutorial survey. The two main compressor instabilities, surge and stall are introduced, along with the notion of surge and stall margins in engine design. An extensive study of the effect of S-duct design parameters such as the diffuser half angle or its area ratio, on surge and stall margins has been carried out by Northrop Grumman and is presented in a paper by Tindell [9]. It sums up analytical, experimental and computational initiatives.

With the goal of reducing the detrimental effects of boundary layer separation and secondary flows, several flow control techniques have been developed. They are divided in two main categories: passive and active. Passive techniques are characterized by no energy input into the fluid, contrary to active which are characterized by a net energy input into the flowing fluid, by means of moving parts or fluidic injection.

The main passive control technique is the Vortex Generator (VG) technique. VGs are small surfaces of various shapes (rectangular, triangular, arches,...), used to generate streamwise vortices of the size of the boundary layer to enhance mixing of the high energy fluid from the core stream with the boundary layer decreased energy fluid. This technique was largely studied [11, 12, 13, 14], and was shown to be quite efficient at delaying or even suppressing separation mainly on airfoils, but also in air inlets. Their main drawback is the parasitic drag they induce The main active control techniques are steady or unsteady blowing or suction. Vortex Generator Jets, for example, were developed to minimize the VGs parasitic drag. They are very similar to VGs, but streamwise vortices are generated by a pulsating jet perpendicular to the wall. Suction and blowing can also simply be applied through a slot, usually parallel to the wall in order to benefit from the Coanda effect [15]. The synthetic jet, which simulates a pulsed jet thanks to a zero net mass flux apparatus has also received a great deal of interest [16, 17, 20, 21]. NASA [24, 25], for example, invested lots of efforts in this technique for which miniaturization and high frequency obtention are the main challenges. Many other active control devices such as micro-balloons actuators [23], magnetic micro-flaps [27] or sparkjet actuators [26] have been more marginally developed.

Control techniques have been experimentally implemented on S-duct inlets in many studies: Lockheed Martin and NASA have implemented micro-vane type VG and VGJ control on a very aggressively designed inlet (very high curvature, high compactness), at a flight Mach number of 0.6 [28]. In this study, a 36-micro vane type VG array was shown to have beneficial effect on pressure recovery, with somewhat mitigated results with the VGJ. Anderson has extensively studied passive VGs and proved their efficiency at reducing inlet distortion. His work included an exhaustive experimental parametric study at flight Mach numbers, a CFD analysis, and a theoretical part [29, 30, 31]. His work was conducted on a flyable geometry, as opposed to more aggressive geometries that have been used. At MIT, closed loop acoustic actuation was considered to control the flow in a UCAV very aggressive inlet [32], and a parametric study using pulsating injection about the separation line was carried out on the same inlet, always at flight Mach numbers (M=0.6) [34]. The effect of detrimental external conditions on inlet performances and distortion have been investigated, in particular in the Boeing Blended Wing Body (BWB) initiative, where the case of forebody Boundary Layer Ingestion (BLI) has been experimentally studied. The study included characterization of the BLI inlet with and without VG type control techniques, at very low Mach numbers (M=0.05) [35, 36, 40].

1.3 Research objectives

Flow control seems a promising way to extend the stable flow range of aircraft engines and thus extend the flight envelope. Industrial interest is thus rising for such flow control techniques. The purpose of this project is to experimentally evaluate and compare two of the most promising of these techniques on a realistic case, at conditions representative of flight conditions. The results of this project would provide solid grounding for future research with the further goal of actual implementation.

Contrary to many other studies, and motivated by the desire for a comprehensive realistic approach, a flyable missile inlet was chosen for this study, as opposed to futuristic aggressive geometries that are often found in the literature. This study focuses on the case of off-design external conditions, and more particularly the case of forebody Boundary Layer Ingestion (BLI) which can occur during certain maneuvers was selected.

The objectives of this project are thus to develop an experimental testbed for flow control in an S-duct inlet at flow conditions representative of flight conditions where BLI occurs, characterize the configuration with and without BLI to ensure understanding of the existing flow structures, and evaluate the performance of two selected flow control techniques at reducing distortion and improving inlet performance: VGs and pulsed injection were chosen based on previous bibliographical work, MIT experience and also for their relative simplicity and efficiency. An inlet geometry representative of S-duct inlets currently in use has been designed, and a model was fabricated and instrumented for flow control experiments. The inlet model was first characterized in the baseline configuration. A distortion generator was then used to simulate thick boundary layer ingestion. To manage the resulting distortion and loss of performance, VGs were first implemented, then pulsed injection. A comparative study was carried out.

This research is an attempt to answer several questions concerning the control of engine face distortion, including:

- Is engine face distortion primarily due to separation or secondary flows? These two phenomenon usually happen at the same time in S-duct inlets, both of them having a detrimental effect on the flow properties at the engine face. Therefore, it was attempted to design control effectors that would address each phenomenon separately and therefore help determine their individual influence on the flow properties at the engine face.
- Is the management of this distortion a question of redistributing the low-momentum fluid that accumulates at the inlet wall before separation, or a question of re-energizing this low-momentum fluid? Or, stated differently, is a passive technique sufficient, or is an energy input necessary?
- What is the efficiency of VG and injection at managing engine face distortion, and what are their relative benefits in terms of performance improvement?

1.4 Thesis outline

Since this research is experimentally based, Chapter 2 provides a detailed description of the experimental setup designed, fabricated and used to test flow control in the MBDA scale missile inlet. Details of the designed test section (inlet, bellmouth and constant area duct) are provided. The instrumentation and its calibration is also presented. Chapter 3 addresses the characterization of the inlet in both the bare configuration and with the BLI simulation setup. The design guidelines for the BLI setup are given, and the baseline results are discussed and interpreted. Chapter 4 presents the controlled configuration, both for the VGs and for the pulsed injection setups. Details of the control setups design and fabrication are provided. The controlled cases results are discussed and compared. Chapter 5 provides a summary of the experimental results and conclusions.

Chapter 2

Experimental Setup

This chapter presents the experimental setup on which the flow control experiments were conducted. Its purpose is to generate a flow at realistic cruise missile operating conditions (Mach number, Reynolds number and inlet mass flow) in an inlet model, and to enable flow control techniques implementation. The hardware at use is first described, followed by the the instrumentation and its calibration. The data reduction parameters in use in the remainder of the study are also presented.

2.1 Hardware

In this section, the main hardware components and their characteristics are presented. The facility and test section components (bellmouth and inlet model) are described. The design operating range is also presented.

2.1.1 Facility

All the experiments were conducted at the MIT Gas Turbine Laboratory (GTL). The facility configuration is shown in Figure 2-1, where two setups are visible: the calibration setup was used to calibrate the bellmouth (see section 2.3.2). The final setup contains the test section that hosted the flow control experiments. Mass flow is delivered through the test section by way of an open-loop system driven by a 1MW De Laval air compressor that acts as a suction source. Air is drawn from atmospheric conditions, passes through the test section, and then a heat exchanger before entering the compressor. After passing through the compressor, air is expelled through an exhaust pipe located on the roof of the GTL. To provide sufficient mass

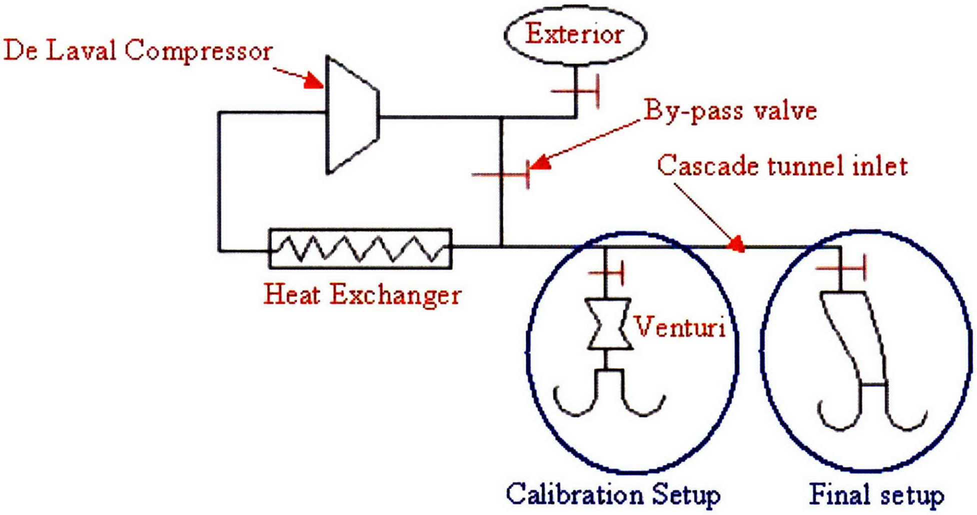
De Laval Compressor
Exterior
By-pass valve
Cascade tunnel inlet
Heat Exchanger
Venturi
Calibration Setup
Final setup

Figure 2-1: Facility configuration

flow through the compressor, it is necessary to recirculate part of the air that goes through the compressor. Therefore a by-pass duct was used, to re-introduce exit air back in the compressor. When the by-pass is used, the heat exchanger is required to maintain consistent inlet air temperature. The De Laval compressor run sheet is provided in Appendix C.

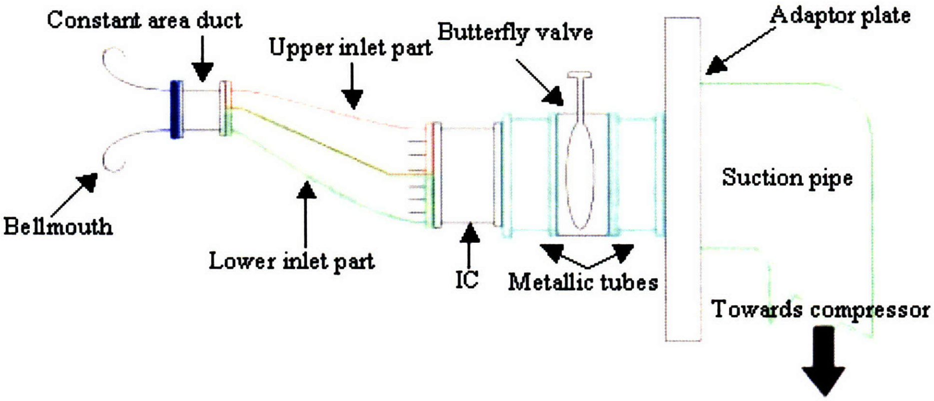
Constant area duct
Upper inlet part
Butterfly valve
Adaptor plate
Suction pipe
Bellmouth
Lower inlet part
IC
Metallic tubes
Towards compressor

Figure 2-2: Test section

The test section was designed and fabricated on the basis of the internal geometry provided by a preliminary work performed at MBDA. A schematic view is shown in Fig. 2-2. This test section lies on an aluminum plate and connects to the suction supply pipe via an adaptor plate, as shown on the sketch. Two cantilevered beams (not represented), bolted to the adaptor plate, support the test section. This support structure configuration isolates the experimental setup from the ground, thus minimizing the shear and stresses at the components interfaces. The cantilevered support also allows for easy access to all of the components within the test section [32]. The test section itself is a combination of parts fabricated by stereolithography (SLA), metallic parts fabricated at MIT and parts already existing at MIT. It consists of:

- a bellmouth contraction (SLA),
- a constant area duct (SLA),
- a scaled model of the MBDA subsonic inlet diffuser (SLA),
- the Instrument Can (IC, aluminum/stainless steel assembly),
- a butterfly valve (purchased industrial component),
- two metallic tubes placed upstream and downstream of the valve (steel welded elements).

The bellmouth smoothly accelerate the flow from atmospheric conditions, reduces distortion and avoids lip separation. It also provides mass flow measurements. The constant area duct further smoothes the flow. The experiments are conducted in the inlet model. The IC provides a total pressure map of the flow as it exits the inlet test section. The butterfly valve enables mass flow control, and the metallic tubes act as adapters. These components are described in the following sub-sections.

2.1.2 The transonic Inlet

Previous work at MBDA [33] has provided this project with a design of the internal surfaces of a full-scale inlet to be used for flow control experiments at MIT. The geometry is that of a tactical transonic inlet, designed for high-subsonic cruise conditions (Mach=0.6).

Figure 2-3 presents some geometrical details of the MBDA designed inlet. Its main characteristics are:

- a quasi-linear area distribution (subsonic diffuser) which makes the inlet entrance the throat of the test section,
- a trapezoidal entrance,
- a circular exit,
- an S-shape.

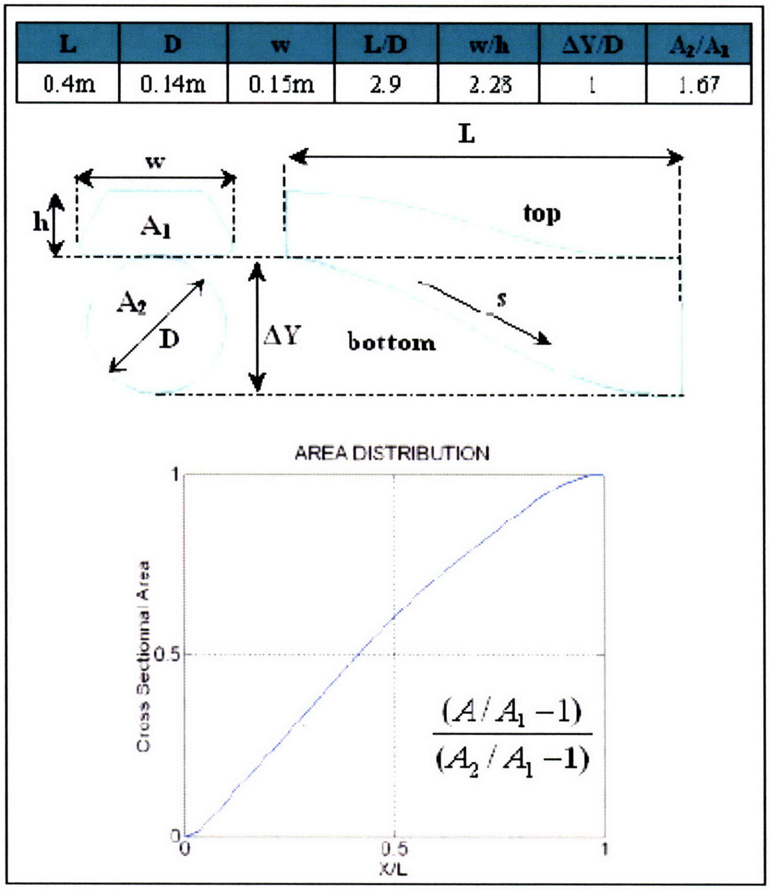

L	D	w	L/D	w/h	ΔY/D	A_2/A_1
0.4m	0.14m	0.15m	2.9	2.28	1	1.67

Figure 2-3: Inlet geometrical parameters

The top of the exit corresponds to the bottom of the entrance, which sets the offset ratio to 1. The reference throat Mach number M_{th} is taken at the throat of the test section, i.e. at the inlet entrance. This geometry, which is inspired from currently used geometries is not as aggressive as other cases that have been studied [10, 34, 28, 28]:

- the expansion ratio, which is the ratio of exit area to entrance area, is $A_2/A_1 = 1.67$,
- the length to diameter ratio, which gives a measure of the inlet compactness, is $L/D = 2.9$.

An aggressive design would set $A_2/A_1 \approx 4$ and $L/D = 1.5$ to 2.5. A more complete description of the inlet geometry is provided in Appendix A.

The scaled MBDA inlet model provides the same characteristics than the geometry described above. It represents a 60% scale, compared to the size of a typical transonic cruise missile inlet. This was chosen to achieve compatibility with existing equipment. The resulting overall dimensions for the scaled model internal surfaces are:

- length: $L = 15.7''/0.398m$,
- exit diameter: $D = 5.4''/0.137m$,
- inlet height: $h = 2.65''/0.0673m$,
- inlet width: $w = 6.05''/0.154m$.

As the inlet has a trapezoidal shape, its characteristic length scale was not obvious to chose. It was decided to use its hydraulic diameter d_H, computed using the formula given by Eq. 2.1:

$$d_H = \frac{4A_1}{C} \tag{2.1}$$

where A_1 is the entrance cross-sectional area and C its circumference. This leads to $d_H = 0.178m$, very close to its larger overall dimension.

The actual inlet parts were designed around this scaled geometry. For practical reasons, the geometry was installed upside down, so that the bellmouth is far enough away from the support beams when mounted on the suction pipe. The inlet thus bends downwards in the main flow direction.

During flow visualization experiments (e.g. oil flow visualization) and instrumentation, direct access to the internal surfaces of the inlet was required. The inlet therefore had to be split into two parts. The lower part is the part that lies on the aluminum plate. The injection setup had also to be placed on this part, hanging down. The upper part rests on top of the lower.

The interface between the lower and upper parts was made as flat as possible and so that the whole internal surface was directly accessible. O-ring assemblies and flanges were included. Figure 2-4 provides views of the designed inlet parts.

The inlet extends downstream to the flange of the 41 total pressure probe IC. Since the probes extent forward of the flange, there is no flange at the Aerodynamic Interface Plane (AIP). As there was no room for an O-ring groove either on the inlet or on the metallic IC, this was found to be the best solution to avoid any leakage at the AIP. The 41 total pressure probes extent into the inlet to reach the AIP.

The upper and lower parts are fixed together by 16 screws and metallic inserts. Two pins provide alignment. They are fixed to the constant area duct by 8 screws

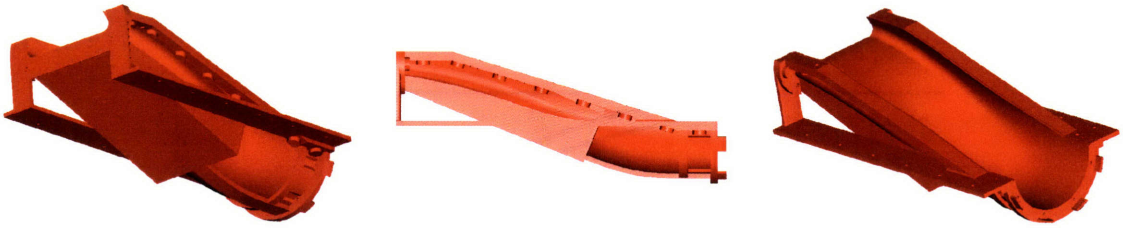

(a) Lower part bottom view (b) Lower part side view (c) Lower part top view

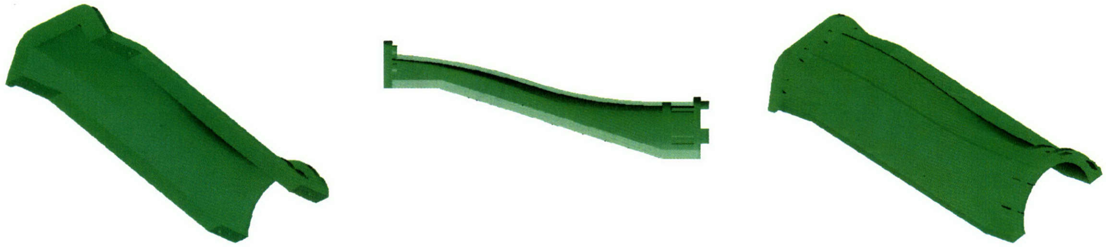

(d) Upper part bottom view (e) Upper part side view (f) Upper part top view

Figure 2-4: Inlet SLA parts

and metallic inserts, and to the IC by also 8 screws. Four pins and 8 tabs respectively provide alignment with the constant area duct and the IC.

The injector position was determined later in the project, so a block of material was first left at its approximate position on the lower part. It was machined at MIT later on when the injector position was decided.

2.1.3 The bellmouth

The bellmouth geometry was chosen to smoothly accelerate the flow coming into the inlet from rest to Mach numbers as high as M=0.95. To prevent distortion generation, there is no cross-section shape change, so the bellmouth is just a convergent trapezoidal duct.

The bellmouth geometry design applied the specifications of the American Society of Mechanical Engineers (ASME) for low-β bellmouth design [42, 43]. β is the ratio of the entrance diameter to the throat diameter. The contraction is elliptical, with the major semi-axis equal in length to the inlet characteristic dimension, and the minor semi-axis equal in length to the two third of the inlet characteristic dimension. To avoid cowl lip separation and vortices generation, the lip has been curled circularly

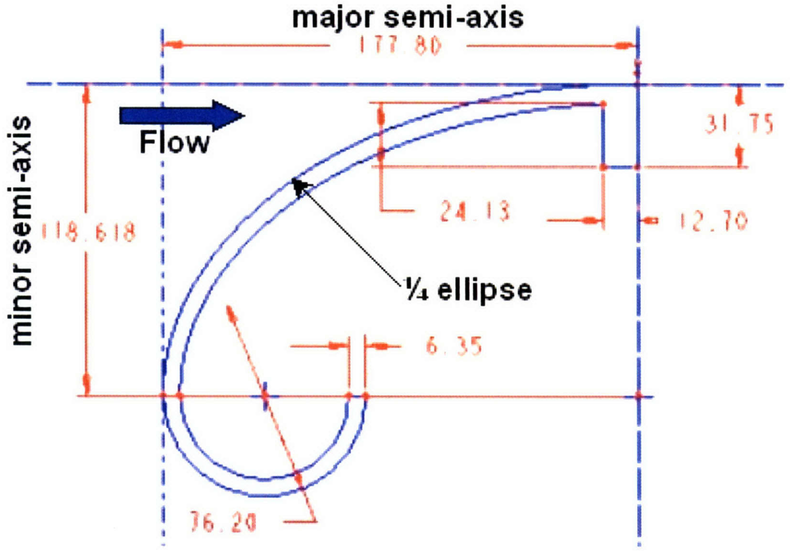
major semi-axis
177.80
Flow
minor semi-axis
118.618
31.75
24.13
12.70
¼ ellipse
6.35
76.20

Figure 2-5: Bellmouth elliptical contraction

with a diameter equal to 0.4 times the characteristic length of the inlet. Figure 2-5 shows a sketch of the elliptical contraction, with dimensions in mm. This geometry results in a quasi-linear Mach number evolution through the bellmouth, which satisfies the requirements to minimize peak flow accelerations.

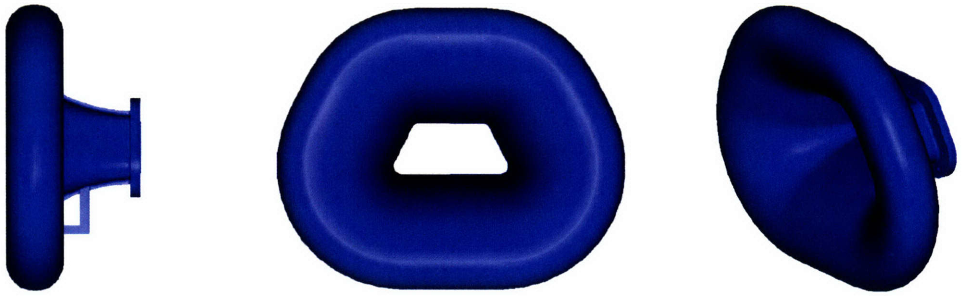

(a) Side view (b) Front view (c) Diagonal view

Figure 2-6: Bellmouth SLA part

The bellmouth part was designed based on this geometry and has the following geometrical characteristics:

- length $L_b = 0.178m$,
- length to exit diameter ratio $L_b/D_b = 1$,
- area ratio $A_{entrance}/A_{exit} = 11$.

The wall thickness was set at $6.25mm$. A $12.5mm$ thick vertical and $31.75mm$ high flat flange and 8 screws connect the bellmouth to the constant area duct. To support the plate so that it doesn't bend under its own weight, support legs have been added around the center of gravity. These legs lie on the aluminum plate. 2 pins provide alignment with the constant area duct.

A constant area duct was placed between the bellmouth and the inlet. It is shown on Fig. 2-7.

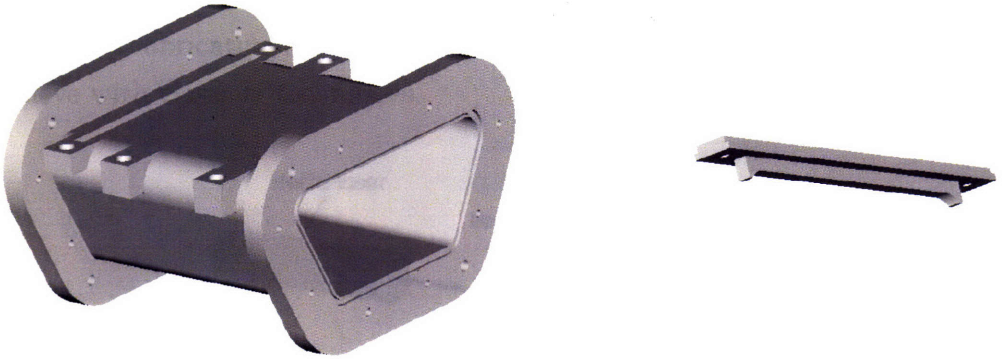

(a) Main part (b) Slot filler

Figure 2-7: Constant area duct SLA parts

Its function is to align the flow parallel to the inlet axis, and to provide the space necessary to place the distortion device to generate the boundary layer thickness representative of that in the presence of the forebody. It also allows placement of the inlet entrance boundary layer thickness measurement device. Its characteristics are:

- The length recommended for such a duct without an obstacle is equal to its diameter. The length has thus been set to the inlet entrance characteristic length $0.178m$. The walls are $6.25mm$ thick.
- Two flanges with o-ring compression assemblies and pin holes (for alignment) were designed at each extremity to avoid air leak. These flanges are identical so that the duct can be used in one sense or the other.
- To provide probe access to the inside of the duct, a slot was designed. It is $6.25mm$ wide and extends through the whole straight portion of the larger

base. It provides access to the boundary layer total pressure probe used for boundary layer measurements (see Section 2.2).

- An additional part was created to fill the slot when the boundary layer total pressure probe is not used. It is fixed to the constant area duct by two screws and two metallic inserts.

2.1.4 Parts fabrication

Although SLA parts cannot achieve the same geometric and pressure and temperature ranges as metal models, they are much less costly and can be built much faster. SLA also allows fabricating shapes that would have been very difficult if not impossible to achieve with classical techniques.

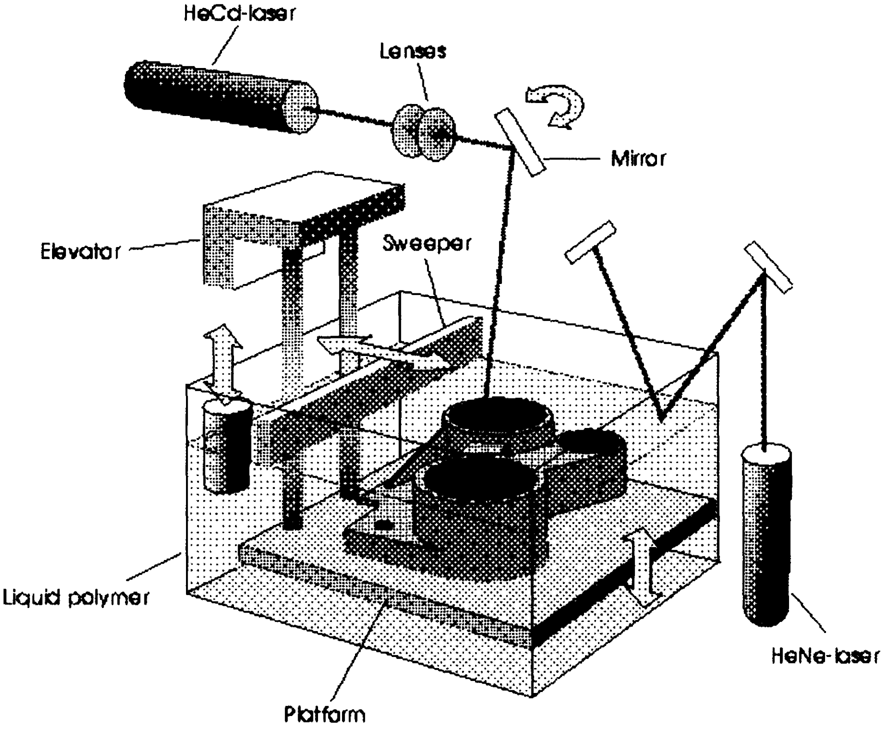

Figure 2-8: SLA apparatus

The stereolithography fabrication technique operates as follows [44]: a photopolymer is used as the building material. A photopolymer is a liquid resin that polymerizes (solidifies) when exposed to an ultra-violet laser beam. In the SLA process which apparatus is shown in Fig. 2-8, a part is built layer by layer, each layer being drawn by a laser that scans the surface of a tank of liquid resin (also called a vat). An elevator then lowers the part under the surface of the liquid to a distance equal to the thickness of the next layer and the process is repeated again. A sweeper breaks the surface tension and ensures that a flat liquid surface is obtained. Fortunately, the layers bind to each other. At the end, the part is removed from the vat, and the remaining liquid resin is washed off.

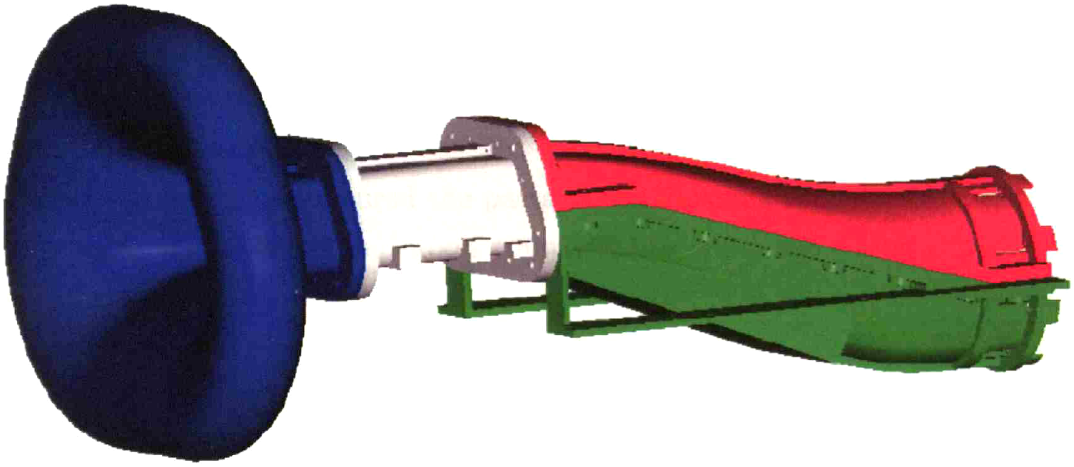

Figure 2-9: Assembled SLA parts

Several companies provide SLA manufacturing services. A pool of 4 potential contractors was quickly chosen, based on capabilities in terms of geometrical accuracy, quality of customer service and pricing. These companies were:

- Quickparts.com (www.quickparts.com),
- 3D-CAM (www.3d-cam.com),
- Solid Concepts (www.solidconcepts.com),
- CRDM (www.crdm.org.uk).

A first design was used to obtain quotes and technical advisory from these companies, which restricted the choice to 2 companies, Quickparts and 3D-CAM. The final choice was based on pricing only.

The resin that was finally used is the SOMOS 14110 resin, recommended for wind tunnel test-model fabrication. The choice of the resin was made on the basis of tests carried out at the GTL machine-shop on samples provided by the companies. Overall, the SLA material proved to be quite resistant to stresses, but brittle when subject to

Table 2.1: Test conditions: throat Mach number, CMF and throat Reynolds number

M_{th}	CMF in $kg.s^{-1}$	Re_{d_H}
0.4	1.22	$.86\,10^6$
0.5	1.50	$1.10\,10^6$
0.6	1.67	$1.27\,10^6$
0.7	1.82	$1.46\,10^6$
0.8	1.95	$1.68\,10^6$
0.88	2.01	$1.80\,10^6$

shocks. Drilling, machining and insertion of numerous metallic threaded inserts was possible, but the parts had to be handled with extreme caution in the process.

Quickparts.com manufactured the parts, did a finishing step on the internal surfaces to ensure smoothness and good compatibility when the parts are assembled, and placed the metallic inserts. A CAD view of the SLA parts when assembled is provided in Fig. 2-9.

2.1.5 Operating range

One of the test objectives was to evaluate the performance of various flow control techniques at high subsonic Mach numbers. The design point of the full scale inlet is $M_{th} = 0.6$. A wide range of flight representative Mach number $[0.4 - 0.88]$ was achieved, to cover more flight conditions. This corresponds to Corrected Mass Flow (CMF) rate in the test section in the range $[1.2 - 2]kg.s^{-1}$ (see Table 2.1.5). In this thesis, CMF and throat Mach number are both used to refer to a particular flow condition. Table 2.1.5 provides the equivalences. The Reynolds number Re_{d_H} is based on the hydraulic diameter of the throat d_h.

2.2 Instrumentation

The measurements consisted of steady-state pressure and temperature measurements. They were used to acquire or compute the following information:

- the inlet mass flow,
- the compressor operating conditions (mass flow, pressure ratio, temperature...),
- a map of the total pressure field entering the inlet,
- a map of the total pressure field at the AIP,

- the static pressure along the centerline of the inlet,
- the boundary layer thickness at the inlet entrance section.

The setup was therefore permanently instrumented with wall static pressure taps and a 41 total pressure probe IC. A traverser setup was designed and fabricated, and was used occasionally for inlet plane total pressure mapping and boundary layer measurement. The data acquisition hardware was monitored on a dedicated computer through codes that were written specifically. This section gives an overview of the instruments at use, along with their data acquisition system and monitoring codes.

2.2.1 Instruments

48 wall static pressure taps were placed on the test section. They are made of metallic micro-tubes (Outer diameter: $1mm$, Inner Diameter: $0.68mm$) that are pushed through the part material up to the internal surface of the duct, so that the inside of the tube is open to the flow. They are connected to the data acquisition system by Tygon tubing. They were placed at various positions: (i) 7 along the bellmouth centerline, exactly one every axial inch ($1'' = 2.54cm$), mainly to provide the data required to compute the mass flow in the test section, (ii) 16 along the inlet centerline, exactly one every curvilinear inch, to provide the static pressure evolution in the duct and (iii) 8 at the AIP and at the bellmouth circumferences, equally spaced, to check for circumferential distortion.

Two static pressure ports were also allocated to a downstream and an upstream station on the De Laval compressor. The pressure read by these ports was used to determine the De Laval operating conditions.

A flat total pressure probe was designed and fabricated. It was used with the traverser (see section 2.2.2) to scan the inlet entrance section and characterize the flow ingested by the inlet.

The Instrumentation Can contains a rake of 41 steady total pressure probes, manufactured by Northrop Grupman and on loan to MIT. It complies with the SAE ARP-1420 recommendations [42]. On this type of rake, each probe is located at the centroid of an equal area section, which allows easy computations of various parameters such as distortion descriptors and the pressure recovery (see section 2.4). The IC data also provided color contour maps of the total pressure at the AIP under various

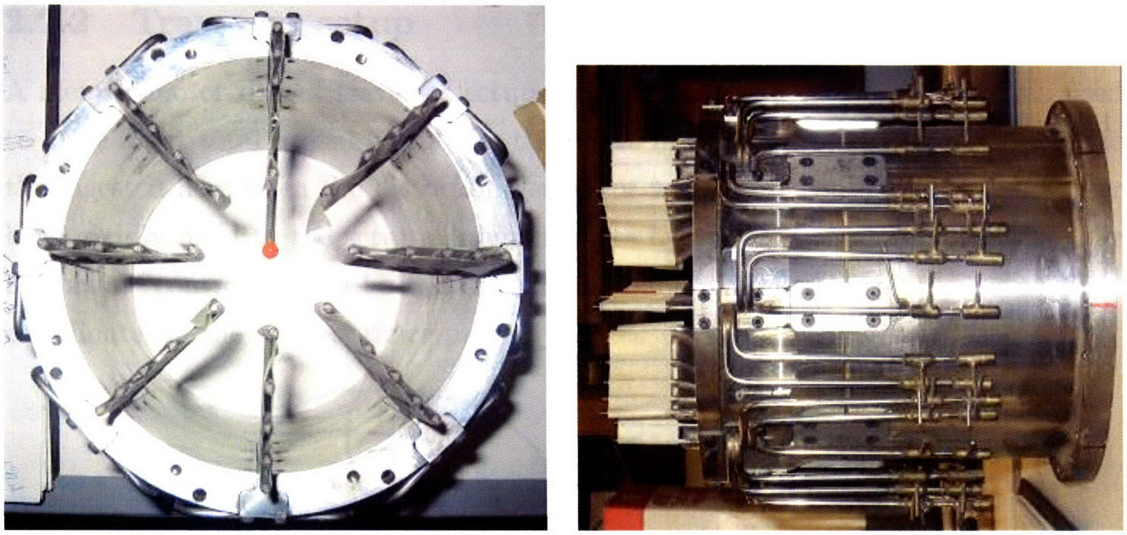

(a) Streamwise view, showing 8 total pressure probes

(b) Side view, probes are protected by tape

Figure 2-10: The Instrumentation Can

flow conditions and with or without flow control. The IC is mounted directly downstream of the SLA inlet parts, and upstream of the butterfly valve via an adaptor (one of the two metallic tubes). The 41 total pressure probes, shown on Fig. 2-10, are distributed in 8 rakes (located 45^o apart) and 5 instrumentation rings (5 probes on each rake plus one at the AIP center). They slide in the SLA inlet parts to reach the AIP.

A mercury thermometer was used to measure the ambient temperature before each run, to permit Mach number computation.

Ambient pressure was obtained using the GTL mercury barometer, cross-checked with the information provided by the Logan Airport meteorological center.

An oil flow visualization technique similar to that described in Reichert [4], using a dark dye and silicon oil mixture, helped reveal the flow field characteristics. The inside walls of the inlet were painted with the black mixture. The running flow then entrains the liquid along specific shear stress lines, which can be shown to be the identical to the streamlines the closest to the wall [1].

2.2.2 Traverser setup

A stepper-motor driven traverser setup was designed and fabricated. It was used to drive a flat total pressure probe in the entire inlet entrance plane to characterize the ingested flow when the distortion generator was on. It consists of two traverser bars, rigidly fixed to the setup aluminum plate by way of two aluminum legs. The motors are controlled by a Labview program, enabling automatic placement at given coordinates in the inlet entrance plane.

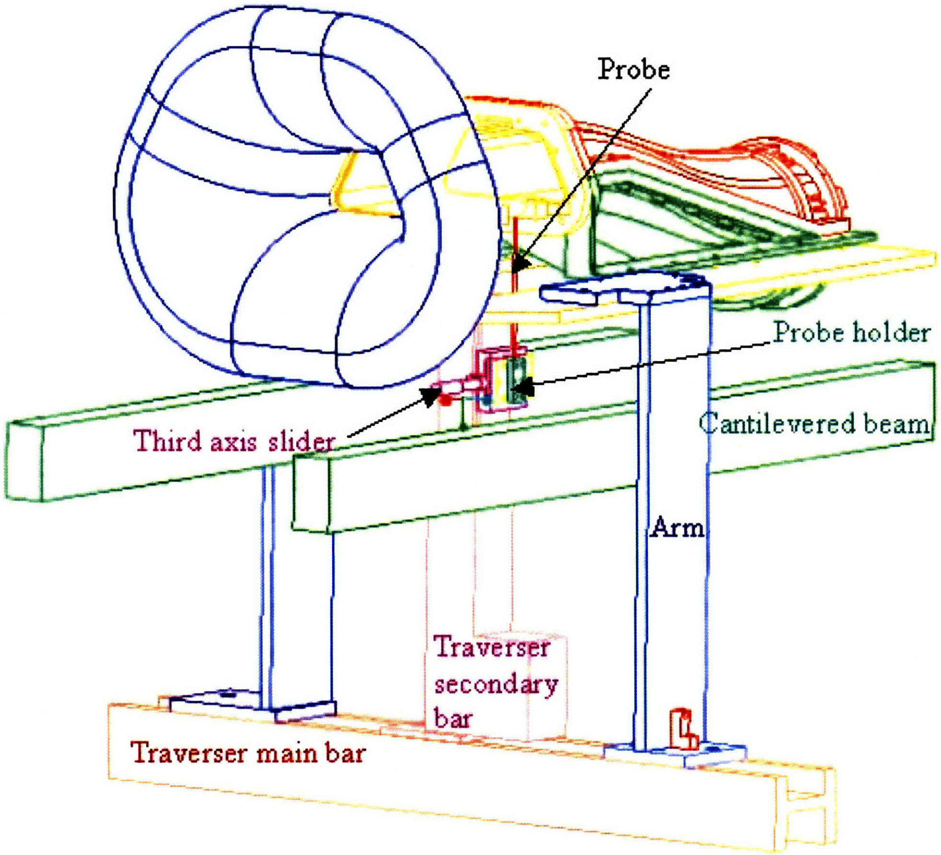
Probe
Probe holder
Cantilevered beam
Third axis slider
Arm
Traverser secondary bar
Traverser main bar

Figure 2-11: The traverser setup

Figure 2-11 shows a simplified CAD view of the traverser setup.

2.2.3 Data acquisition

The pressure probes and wall ports are connected via Tygon tubing to 4 Scanivalve electronic boxes containing the pressure transducers. Three of these units are Scanivalve model "DSA 3217/16Px" 200Hz maximum sampling frequency units, each containing 16 independent transducers, the fourth unit is a Scanivalve "SCANCO SSS 48 CMK3" unit controlled by a Scanivalve "SDIU MK5" unit. The latter is a slower unit, made up of a stepper motor-driven rotative head that can be aligned with each of the 48 pressure ports.

The Scanivalve Digital Interface Unit (SDIU) is responsible for controlling the 48 port Scanivalve transducer and displaying the output. It connects to the controlling computer via Serial Port and processes commands from the control program, including homing the rotative head and triggering data acquisition. The SDIU performs the steady pressure data acquisition and converts the transducer analog response to a digital reading of absolute pressure. The DSA units provides directly a 16 channel digital TCP/IP output.

On the software side, a Labview interface program, running on the experiment's dedicated PC, controls remotely the SDIU and the 3 DSA units simultaneously, and provides real time information about the compressor operating conditions, inlet mass flow and traverser status when in use. Various Matlab functions are imbedded in the Labview program to execute the required aerodynamic computations.

2.3 System calibration

The bellmouth was calibrated against an industrial Venturi tube to provide 1% accuracy mass flow measurements. This required the fabrication of a preliminary setup. Moreover, the Scani-valve units required a quick 2 point calibration before each run. This section describes the bellmouth calibration procedure and briefly overviews the Scani-valve calibration.

2.3.1 Scani-valve calibration

The Scani-valve units were fully calibrated prior to this project. Before each run, an additional quick two-point calibration was performed:

- in a first time, all ports were let open to the air so that the differential pressure transducer would all see a null pressure. Measurements were recorded to correct for the potential static drift.
- in a second time, the ground port was connect to a vacuum pump, so that all the ports would see a differential pressure of one atmosphere. This second point would allow to correct for slope drift.

This procedure tuned all the various units in use to the same references.

The atmospheric pressure and temperature were measured before the runs, using the GTL precision mercury barometer, the Logan Airport Information center data, and a 0.1^oC-precision mercury thermometer.

Mass flow rate measurement with the Venturi tube required the use of a thermistor. It was two point-calibrated calibrated against the mercury thermometer, using ambient temperature conditions and a water/ice bath. They were found to agree within $0.2K$. This ensured 0.5% accuracy for the pressure readings. The mass flow rate measurement was thus only limited by the Venturi built-in accuracy of 1%.

2.3.2 Bellmouth calibration setup

The bellmouth and constant area duct were instrumented with wall static pressure taps. The goal was to obtain an estimate of the static pressure in the duct/bellmouth section and correlate it to the mass flow rate measured in the Venturi, to give the bellmouth calibration curve. The average of the pressures at the bellmouth exit flange was chosen as the primary pressure reading against which to correlate the mass flow. When the distortion generator was on, the pressure read on the bellmouth centerline is used instead. The pressure were read using one of the fast, highly accurate DSA units.

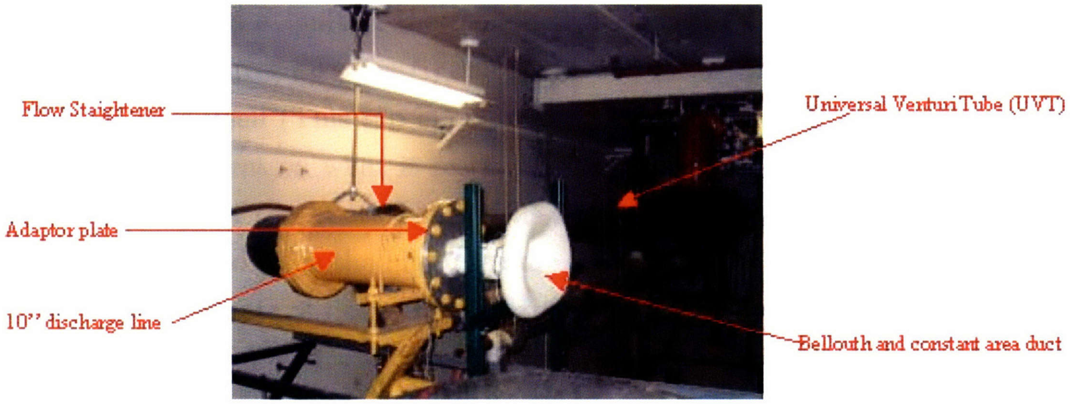

Figure 2-12: The bellmouth calibration setup

The bellmouth calibration setup was located in one of the Gas Turbine Laboratory (GTL) test cells, on the $0.254cm$ diameter discharge line. The bellmouth and the constant area duct were mounted in line with the Universal Venturi Tube (UVT). The pipes on which the Venturi is mounted are connected to the De Laval compressor via a network of pipes and valves (see Fig. 2-1). Changing the bypass ratio of the De Laval compressor, or opening or closing the gate valve on the discharge line could control the mass flow rate through the setup.

2.3.3 The Venturi

The Venturi tube in use was a BIF, Inc. [47] "Universal venturi tube" (U.V.T.) part number 0182-10-2291 with a throat diameter of $0.127m$. The venturi is mounted in the $0.254m$ diffuser-tester discharge line, in one of the GTL test cells.

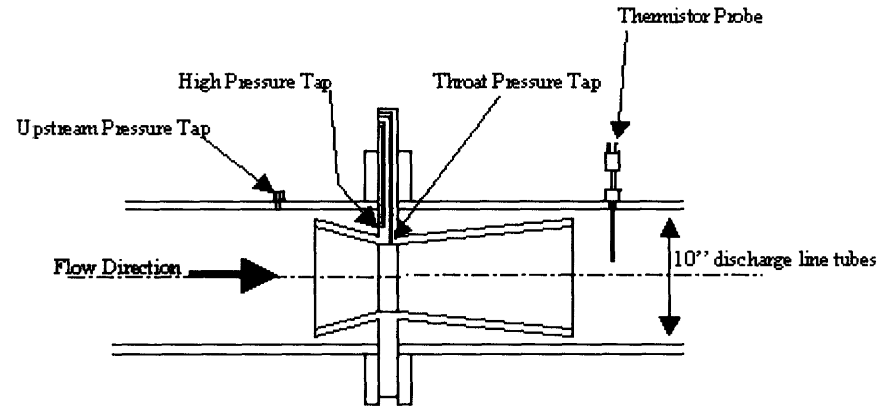

Figure 2-13: The Venturi tube

The Venturi has a built-in thermistor probe located downstream of the throat and three built-in pressure taps: (i) one at the $13.716cm$ throat, (ii) one upstream on the $0.254m$ pipe itself (This tap is positioned upstream enough so that the Venturi presence has no effect on what it reads [45]), and (iii) one located on the upstream face of the flange of the Venturi tube (the flange that is clamped between the pipe flanges) and referred to as the high pressure tap.

The mass flow rate is deduced from the pressure readings at the upstream and throat pressure taps, and the temperature reading on the thermistor probe. The high-pressure tap reading can also be used but the turbulence level was higher at its location, making the readings less stable. Its readings were recorded to check for consistency, but not used in the calibration procedure.

The whole mass flow rate measurement procedure (as given by the documentation provided by BIF), is based on the discharge coefficient C_D of the UVT, defined as the ratio of the actual mass flow rate to the theoretical mass flow rate. It is considered [46] to be constant with a value of 0.980 to within 0.5% for Reynolds numbers based on the pipe diameter of 75,000 and above. This covers the range of the future experiments down to the lowest mass flow rate ($1.22 kg.s^{-1}$ corresponding to a Mach number of $M_{th} = 0.4$ at the throat) envisioned, as the Reynolds number based on the pipe diameter is then approximately $2\,10^6$. The Venturi remains unchocked for mass flow rates as high as $70 kg.s^{-1}$, which is far above the highest mass flow rate envisioned for our experiments. The rated uncalibrated accuracy of the U.V.T. is to within ±1%.

The theoretical mass flow rate is first computed on the assumptions of uniform compressible flow properties at the upstream and throat static-pressure tap locations, and conservation and uniformity of total pressure and total temperature between the locations of the total pressure and total temperature probes. Given the upstream (station 1) static pressure, and the throat static pressure (station 2), and the total temperature of the flow, the theoretical mass flow rate is calculated as follows.

By continuity the mass flow rates through stations 1 and 2 are the same:

$$\dot{m}_{1th} = \rho_1 U_1 A_1 = \dot{m}_{2th} = \rho_2 U_2 A_2 \tag{2.2}$$

Equation 2.2, combined with the equation of state of a perfect gas:

$$P = \rho r T \tag{2.3}$$

the definition of the Mach number:

$$M = \frac{U}{a} = \frac{U}{\sqrt{\gamma r T}} \tag{2.4}$$

and the relationship between static and total temperature in a flow of a perfect gas:

$$\frac{T_t}{T} = 1 + \frac{\gamma - 1}{2} M^2 \tag{2.5}$$

can be written as:

$$\dot{m}_{th} = \frac{P_2}{r T_t} \sqrt{\gamma r T_t} M_2 \left(1 + \frac{\gamma - 1}{2} M_2^2\right)^{1/2} A_2 \tag{2.6}$$

Applying the basic relations for the adiabatic-isentropic flow of an ideal gas, an expression for M_2^2 in terms of the upstream-to-throat static pressure and area ratios is obtained:

$$M_2^2 = \frac{\frac{2}{\gamma-1}\left(\left(\frac{P_2}{P_1}\right)^{\gamma-1/\gamma} - 1\right)}{1 - \left(\frac{A_2}{A_1}\right)^2 \left(\frac{P_2}{P_1}\right)^{-2/\gamma}} \tag{2.7}$$

As P1 and P2 are measured, and the area ratio is known, this equation can be used to eliminate M_2 from Eq. 2.6 and thus calculate it, given the total temperature. The actual mass flow rate is then determined by applying the discharge coefficient:

$$\dot{m}_{actual} = C_D \dot{m}_{th} \tag{2.8}$$

2.3.4 Bellmouth calibration curve

The main result of the bellmouth calibration is the calibration curve. It represents the ratio of static pressure to total pressure at the bellmouth flange versus the Corrected Mass Flow (CMF) through the setup, deduced from the pressure readings on the Venturi. The calibration goal is to provide data to correlate those parameters.

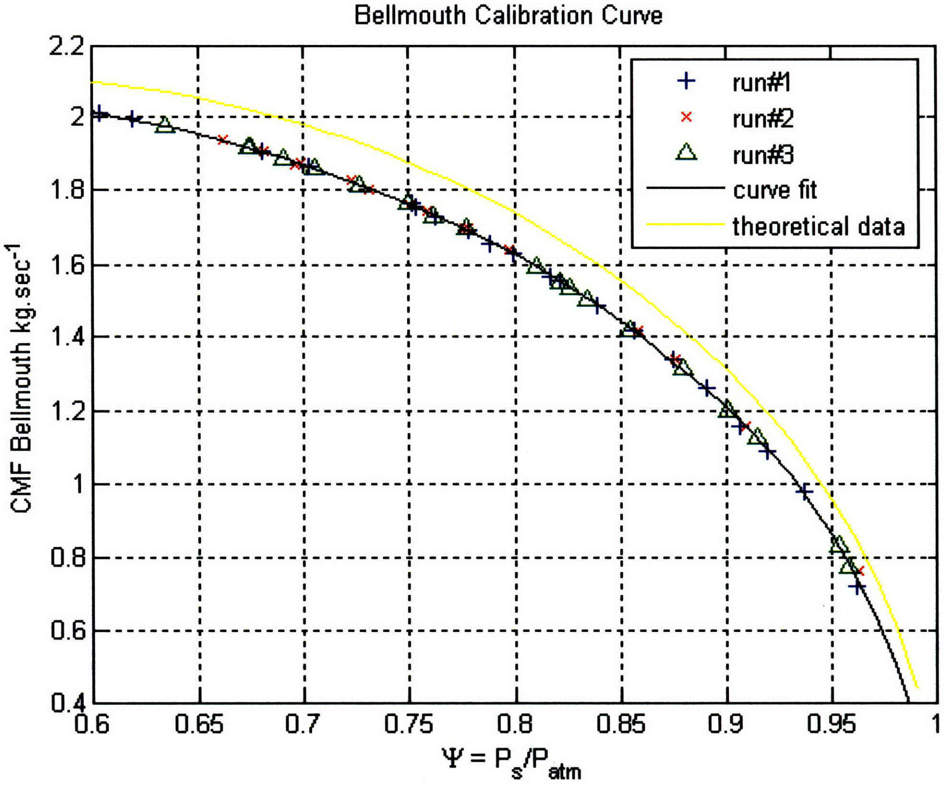

Figure 2-14: The bellmouth calibration curve

As can be seen on Fig. 2-14, the results from the various runs agree very well, despite difference in atmospheric conditions from one test to the other. This ensures the repeatability of the mass flow measure. A curve similar to that displayed in Fig. 2-14 was obtained for each of the bellmouth pressure ports, thus enabling mass flow computation on the basis of the pressure read on any of these ports.

In theory, the CMF through the bellmouth could be directly deduced from the ratio of static to total pressure (referred to as non-dimensional pressure), using the assumption of uniform compressible perfect gas flow properties, with conservation of total temperature and total pressure along the bellmouth. Given the static pressure p at the bellmouth port, the mass flow $\dot{m}$ measured at the Venturi and the ambient temperature and pressure conditions T_t and P_t, it can be theoretically calculated as follows: First, using Eqs. 2.3, 2.8, and 2.5, the usual ratio between p and P_t can be deduced:

$$\frac{P_t}{p} = \left(\frac{T_t}{T}\right)^{\gamma-1/\gamma} \tag{2.9}$$

which gives an expression of the Mach number at the pressure port location in terms of the pressure ratio:

$$M = \sqrt{\left(\left(\frac{P_t}{p}\right)^{\gamma-1/\gamma} - 1\right)\frac{2}{\gamma-1}} \tag{2.10}$$

The Mass Flow Parameter is a Mach number only dependent parameter that can be derived from Eq. 2.6 as:

$$MFP(M) = \frac{\dot{m}\sqrt{rT_t}}{P_t A} = \frac{M\sqrt{\gamma}}{\left(1+\frac{\gamma-1}{2}M^2\right)^{\gamma/2(\gamma-1)}} \tag{2.11}$$

The CMF is then deduced by re-dimensionalizing the MFP expression using the ambient and the reference conditions:

$$CMF\left(\frac{p}{P_T}\right) = \frac{\dot{m}\sqrt{rT_t}}{P_t A}\frac{P_{ref}}{\sqrt{rT_{ref}}} = \dot{m}\sqrt{\frac{T_t}{T_{ref}}\frac{P_{ref}}{P_t}} \tag{2.12}$$

This provides a theoretical calibration curve to check for consistency. The difference between this theoretical result and experimental data is due to the inevitable losses the bellmouth produces. This also justifies why the non-dimensional pressure p/P_t can be used as a relevant parameter to compute the CMF.

It is also interesting to note that the pressure was found to *increase* along the

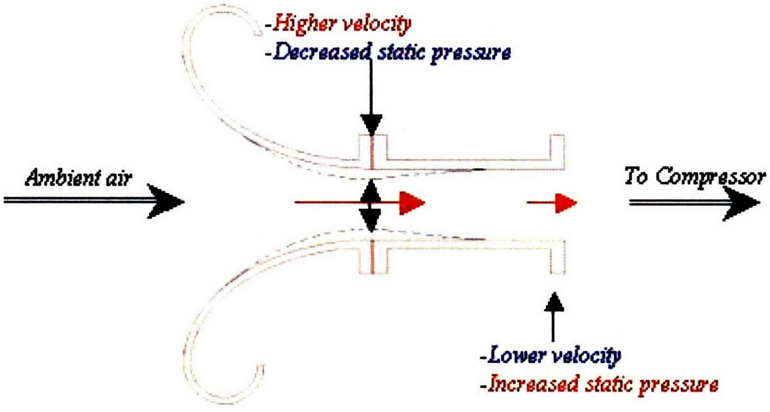

Figure 2-15: The bellmouth vena contracta

constant area duct, when it was expected to decrease: because of wall friction and to conservation of mass flow along the duct, the pressure should decrease. The proposed explanation for this phenomenon is the presence of a vena contracta at the bellmouth flange, which locally reduce the effective area, thus locally reducing the pressure. There is therefore a balance between this effect and the wall friction. In the lower range of mass flow, the vena contracta effect was found to be predominant, and in the upper range of the mass flow, the wall friction effect becomes predominant.

2.3.5 Mass flow deduction

The experimentally obtained calibration curve was interpolated by fitting a 7^{th}-order polynomial to the data. The equation of this fitting curve, shown in Fig. 2-14, is given by Eq. 2.13:

$$\begin{aligned} CMF = & -34816.17\left(\frac{p_b}{P_{T0}}\right)^7 + 189020.33\left(\frac{p_b}{P_{T0}}\right)^6 - \\ & -438074.28\left(\frac{p_b}{P_{T0}}\right)^5 + 561754.79\left(\frac{p_b}{P_{T0}}\right)^4 - \\ & -430420.78\left(\frac{p_b}{P_{T0}}\right)^3 + 197040.65\left(\frac{p_b}{P_{T0}}\right)^2 - \\ & -49899.01\left(\frac{p_b}{P_{T0}}\right) + 5394.62 \end{aligned} \tag{2.13}$$

where p_b is the pressure read on the bellmouth flange, and P_{T0} the freestream total pressure.

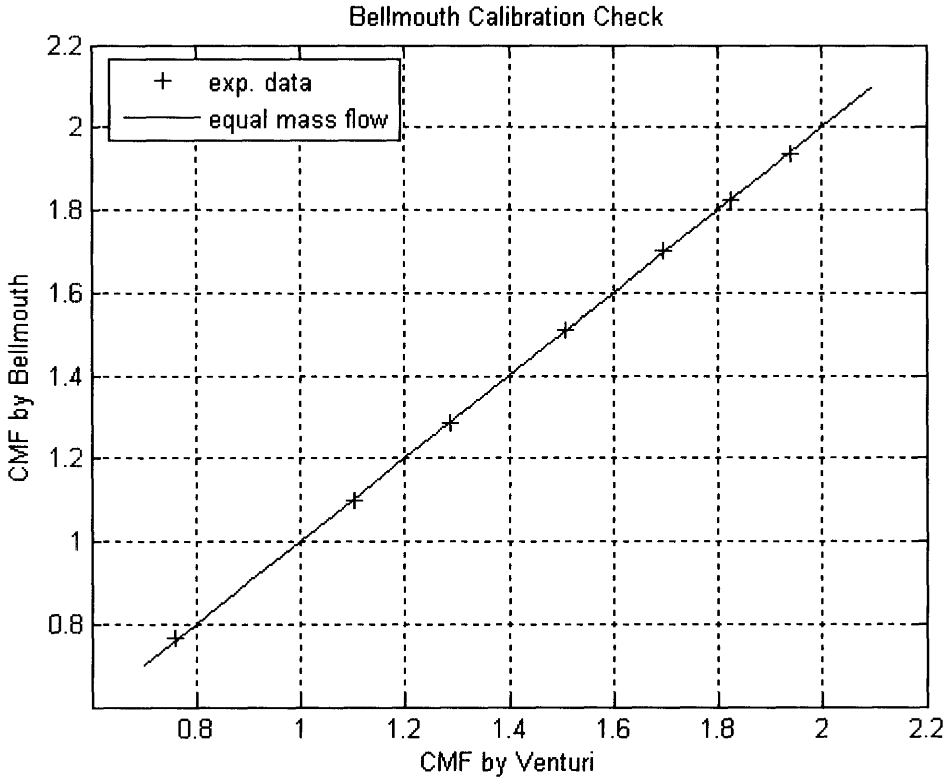

Figure 2-16: Bellmouth calibration check

A calibration check was performed: data that were not used for the building of the calibration curve were gathered and used to compute the CMF by means of the calibration curve, and compared to the CMF read on the Venturi. Figure 2-16 shows an excellent agreement between the two.

2.4 Data reduction

This section describes the parameters used to describe the inlet operating conditions and to quantify the inlet distortion and efficiency.

2.4.1 Inlet operating conditions

It was chosen to refer to the inlet operating conditions in terms of mass flow rate. As air was drawn from ambient atmosphere which temperature and pressure could vary, the mass flow obtained for a target inlet throat Mach number could vary from one test campaign to the other. The Corrected Mass Flow (CMF), which is the mass flow corresponding to the same inlet throat Mach number at US reference sea level atmospheric conditions ($P_{ref} = 101\,327 Pa$, $T_{ref} = 288.17K$), provides a common reference. It is defined by Eq. 2.14.

$$CMF = \dot{m}\frac{P_{ref}}{P_{T0}}\sqrt{\frac{T_{T0}}{T_{ref}}} \tag{2.14}$$

where $\dot{m}$ is the actual mass flow rate, P_{T0} and T_{T0} are the freestream (ambiant) total pressure and temperature.

Description of the static pressure profile, for example along the inlet centerline, made use of the static pressure coefficient C_p defined by Eq. 2.15.

$$C_p = \frac{p - p_{th}}{P_{T0} - p_{th}} \tag{2.15}$$

It is based on a reference static pressure, p_{th}, taken at the inlet throat.

When the screen was used, its total pressure recovery PR_s was computed with respect of Eq. 2.16.

$$PR_s = \frac{1}{P_{T0}}\left[\frac{1}{A_1}\iint_{A_1} P_T(x,y)dA\right] \tag{2.16}$$

where $P_T(x,y)$ is the total pressure measured in the elementary area dA centered on the point of coordinates (x,y). This information was provided thanks to the traverser setup.

2.4.2 Inlet performance descriptors

The primary inlet performance parameters in use are inlet pressure recovery, P_{Te}/P_{T0}, an average circumferential distortion descriptor, $DPCP_{avg}$, and a maximum radial distortion descriptor, $DPRP_{max}$. These parameters are defined in the SAE ARP1420 [42]. To derive these descriptors, all sensitivity parameters were set to 1.0 and all offset terms to 0.

Figure 2-17 shows a typical one-per-revolution pattern plot of total pressure along an IC ring (ring i) of probes. The total pressure $P(\theta)$ at an arbitrary angular location θ is obtained by linear interpolation between the two closest probes. PAV_i is then defined as the ring average total pressure and is computed using Eq. 2.17:

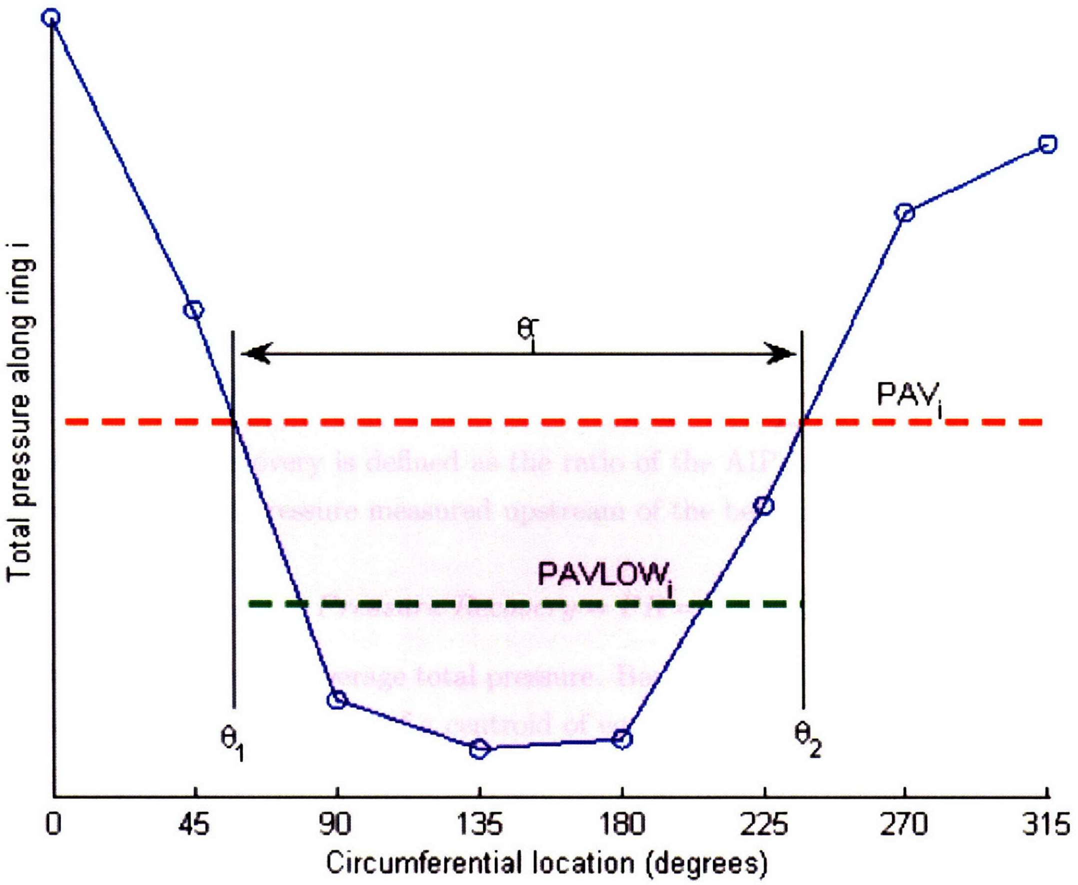

Figure 2-17: Typical ring total pressure plot

$$PAV_i = \int_0^{360} P(\theta)d\theta \tag{2.17}$$

The low pressure region, defined as the region where the total pressure is lower than PAV_i, is bounded by the angular locations θ_{1_i} and θ_{2_i}, with an extent θ_i^-. $PAVLOW_i$ is then defined as the average total pressure in the low pressure region and is computed using Eq. 2.18:

$$PAVLOW_i = \int_{\theta_{1_i}}^{\theta_{2_i}} P(\theta)d\theta \tag{2.18}$$

The $DPCP_{avg}$ is equal to the average of the ring distortion intensities and is defined by Eq. 2.19:

$$DPCP_{avg} = \sum_{i=1...5} (Intensity_i/5) = \sum_{i=1...5} \frac{1}{5} \left(\frac{PAV_i - PAVLOW_i}{PAV_i} \right) \tag{2.19}$$

where i is the ring number on the AIP rake and where $Intensity_i$ is introduced as a measure of the ring i distortion intensity. The radial distortion descriptor $DPRP_{max}$ is defined by Eq. 2.20:

$$DPRP_{max} = \max_{i=1...5}(DPRP_i) = \max_{i=1...5} \frac{P_{Te} - PAV_i}{P_{Te}} \tag{2.20}$$

Inlet pressure recovery is defined as the ratio of the AIP rake total pressure and the freestream total pressure measured upstream of the bellmouth (Eq. 2.21).

$$Pressure\ Recovery = PR = \frac{P_{Te}}{P_{T0}} \tag{2.21}$$

where P_{Te} is the AIP average total pressure. Because the IC total pressure probes are each located at the center of a centroid of equal area, P_{Te} is simply obtained by averaging the pressures read by the 41 probes.

$$P_{Te} = \frac{1}{41} \left(P_{0,0} + \sum_{i=1...5, j=1...8} P_{i,j} \right) \tag{2.22}$$

where $P_{i,j}$ is the pressure read by the probe located on the ring i and angular location j.

Chapter 3

Inlet Flow Characterization

This chapter presents the results obtained with the inlet in both the clean and the boundary layer ingesting configuration. The results of the bare inlet configuration serve to characterize the inlet in the most favorable conditions, i.e. uniform clean flow at the entrance. The results of the boundary layer ingesting inlet serve as a baseline for the controlled cases. The performance of the inlet is analyzed based on the pressure measurements mainly and the structure of the inlet flow is deduced from oil flow visualizations.

3.1 Bare inlet: flow structure

In this section, the results from the inlet with clean, uniform flow at the entrance are presented. The inlet performance is first described. The flow structure, deduced from oil flow visualization is then presented. The inlet performance is presented for the whole mass flow range. Oil flow visualizations can be carried out only at a few operating points, so the flow structure was studied at the design point only.

3.1.1 Flow structure in S-ducts

This inlet shape is not particularly aggressive, so good baseline performance was expected. Classical inlets typically have pressure recovery of 98% or better, the losses being mainly dominated by friction and lip separation at off-design conditions. For S-duct inlets like the one studied here, duct curvature introduces additional losses.

The offset in such inlets has two detrimental effects [35]:

- The streamline curvature in the bend of an S-duct inlet is also accompanied by a transversal pressure gradient, so that the pressure is higher on the outside than on the inside of the bend. This is explained by the generation of centrifugal forces, which are compensated for by a outward pointing pressure gradient, according to Eq. 3.1.

$$\frac{\partial p}{\partial r} = \frac{\rho u^2}{r} \tag{3.1}$$

where r is the radius of curvature, ρ the density and u the local fluid velocity. Due to its slower velocity ($u_{BL} < U_0$), thus lower momentum, the boundary layer is more sensitive to this pressure gradient. The balance of the forces on it will migrate it along the walls towards the inside of the bend more readily than the core flow, producing what is referred to as "secondary flows": According to Eq. 3.1, for the same pressure gradient ${}^{\partial p}/_{\partial r}$, for the same density but with a slower velocity, the radius of curvature of the boundary layer has to be smaller than that of the freestream, thus driving the upper boundary layer flow towards the inside of the bend. Figure 3-1 shows a schematic of the generation of secondary flows in a S-duct. This accumulation of boundary layer fluid at the inside of the bend will try to replace and push the fluid already there away from the wall toward the outside of the bend, thus producing a lift-off effect that worsens the separation.

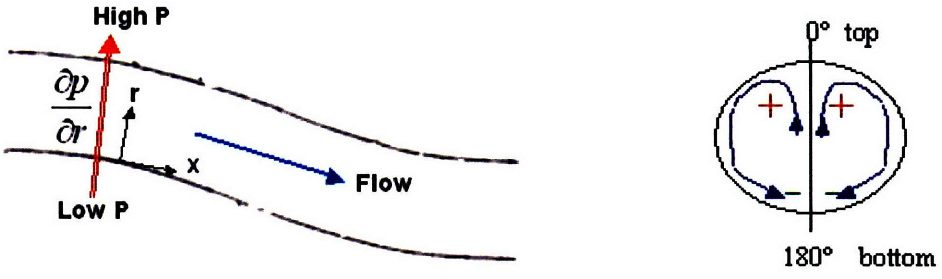

(a) side view

(b) cross-sectional view

Figure 3-1: Secondary flows in S-ducts

- The curvature at the first bend generates a local acceleration of the fluid, to which is associated a local pressure drop close to the bottom wall. Therefore, as the flow exits the first bend, the locally accelerated flow sees a much greater adverse pressure gradient than that inside a straight duct of same area profile. Boundary layer separation is consequently more likely to occur in the S-duct geometry, at the exit of the first bend. This phenomenon is very similar to what happens on a stalling wing, when the flow separates on the suction side of the wing after being locally accelerated.

The separation mechanism itself is shown in Fig. 3-2. The boundary layer fluid gradually loses its momentum under the effect of the adverse pressure gradient, until at some point, called the stagnation point, its velocity nullifies and is finally reversed. A separation bubble forms, where the fluid flows in the counter-streamwise direction.

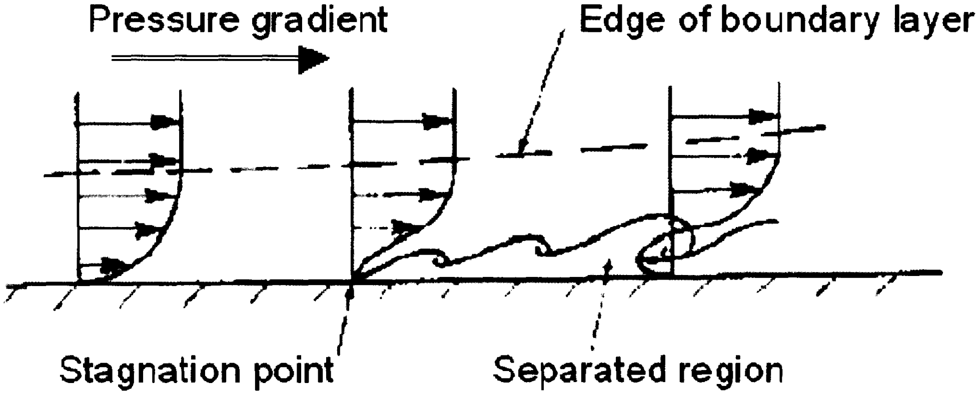

Figure 3-2: Boundary layer separation

It was found, as expected, that despite its not-so-aggressive geometry, the flow in this inlet separates at Mach 0.6.

3.1.2 Oil flow visualization

Since the flow structure and the inlet performance are intimately related, the motivation of the flow visualization experiments is to understand the physics of the flow.

The flow visualization method consists of applying a mixture of viscous silicon oil and black dye powder to the top and bottom surfaces of the inlet. After applying the oil, the inlet is quickly re-assembled into the experimental setup to ensure evenly distributed oil coverage. The flow visualization experiment requires raising the mass flow through the inlet as quickly as possible to ensure that the oil is not completely washed out before reaching the desired test condition. Similarly, it is important to allow the oil to dry at the desired mass flow before ending the experiment. Otherwise, the visualization becomes distorted by the characteristic of lower mass flows during the compressor shutdown.

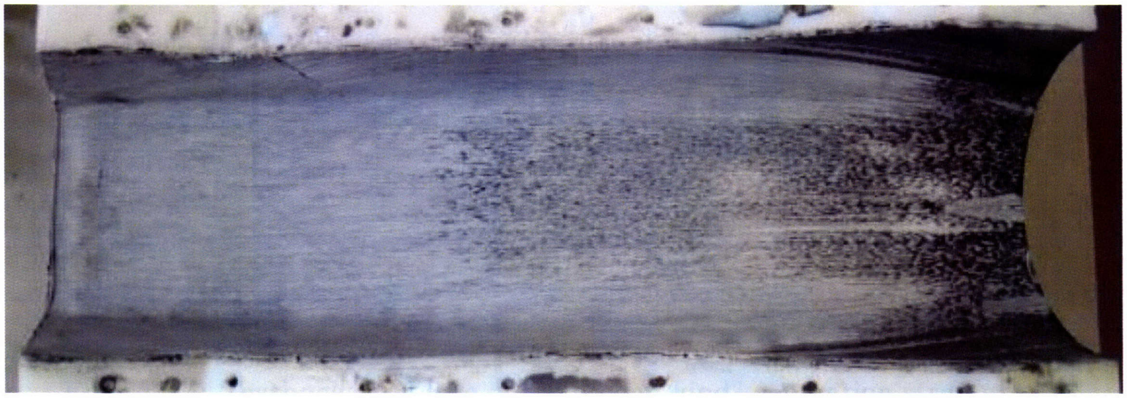

(a) upper part

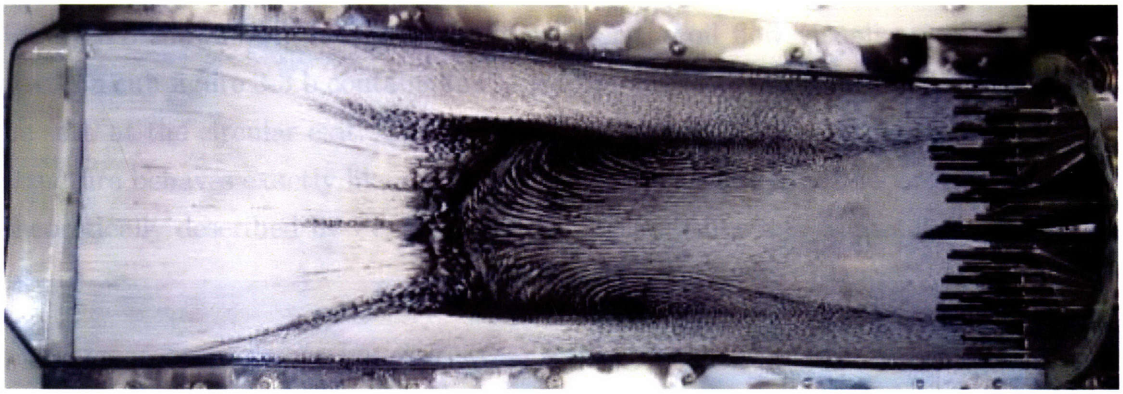

(b) lower part

Figure 3-3: Oil flow visualization results for the bare inlet configuration

During the experiment, the flow shear stress at the wall washes the oil and dye mixture out, convecting it downstream. But in region where the wall shear stress is small or null, the oil remains and stagnates. The visualization thus gives an idea of what the wall shear stress intensity is. The wall shear lines are always tangent to the shear direction and tend to align with the velocity lines [1]. Therefore, the oil flow visualization gives an idea of what the streamlines the closest to the wall look like.

The flow visualization results discussed in this section apply to the design point CMF of $1.67 kg.s^{-1}$.

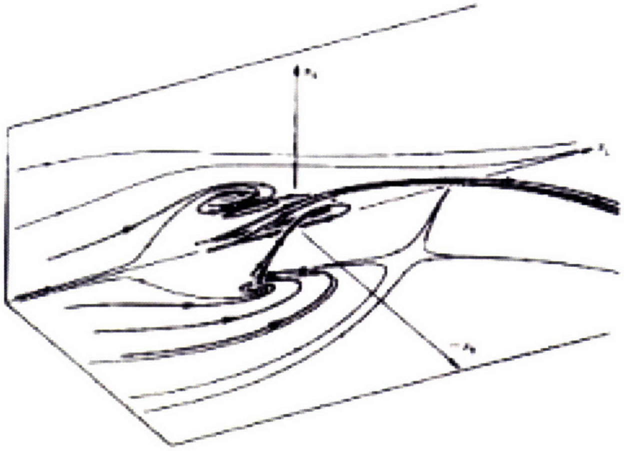

Figure 3-4: Textbook "owl face of the second kind" separation structure [2]

3.1.3 Boundary layer separation

Figure 3-3 shows both halves of the inlet after the oil flow visualization. The lower part, on sub-figure 3-3.b contains the separated region of the flow. The IC probes can be seen at the circular exit. The direction of the flow is from left to right. This flow structure behaves exactly like the "Owl face of the second kind" separation structure theoretically described by Perry and Chong [2] and shown in Figure 3-4.

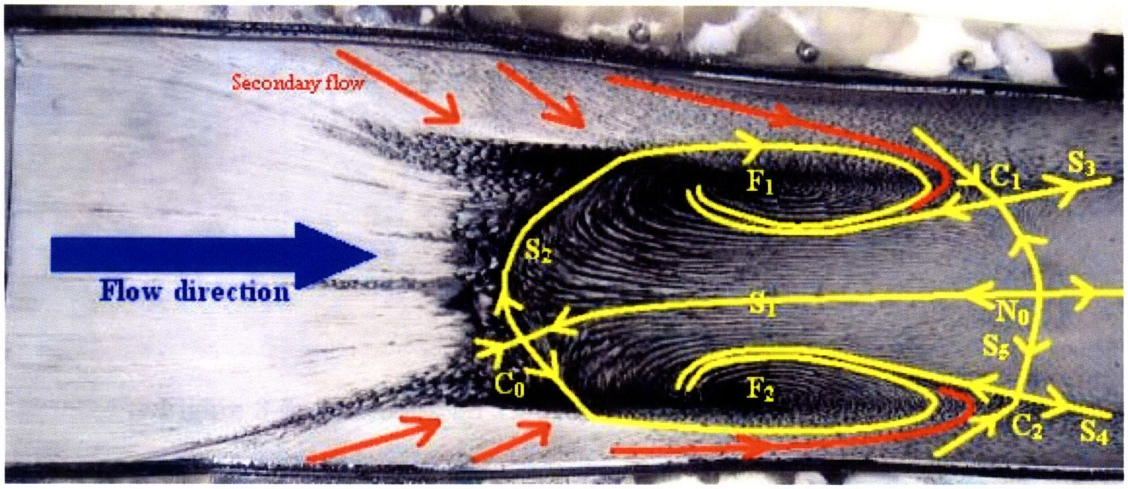

Figure 3-5: Oil flow visualization interpretation for the baseline case

In this structure, the separation produces twin vortices in the re-circulation zone. Figure 3-5 shows the separated region in detail, and the lines superimposed describe the main features of the flow as interpreted based on [1]. Figure 3-6 shows a 3-D schematic view of the separation structure. The notations refer to either Fig. 3-5 or Fig. 3-6, depending on the visibility of the element referred to.

The separation is a "one saddle, two foci" kind separation: S_1 and S_2 are two separating lines, C_0 is a saddle node, and the foci F_1 and F_2 are attractive. S_2 is the upstream limit of the separation bubble, and is made of the intersection of the separation surface Σ_2 and the wall. S_1 is the middle line in the separation bubble that separates the fluid streamlines that curl towards F_1 and F_2. C_0 is the intersection of the two separating lines, and is the only point where the shear stress actually goes to zero. In this configuration, the separation surface rolls up around two vertical lines (ζ is one of them) that emanate from F_1 and F_2.

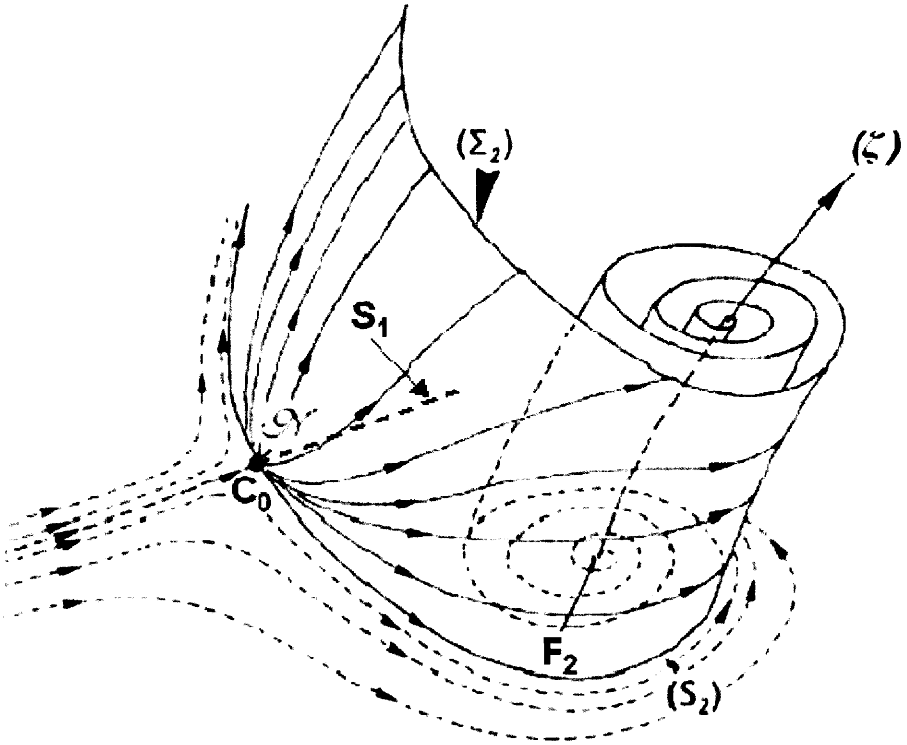

Figure 3-6: Textbook 3d-view of the separation structure [1]

At S_2, the incoming thick boundary layer takes off and follows the separation surface Σ_2: Considering a square tube of fluid with its corners being the two streamlines I_1 and I_2 and two shear stress lines f_1 and f_2 (see Fig. 3-7 for notations) with average speed $\overline{V}$, average density $\overline{\rho}$, width n and height h, the mass flow rate Q_m through it is given by Eq. 3.2.

$$Q_m = \overline{\rho} n h \overline{V} \tag{3.2}$$

When this tube arrives close to the separating line S_1, I_1 and I_2 and the shear stress lines f_1 and f_2 converge to the separation surface, so n approaches zero, and since $\overline{V}$ and $\overline{\rho}$ remain finite, and the mass flow rate is constant, then the height h goes to infinity according to Eq. 3.3.

$$h = \frac{Q_m}{\overline{\rho} n \overline{V}} \xrightarrow[S_1]{} \infty \tag{3.3}$$

Thus, incoming streamlines close to the wall go away from it, the boundary layer "takes off". They are also pushed aside in the spanwise direction.

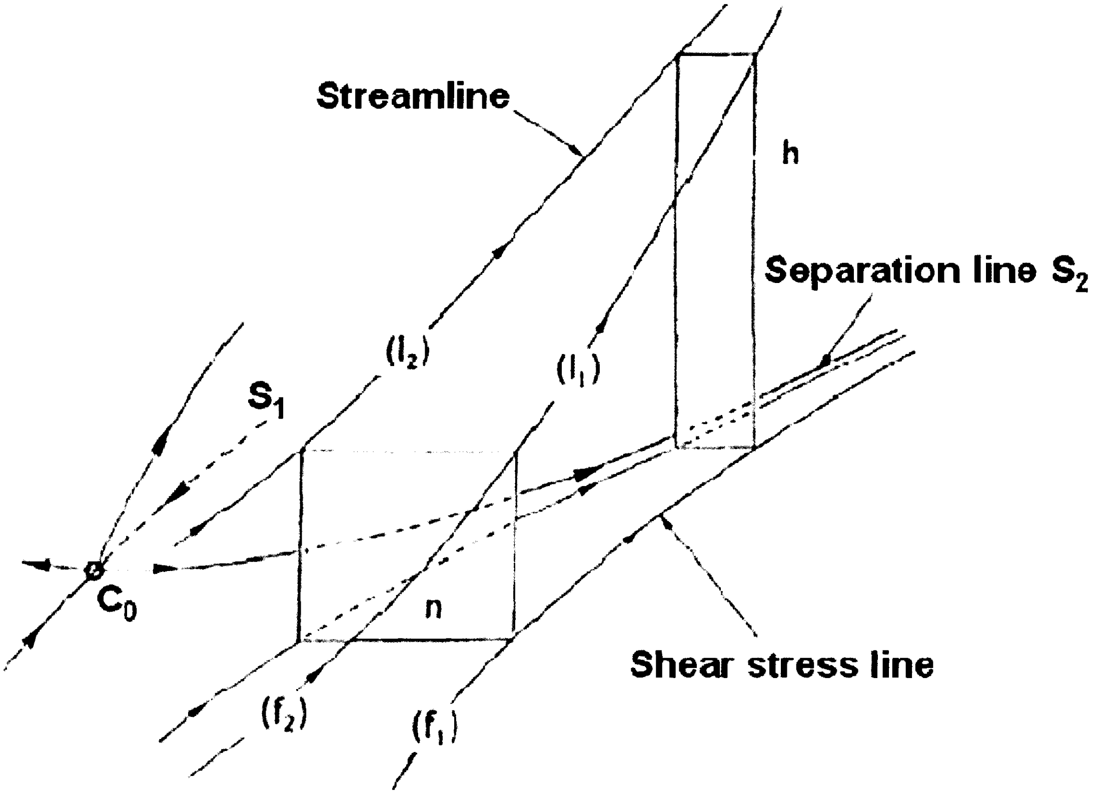

Figure 3-7: Textbook 3d-view of a boundary layer take off [1]

Figure 3-7 shows a schematic view of this phenomenon. The slight deviation of C_0 from the centerline in the oil flow visualization results is due to the instability of a symmetric configuration in real flows. Such dissymmetric configuration are much more stable.

3.1.4 Flow reattachment

More downstream, close to the exit, a "two saddle nodes, one diverging node" kind reattachment structure can be seen on Figure 3-5. This structure is characterized by the appearance of two supplementary saddle nodes C_1 and C_2, and of two separating lines S_3 and S_4, on each side of the separating line S_1 and of a reattachment line S_5. The line S_5 separates the reverse flow in the separation bubble from the reattached flow downstream. It also separates the flow that winds up around the foci from the flow that goes on downstream. The lines S_3 and S_4 are the roots of two separation surfaces (Σ_3 and Σ_4) that wind up around the foci, similar to the primary separation surface Σ_2 shown on Fig. 3-6.

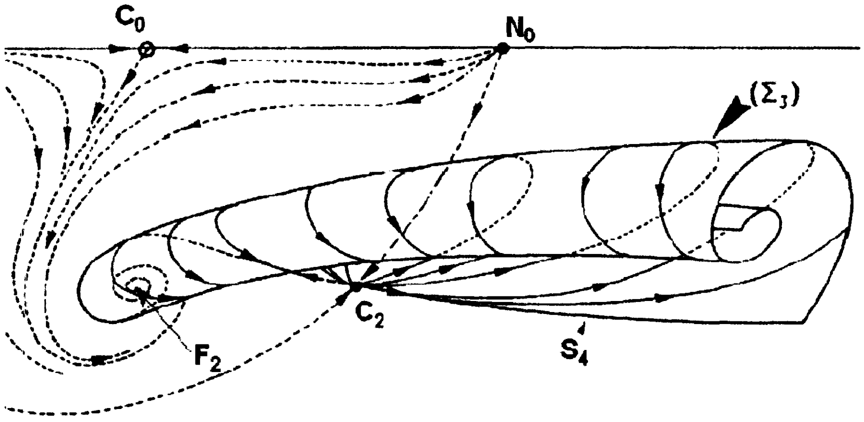

Figure 3-8: Textbook 3-D view of the reattachment structure [1]

The two outer branches S_3 and S_4 cannot end in the fluid [1] as they have to hit a surface or go to infinity. Whatever they do does not happen inside the test section and has no effect on the inlet flow. It should be noted that Poincaré's rule does not apply to this case, as this is not a closed surface.

$$\sum Nodes + \sum Foci - \sum Saddlenodes = 2 \tag{3.4}$$

Thus, Eq. 3.4 does not have to be respected in this case. Though the reversed flow region is closed as the flow reattaches, the two vortices that are generated at the foci F_1 and F_2 are stable features that convect downstream to the compressor face.

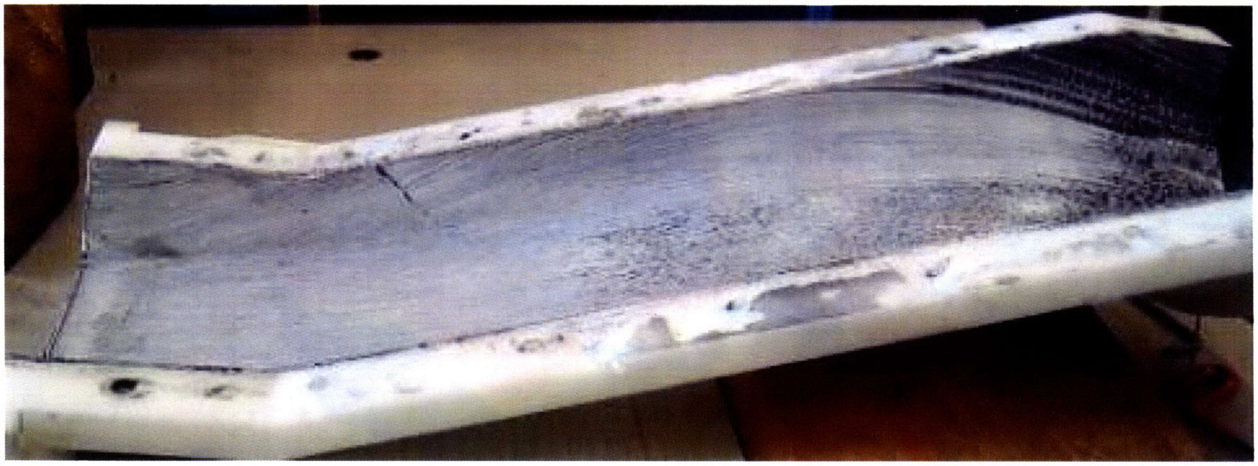

Figure 3-9: Secondary flows

3.1.5 Secondary flows

Figure 3-9 shows a side view of the upper inlet part after the oil flow visualization experiments. As can be seen, the flow is characterized by strong secondary flows that bend the streamlines from the upper to the lower part after the bend and then in the opposite direction right before the AIP. These deviations are due to the centrifugal forces generated in the two bends of the S-duct. The secondary flows participate in the structure of the separated area as part of the side incoming flow is ingested by the two foci, as shown on Fig. 3-5.

3.1.6 AIP flow properties

The flow features described previously impact on the flow properties at the AIP. Figure 3-10 shows a total pressure map at the AIP. The upper part of the AIP is quite unaffected by the distortion: the total pressure is nearly constant. There is a low total pressure region right at the top of it. This is a small area of thickened boundary layer, generated by the second curve of the inlet. The total pressure deficit at the bottom has a much larger area. It is symmetric, and spreads over nearly the whole radius of the AIP. It corresponds to the trace of the two vortices shed in the separation bubble. This low total pressure region is also characterized by a higher static pressure[1], as it corresponds to low-momentum boundary layer fluid accumulated here by the secondary flows.

---

[1] as measured by the wall static pressure ports at the circumference of the inlet exit

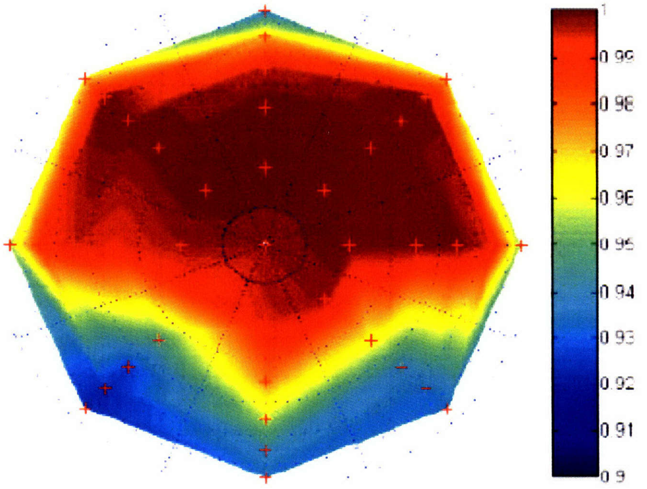

Figure 3-10: AIP total pressure map at $CMF = 1.67 kg.s^{-1}$ for the baseline case

The overall pressure recovery is high, $PR = 0.975$, in accordance to usual results for S-ducts of this type, and the distortion level is low, $DPCP_{avg} = 0.016$, way below the usual limit of $DPCP_{avg} = 0.05$. This inlet thus indeed features good AIP flow properties in the clean configuration at the design mass flow.

3.2 Bare inlet: CMF sensitivity

In this section, the variations of the inlet performance parameters with CMF is discussed. Pressure recovery, static pressure profile along the inlet centerline and AIP distortion are all quantified.

3.2.1 Pressure recovery

In this section, the relationship between AIP flow properties and CMF is studied. Figure 3-11 describes it over the mass flow range used in these experiments. Within the CMF operating range $[1.22 - 1.95] kg.s^{-1}$, the pressure recovery is quite high, lying between 94% and 99.5%. As can be seen on Fig. 3-11, the pressure recovery falls slowly with increasing Mach numbers, and around $CMF = 2.01 kg.s^{-1}$, the pressure recovery drops dramatically while the CMF stagnates, as the backpressure was lowered by opening the butterfly valve that leads to the suction source. This indicates that the inlet begins to choke at this CMF.

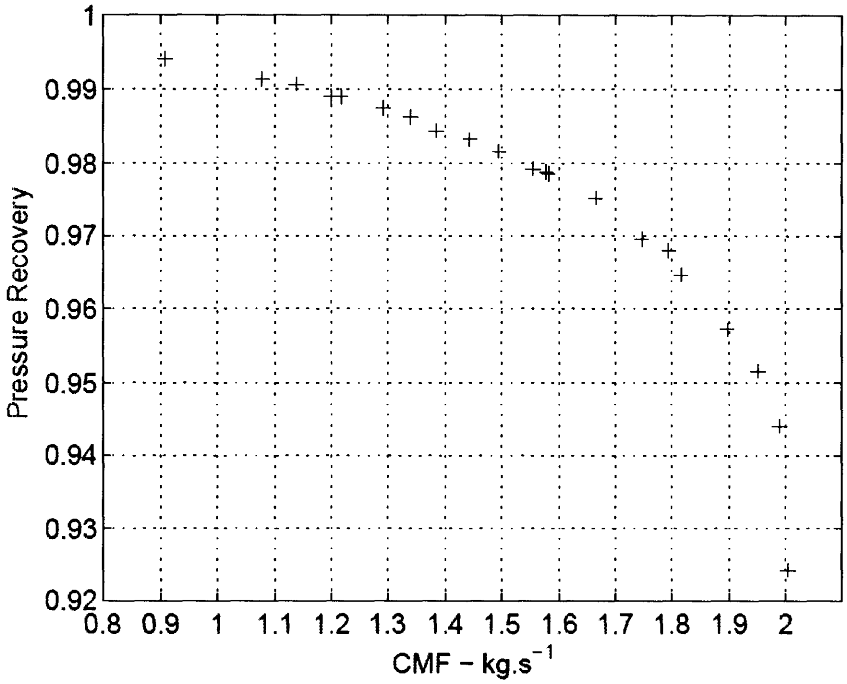

Figure 3-11: AIP Pressure recovery as a function of CMF for the baseline case

3.2.2 Pressure profile

The pressure profile refers to the static pressure evolution along the centerline of the inlet. It is expressed in terms of pressure coefficient (see section 2.4 for details). Figure 3-12 shows the pressure coefficient along the inlet centerline as obtained for different CMF. The station is the number of the static pressure port, when counted from the entrance of the inlet. The static pressure ports were set $1'' = 2.54cm$ apart on the inlet centerline, so that the station is also the curvilinear coordinate in inches of the pressure port. Several conclusions are to be drawn from these profiles:

- the highest CMF present extremely low pressure profiles,
- for CMF around the design CMF ($CMF = [1.22 - 1.82] kg.s^{-1}$), the pressure profile presents a plateau.

The decrease of the static pressure profile with very high mass flows is to be related to the fact that the inlet chokes at these CMF: as the flow reaches Mach=1 close to the first bend, the static pressure decreases dramatically and locally at the first port, effect that might also be amplified by the "suction side effect" that takes place at this location. It was also shown that a shock takes place in the first bend:

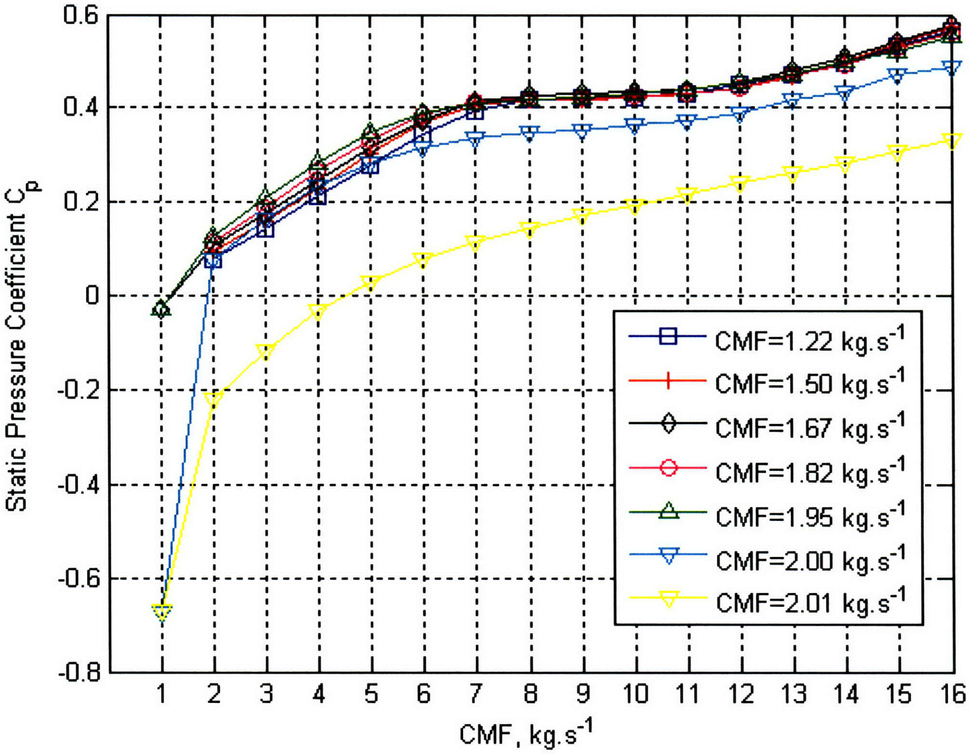

Figure 3-12: Pressure profile along centerline for the baseline case

The way the mass flow is set in the setup is by opening or closing the butterfly valve downstream of the test section. This increases or reduces the backpressure applied at the AIP, which decreases or increases the flow velocity and thus mass flow through the setup. For some opening of the butterfly valve (around 72%), though, the mass flow reaches its maximum and further opening of the butterfly valve does not have any effect on the mass flow anymore: As can be seen on Fig. 3-13, as the valve is further and further opened, the mass flow remains fixed at $CMF = 2.01kg.s^{-1}$. All the static pressure ports located upstream of the first inlet centerline port, such as the bellmouth centerline ones, read the same static pressure, as can also be seen on Fig. 3-13. It should be pointed out that the reference static pressure used to compute the pressure coefficient is taken at a pressure port upstream of the first inlet centerline port. Therefore, an equal pressure coefficient indeed implies an equal static pressure upstream of the first inlet centerline port.

But the static pressure profile downstream of the first port gradually decreases with decreasing backpressure. The explanation of this phenomenon is that once the

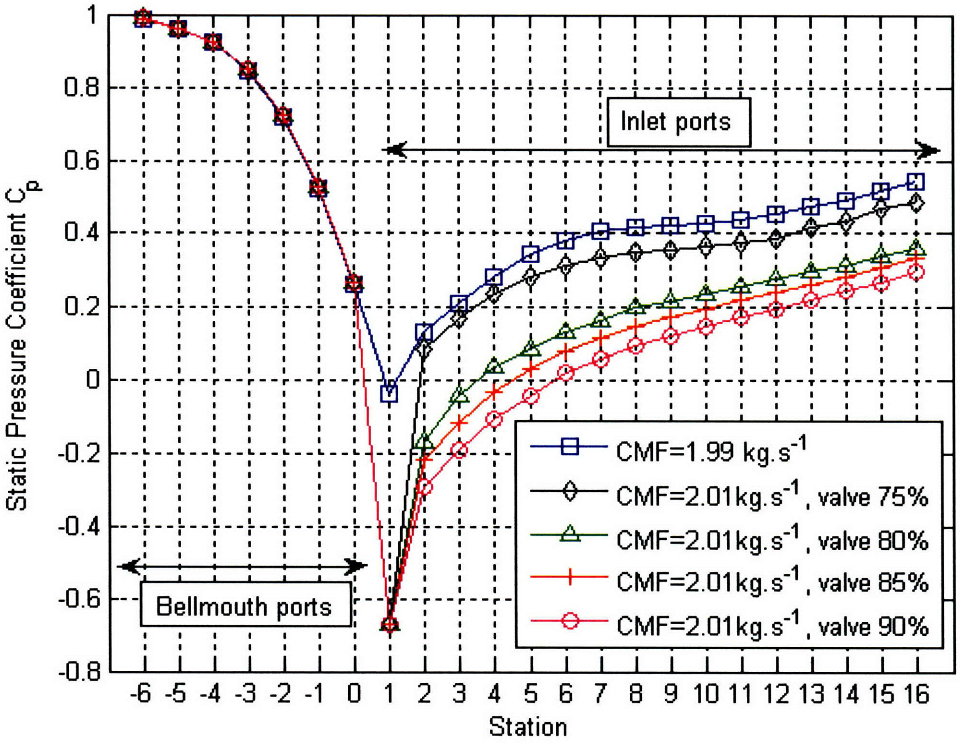

Figure 3-13: Inlet and bellmouth pressure profiles at choked conditions for the baseline case

inlet is choked, further lowering the backpressure generates supersonic flow immediately downstream of the choking point, which is then re-compressed through a shock to subsonic again in order to meet the imposed backpressure. This phenomenon is very similar to what happens during the starting of an inlet or of a wind tunnel. The presence of a shock of increasing strength explains why the AIP pressure recovery would decrease while the CMF would stay constant when the butterfly valve was more and more opened. As no information travels upstream of a shock, the static pressure reading upstream of the inlet would logically remain unchanged, as observed.

It is also interesting to note that the noise level during the runs was tremendously attenuated when the highest CMF were obtained, which is in agreement with the previous explanation: sound waves can not cross the sonic point, therefore none of the noise emitted by the machinery downstream of the inlet first bend could be perceived by the operators during the experiments.

3.2.3 Separation bubble location

The plateau on the static pressure profile actually denotes the position of the reverse flow area. Indeed, as the boundary layer takes off, the cross-sectional area dedicated to the freestream flow, referred to as the effective area, diminishes. This loss in effective area prevents the subsonic flow from compressing properly and the resulting static pressure rise is less than that obtained in a clean flow configuration, i.e. with no separation.

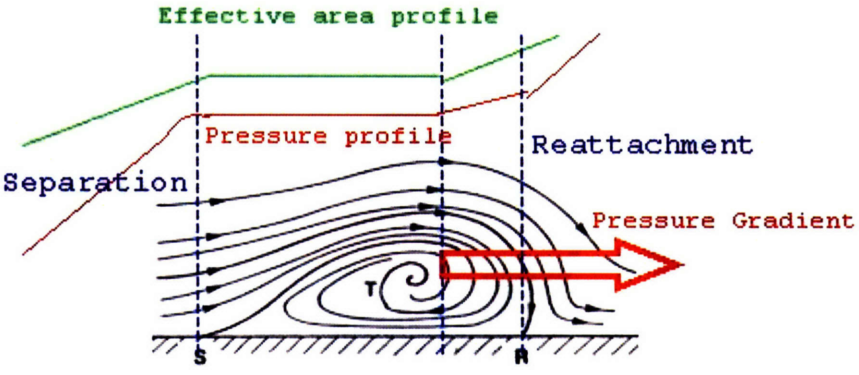

Figure 3-14: Pressure and effective area profiles at separation in duct flows

The separation can thus be approximately located for the various mass flows using the static pressure profile at the centerline. The wall static pressure ports being separated by an inch, a reasonable estimate is that the pressure plateau spreads between the 7^{th} and 11^{th} station, corresponding to x-coordinates of $0.167m$ to $0.279m$. The first edge of this plateau can be considered of the edge of the separation bubble. The reattachment edge is usually downstream of the end of the plateau. This is because when the bubble begins to thin out, the pressure rises again. The plateau associated with the separation bubble moves little with varying mass flows in the range $[1.22-1.82] kg.s^{-1}$, far from the choked conditions. The static pressure coefficient is locked at $C_p = 0.42$ at the plateau.

3.2.4 Distortion

The separation induces total pressure loss on the bottom half of the AIP, as shown on Fig. 3-15. This region grows in extent and pressure deficit as the mass flow is increased. The upper core stream remains quasi-undistorted for most of the operating range, except for a small region right at the top of the AIP which is due to the second

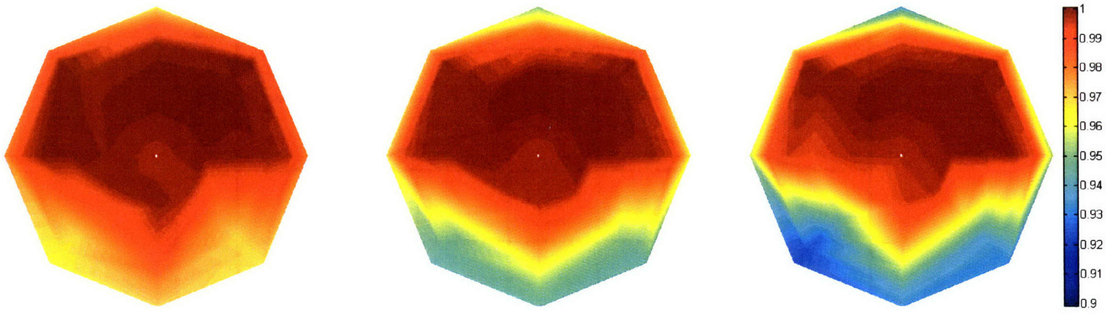

(a) $CMF = 1.22kg.s^{-1}$ (b) $CMF = 1.50kg.s^{-1}$ (c) $CMF = 1.67kg.s^{-1}$

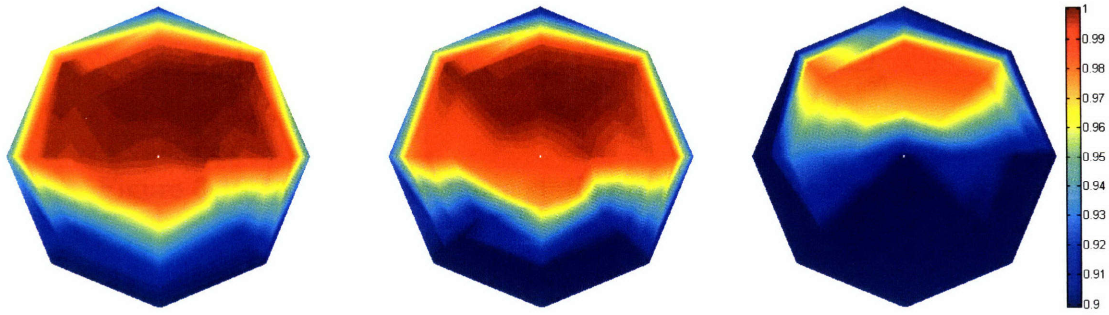

(d) $CMF = 1.82kg.s^{-1}$ (e) $CMF = 1.95kg.s^{-1}$ (f) $CMF = 2.01kg.s^{-1}$

Figure 3-15: AIP total pressure maps for the baseline case

inlet bend. For the upper end of the mass flow range, above $CMF = 1.95kg.s^{-1}$, the flow quality at the AIP deteriorates considerably as the inlet chokes and a shock takes place close to the throat. Finally, the secondary flows cause a total pressure loss that is visible on the sides of the AIP. The loss increases with the increasing mass flow.

Figure 3-16 shows the static pressure ratio at the circumference of the AIP, 0^o and 360^o being the top and 180^o the bottom of the inlet. The low total pressure region generated by the separation creates a high static pressure, due to the low velocity of the fluid in this region. The decrease of static pressure with increasing mass flow is a compressibility effect: as the total pressure of the flow is equal to the atmospheric pressure, and is consequently constant, increasing the mass flow leads to an increase in Mach number. The ratio $^{p}/_{P_T}$ being an decreasing function of the Mach number, increasing the mass flow leads to a decrease in static pressure.

Figure 3-17 shows the circumferential distortion, expressed in terms of $DPCP_{avg}$ as a function of CMF. The distortion level remains low, way below the $DPCP_{avg} =$

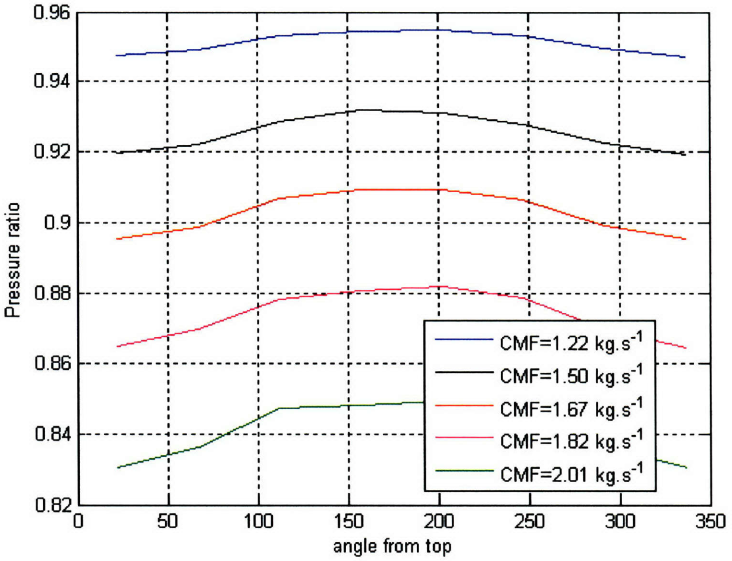

Figure 3-16: AIP circumference static pressure for the baseline case

0.05 usual limit, except for the choked conditions.

Overall, this inlet exhibits good performance: the pressure recovery is high and the distortion level is low. In regular conditions, it would not specifically require any control system. The distortion generator that was later placed at the entrance of the inlet to simulate the ingestion of a thick boundary layer, however, creates flow conditions justifying the use of flow control control techniques. This is the subject of the remainder of this chapter.

3.3 BLI configuration : flow structure

This section presents the characterization of the inlet in distorted entrance flow conditions. A screen was used to generate a total pressure loss at the bottom part of the entrance in order to simulate forebody boundary layer ingestion. This distortion greatly affected the inlet flow. Some details are first given on the screen design. The flow structure in the inlet and the inlet performance are then presented, based on oil flow visualization and pressure measurements. This flow was characterized to provide inputs to the flow control design.

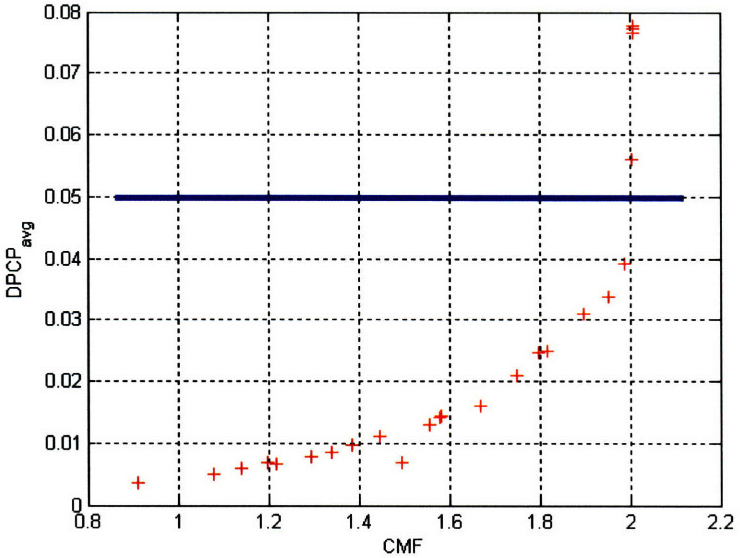

Figure 3-17: Circumferential distortion as a function of CMF for the baseline case

3.3.1 Screen design

The parameters used to characterize the distortion to be introduced at the entrance of the inlet were:

- its height δ, which should represent 15% of the inlet entrance height: $^{\delta}/_{h} = 15\%$,
- the total pressure loss should represent 20% of that of the incoming flow $^{\delta P_t}/_{P_0} = 20\%$.

These are based on previous CFD results obtained at MBDA on similar configurations. All of the parameters were chosen at the design point, which corresponds to an inlet CMF value of $CMF = 1.67 kg.s^{-1}$.

The most common way to generate distortion is to use a screen [48, 49]. The design of the screen is largely inspired by Bruce's paper [49] and Koo's article [50]. When fluid passes through a screen, the static pressure drops to overcome the viscous forces exerted by the screen wires. The reduction in pressure can be expressed by the dimensionless pressure drop coefficient K, defined by Eq. 3.5.

$$\Delta p = K \frac{1}{2} \rho u^2 \tag{3.5}$$

where Δp is the static pressure drop across the screen, ρ the fluid density and u its tangential velocity with respect to the screen. K may be related to the screen

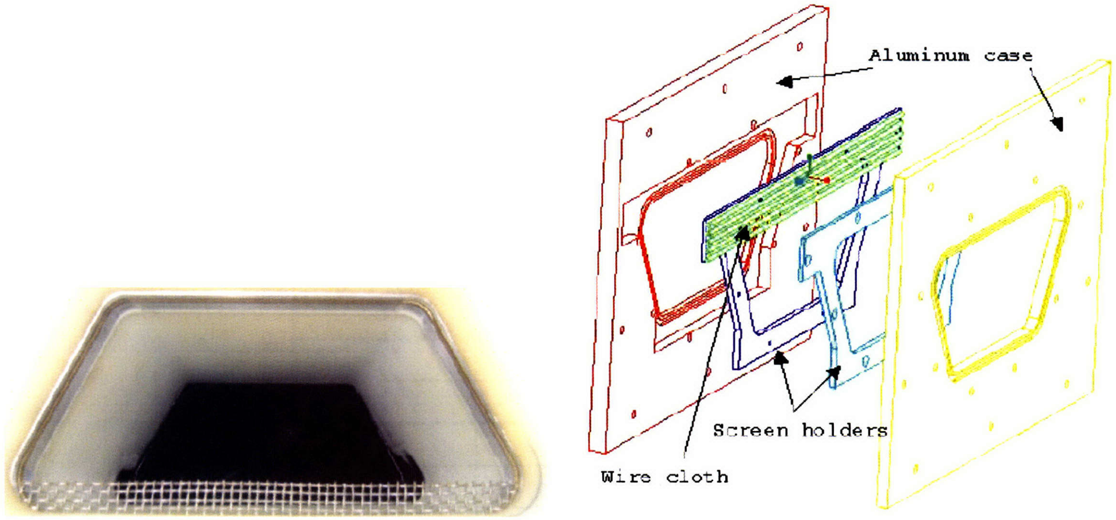

(a) photograph of the screen in place (b) CFD view of the screen holders

Figure 3-18: The distortion screen setup

solidity s, defined as the ratio of blocked area to total area, by Eq. 3.5.

$$K = \frac{cs}{(1-s)^2} \tag{3.6}$$

where c is a loss coefficient which is an empirical function of the Reynolds number Re based on the wire diameter d and the interstitial velocity through the screen u_{int}.

$$u_{int} = \frac{u}{(1-s)} \tag{3.7}$$

$$Re = \frac{u_{int} d}{\mu} \tag{3.8}$$

Based on experimental data, researchers found that for square mesh wire screens, c initially decreased with increasing Reynolds number, then leveled off at about 0.8 in the range $600 < Re < 4000$, and then rose gradually to a value of 1.00 at $Re \approx 15\,000$. Given this set of rules, it was straightforward to determine which commercially available wire cloth was suited for this application.

The wire cloth was then mounted on specially designed brass brackets that could slide into a leakage-free aluminum case. The aluminum case itself would be mounted between the bellmouth and the constant area duct. Figure 3-18 shows a photographic view of the screen mounted on the setup.

3.3.2 Screen distortion characterization

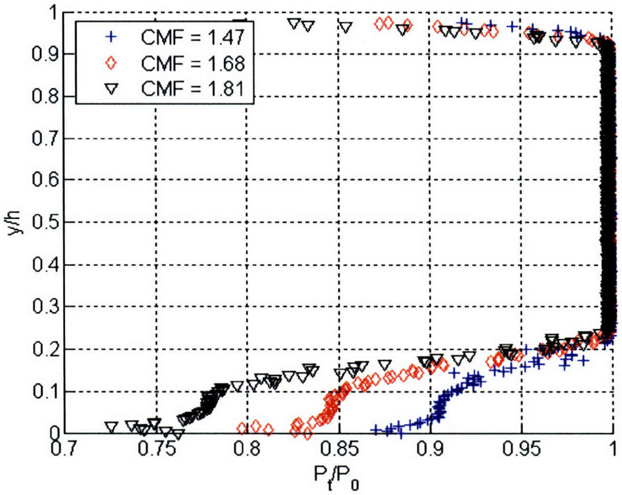

Figure 3-19: Screen pressure recovery

The traverser setup described in section 2.2.2 was used to scan the total pressure at the entrance plane of the inlet and characterize the distortion introduced by the screen. The screen was set at the bellmouth exit flange, 17.78cm upstream of the inlet entrance. The total pressure probe scanned the total pressure on a plane located 3.175cm upstream of the inlet entrance plane and 14.605cm downstream of the screen location.

Figure 3-19 shows the total pressure as a function of the inlet entrance height, in non-dimensional parameters. The boundary layers at the bottom and top of the inlet are clearly visible. At the design CMF ($CMF = 1.67kg.s^{-1}$), the total pressure loss introduced by the screen is about 15% on the first 10% of the inlet entrance height. The shear layer extends the screen effect up to about 20% of the screen height. Given the approximate nature of MBDA's characterization of the desired distortion to simulate, this distortion level was deemed sufficient, even though it did not exactly meet the aforementioned requirements.

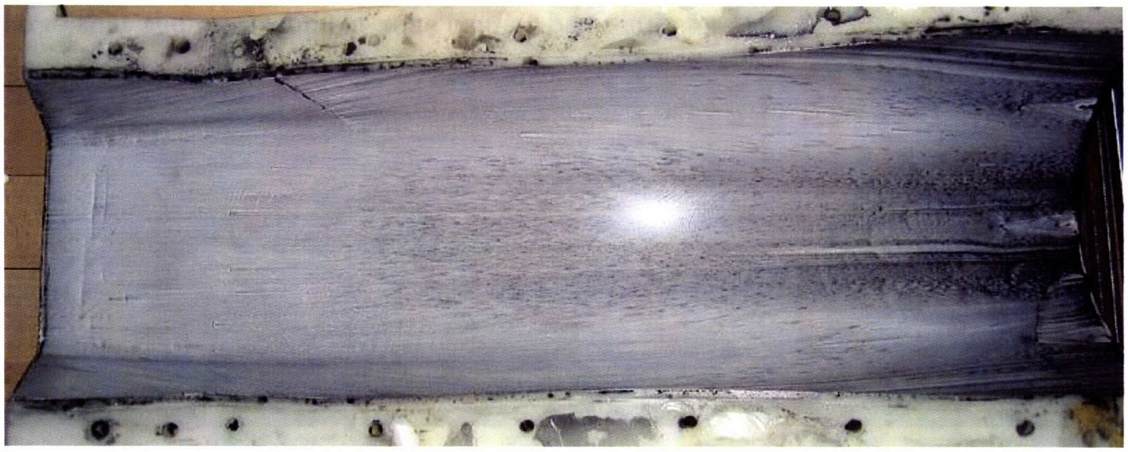

(a) upper part

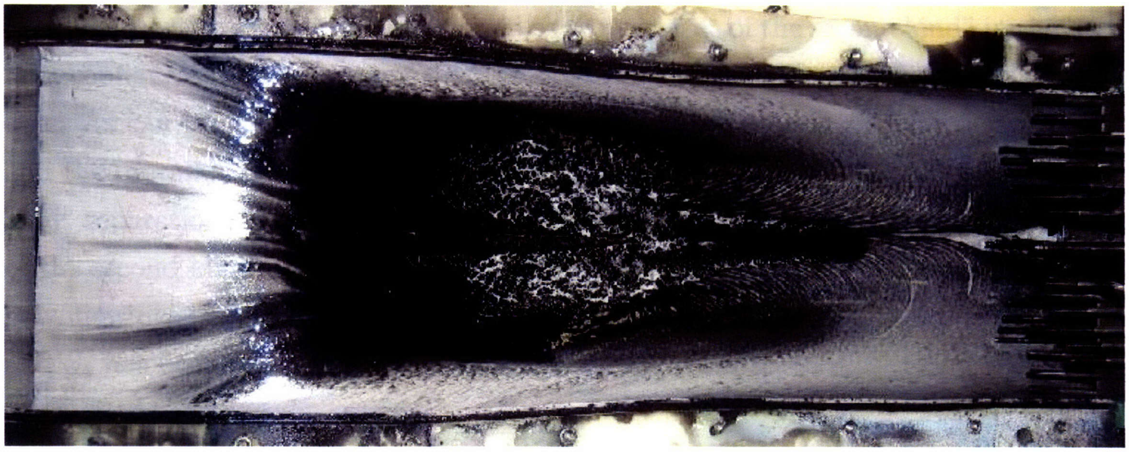

(b) lower part

Figure 3-20: Oil flow visualization results for the BLI configuration

3.3.3 Oil flow visualization

The presence of the screen at the entrance of the inlet significantly modifies the flow in the inlet. Figure 3-20 shows the oil flow visualization results for the design mass flow $CMF = 1.67 kg.s^{-1}$. The direction of the flow is from left to right. As can be seen, the separation structure is greatly affected by the presence of the screen: the separation line moves upstream and the vortices structures doubles in size. The massively recirculating flow draws all the oil to the separation line, erasing much of the shear spectrum at this location. However, two large vortex prints are clearly visible downstream of the separation line. The size of the separation structure is so large that the reattachment zone cannot be seen before the AIP.

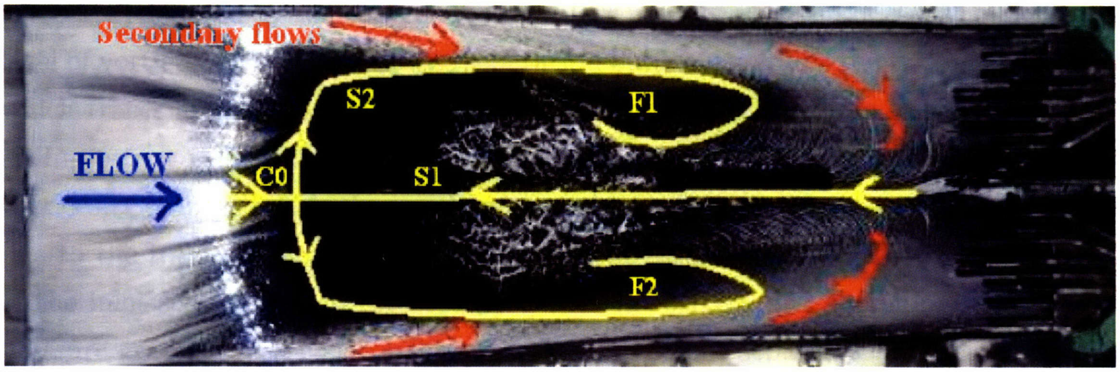

Figure 3-21: Oil flow visualization interpretation for the BLI configuration

The separation structure, recognized as an "owl face of the second kind" in the bare inlet configuration case (see section 3.1), becomes an "owl face of the first kind" in this case. As can be seen on Fig. 3-21, the separating lines S_3 and S_4 have disappeared, and the overall structure compares perfectly with the textbook "owl face of the first kind" separation structure shown on Fig. 3-22. The main difference from the "owl face of the second kind" structure, shown on Fig. 3-5, is that the area of purely reversed flow, flowing straight in the counter-streamwise direction between separating lines S_3 and S_4 has been taken over by the enlarged vortex prints.

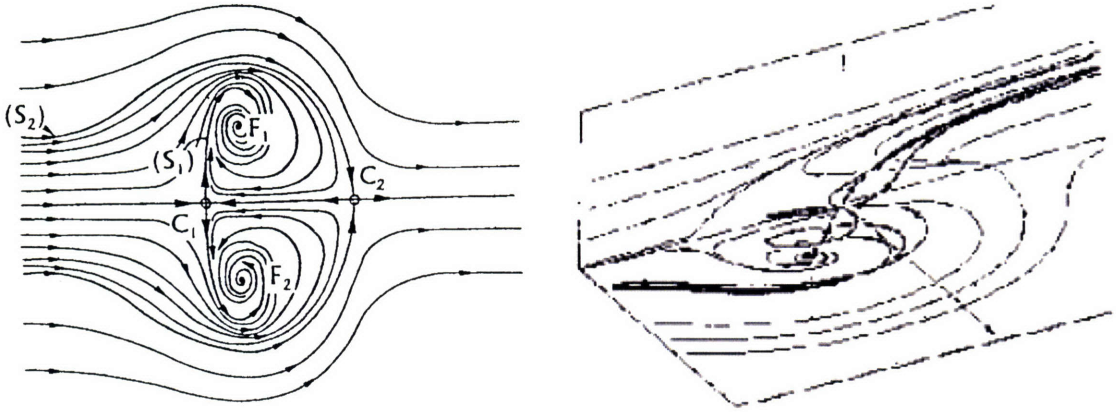

(a) shear spectrum [1]

(b) 3-D schematic view [2]

Figure 3-22: Textbook "owl face of the first kind" separation structure

Figure 3-21 shows the separated region in details, and the lines superimposed describe the main features of the flow as interpreted based on [1]. The flow separates at the upstream edge of S_2, and the boundary layer takes off. A zone of reversed flow is created, denoted by the thick deposit of black dye downstream of S_2. The increased level of vorticity at the edges of the separation bubble generates the two large vortices which traces are clearly visible downstream. The secondary flows also seem to play an important role in the separation structure, as they are largely entrained in the vortices. Compared with the baseline case, the separation line has moved upstream: due to the total pressure loss introduced by the screen, the flow in the bottom part of the inlet sees a static pressure drop across the screen, and therefore sees a larger pressure gradient in the streamwise direction, and thus separates earlier in the duct. The separation bubble also doubled in size, and now takes about $^{3}/_{4}$ of the inlet length.

3.3.4 Separation location

The static pressure profiles shown on Fig. 3-23 confirm the behavior of the separation structure: the effect of the screen translates into a much larger plateau, which subsequently allows much less duct length for static pressure increase before the AIP.

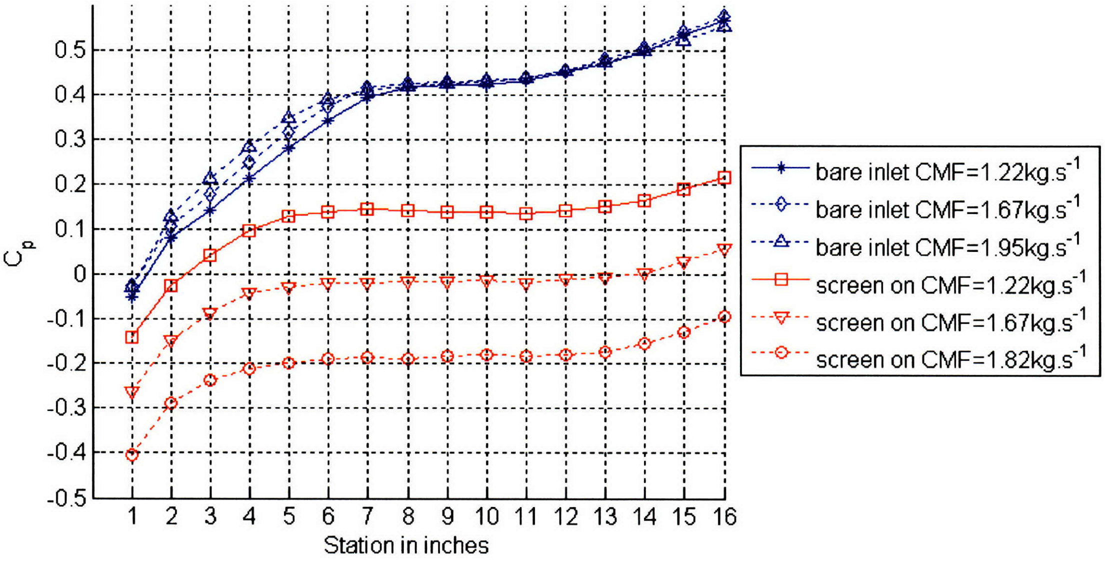

Figure 3-23: Static pressure profiles for bare and "screen on" configurations

The separation line was located using the pressure and the oil flow visualization data at the curvilinear coordinate $s = 10.16cm$ from the inlet entrance, approximately $7.62cm$ upstream of that of the bare inlet configuration. This location is an important parameter for the control techniques implementation. The size of the plateau is essentially constant with the varying mass flow.

3.4 BLI configuration: performance

In this section, the effect of the screen on the performance of the inlet is discussed.

3.4.1 Pressure recovery

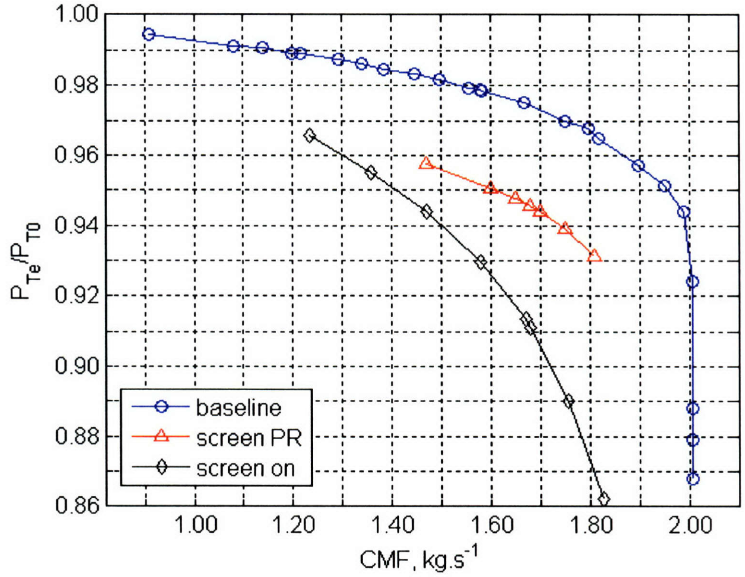

Figure 3-24: Pressure recovery for the bare and the "screen on" configurations

The effect of the ingested total pressure deficit on the inlet performance is important, as shown by Fig. 3-24. The pressure recovery plot shows the baseline PR, the screen PR, i.e. the pressure recovery through the screen taken at the inlet entrance and the resulting inlet PR taken at the AIP: The pressure recovery of the inlet drops from 97.5% to 91.3% at the design point, for a net loss of 6.13%. The total pressure loss introduced by the screen is only about 2.8% at this point. The S-duct therefore dramatically amplifies the screen loss. Moreover, the net loss increases with increasing CMF: 2.5% for the lower end of the operating range, 6.13% at the design point ($CMF = 1.67 kg.s^{-1}$), up to approximately 10% for the higher end of the operating range.

The losses attributed to the S-duct (induced losses) also represent the potential improvement margin ideally realizable by passive (no energy input) control means. The term "improvement margin" refers to the ideally possible pressure recovery gain via passive means, after one accounts for the total pressure loss across the distortion screen.

3.4.2 Distortion

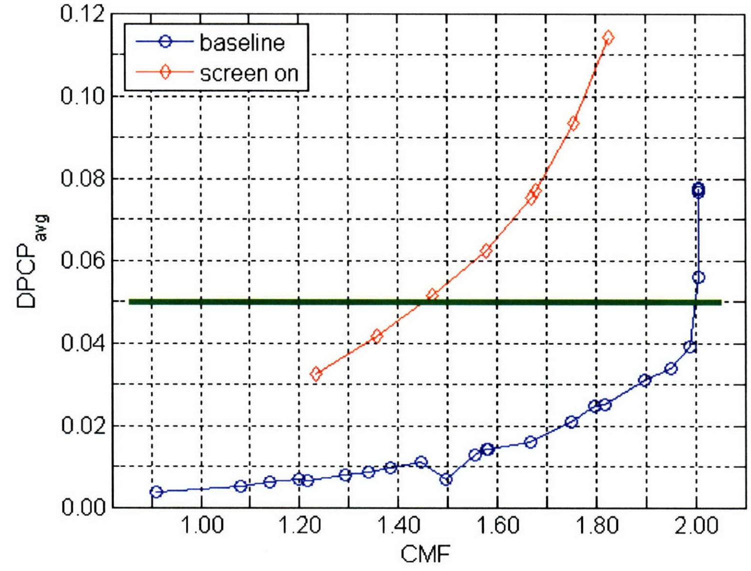

Figure 3-25: Circumferential distortion for the bare and the "screen on" configurations

The $DPCP_{avg}$ (standard circumferential distortion descriptor, see section 2.4.2) plots shown on Fig. 3-25 shows a dramatic increase in the distortion levels, way above the 0.05 commonly used limit for most of the operating range. The trend is also an increase with increasing CMF. Indeed, the separation has a strong effect on the flow at the AIP, as can be seen on the total pressure maps shown in Fig. 3-26. The low total pressure area takes almost 50% of the lower AIP area, generating a large circumferential distortion along any given ring.

Given this loss of performance, there is definitely a need for performance improvement in this "screen on" case, both in terms of distortion and PR.

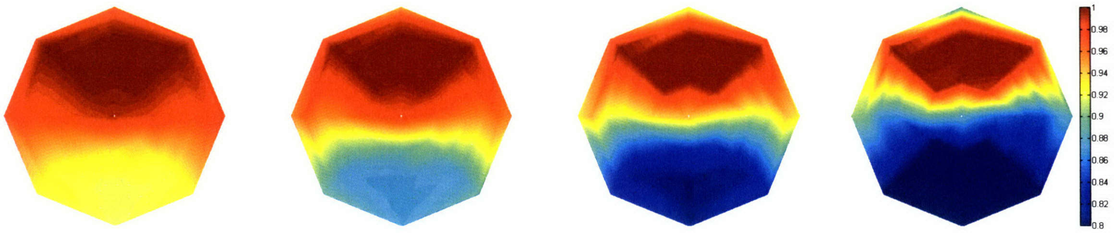

(a) $CMF = 1.22kg.s^{-1}$ (b) $CMF = 1.50kg.s^{-1}$ (c) $CMF = 1.67kg.s^{-1}$ (d) $CMF = 1.82kg.s^{-1}$

Figure 3-26: AIP total pressure maps for the “screen on” case

Chapter 4

Control Implementation

In Chapter 3, the inlet in the boundary layer ingestion case was characterized, and a net loss of performance, both in terms of pressure recovery and distortion at the AIP, resulted from the simulated off-design conditions. This chapter presents the control techniques that have been implemented and tested to improve the inlet performance. To provide an overview of available flow control techniques, both passive and active flow control techniques have been tested, respectively Vortex Generators and steady and periodic injection upstream of the separation line. Specifically, the flow control techniques design and their results are presented. A comparative analysis is also provided.

4.1 Vortex Generators

VGs have received a great deal of interest as an efficient way to reduce and eliminate separation both in external and internal aerodynamic applications. Their relative simplicity of implementation make them particularly attractive, as they require no tubing nor complex sub-system. Therefore, the first attempt to improve the performance of the inlet was done using Vortex Generators, which have proved quite efficient at delaying separation [29],[30],[31]. This section describes how the Vortex Generator technique was applied to the BLI inlet and presents the results obtained.

4.1.1 VG design

VGs are basically little vanes of various shapes (rectangular, triangular, arch-shaped...) that protrude from the wall surface and are scaled to the size of the boundary layer.

VGs have been shown to be efficient at reducing separation, working in two ways:

- The trailing vortices that they generate in a flow introduce streamwise vorticity that enhances the mixing between the low-momentum fluid from the boundary layer and the high-momentum fluid from the freestream. To generate this streamwise vorticity, the VGs have to be inclined at an angle to the incoming flow. The phenomenon is very similar to the generation of streamwise vortices by an airfoil with incidence. The beneficial consequence is the re-energizing of the boundary layer, which can subsequently withstand a steeper pressure gradient. The detrimental consequence is parasitic drag.
- VGs can also be used to manage the secondary flows. In this case, they are arranged to redirect the flow stream and redistribute the boundary layer evenly.

Three VG configurations have been tested in this project, and followed the two approaches: The first VG arrangement was designed to enhance mixing, the second and third arrangements were designed to manage the secondary flows. All of the VGs that have been used in this study are rectangular. Figure 4-1 shows one of the VGs in use.

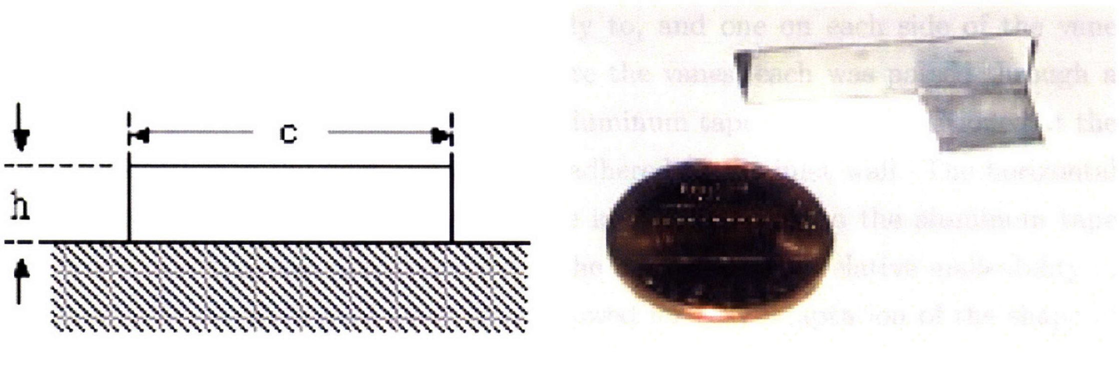

(a) Geometric details

(b) a VG

Figure 4-1: The VGs in use

Their geometry and placement is largely inspired from [29]. Scaled to this inlet, they have a height h=0.635cm (about half the height of the distortion introduced by the screen), have a low-profile aspect ratio of $h/c = 0.259$, and make a 16^o angle with the flow, independent of the specific arrangement implemented. "Arrangement" refers to the way the VGs are positioned with respect to one another. Two arrangements

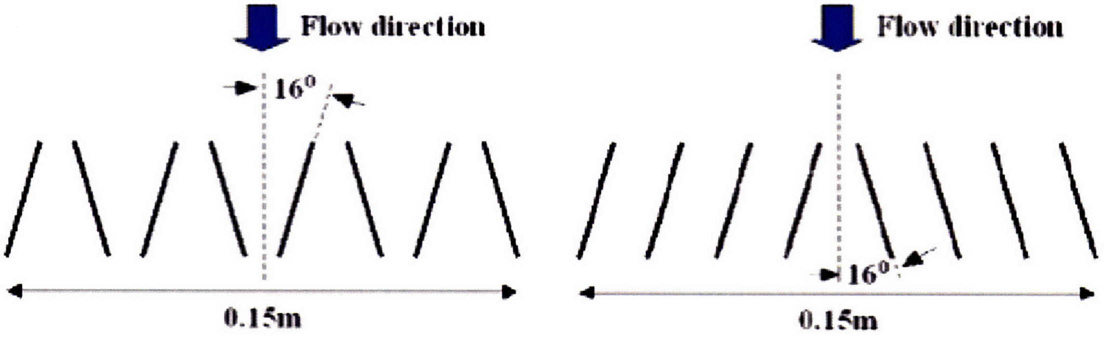

(a) Counter-rotating

(b) Co-rotating

Figure 4-2: Counter- and co-rotating VG arrangements

have been tested: a counter-rotating arrangement, and a co-rotating arrangement. Figure 4-2 shows both arrangements.

The VGs were spaced evenly on the largest base of the trapezoid that forms the entry, across the whole span of it. Assembled in sets of 8 VGs, the mean space between them was $5mm$, which with the spanwise extent of each VG, makes a total span of $0.15m$. The VGs were cut from thin aluminum plate and fashioned with two legs, which were folded perpendicularly to, and one on each side of the vane surface, as shown on Fig. 4-1.(b). To secure the vanes, each was passed through a slot cut in a piece of aluminum tape. The aluminum tape was then positioned at the required location in the inlet and securely adhered to the inlet wall. The horizontal legs, sandwiched between the tape and the inlet wall, stuck to the aluminum tape and firmly held the vane perpendicular to the inlet wall. The relative malleability of the aluminum the VGs were made from allowed for easy adaptation of the shape of the legs to the curved inlet wall. This technique had the immense advantage of not requiring any drilling or machining on the SLA inlet parts, which were shown to be quite brittle parts. The assembly proved very reliable, even at the highest inlet mass flow. See Fig. 4-8 for a top view of the VGs, which clearly shows the legs underneath the aluminum tape.

The location of the VG sets were determined using the scaling provided in [29]. Two locations were tested, either alone or at the same time depending on the arrangement:

- the first (denoted location 1 in Table 4.1) was upstream of the separation line (curvilinear coordinate s=5.08cm), with the idea to give the mixing sufficient time to develop before the separation line,

- the second (denoted location 2 in Table 4.1)was further downstream inside the separation bubble (curvilinear coordinate s=15.24cm), with the idea of maintaining the boundary layer attachment.

The VG sets were arranged along a line perpendicular to the freestream direction, as shown on Fig. 4.1. Table 4.1 sums up the configurations tested.

Table 4.1: The VG configurations tested

	VG arrangements	Location 1	Location 2
Configuration# 1	Counter-rot.	*Yes*	*Yes*
Configuration# 2	Co-rot.	*Yes*	*No*
Configuration# 3	Co-rot.	*Yes*	*Yes*

4.1.2 VG results

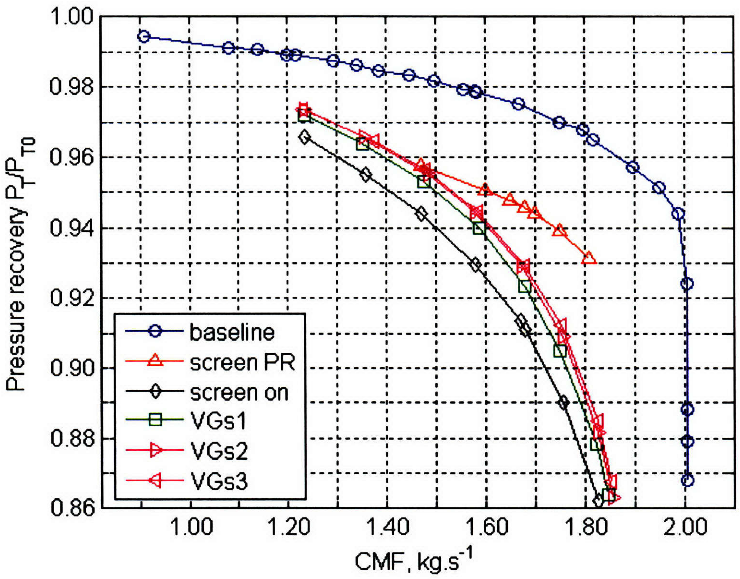

Figure 4-3: Pressure recovery for the VG-controlled cases

Figure 4-3 shows the pressure recovery as a function of the mass flow for the three VG configurations tested, along with the baseline, inlet entrance and "screen on" case for comparison. The immediate conclusion is that all the VG configurations tested led to some improvement in the pressure recovery. At the design point

($CMF = 1.67 kg.s^{-1}$), the VG configurations 1, 2 and 3 respectively achieved a pressure recovery gain of 1.1%, 1.8% and 1.82%, which represent 38% to 57% of the available improvement margin. The tendency is clearly that at higher the mass flow the benefit of the VGs becomes less pronounced: the efficiency of the VGs decreases with increasing CMF, being negligible in the upper part of the operating range.

There is a net (30%) superiority of the second and third VG configurations (the co-rotating arrangements) to the first one (the counter-rotating arrangement). The third configuration, where two sets of co-rotating arrangements were set upstream of the separation line and repeated further downstream, is the most efficient one.

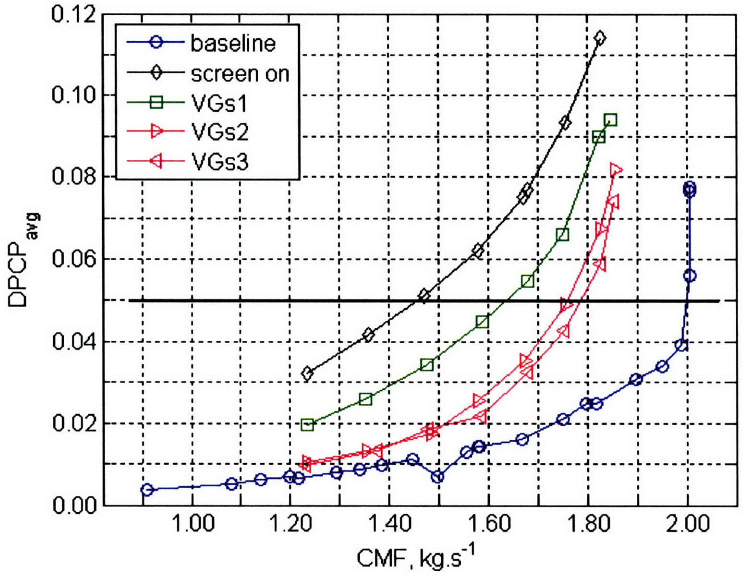

Figure 4-4: Circumferential distortion for the VG-controlled cases

The effect of the VGs on the distortion level is quite interesting: the three configurations proved very efficient at reducing the distortion level, but only the two co-rotating configurations (configurations 2&3) were able to bring the distortion level significantly below the 0.05 limit for most of the operating range, and in particular at the design point. The most efficient configurations is the third, which corresponds to the co-rotating configuration with two sets of VGs placed upstream of the separation line and repeated further downstream. The resulting distortion is close to that of the baseline case for the lower part of the CMF range, where it is about 0.01. It reaches 0.035 at the design point, compared to 0.016 for the baseline case, 0.0753 for the "screen on" uncontrolled case and respectively 0.0549 and 0.0355 for the VG1 and VG2 cases. For the higher end of the CMF range, the distortion level increases rapidly. The co-rotating configurations therefore proved twice as efficient as the counter-rotating one at reducing the AIP distortion.

Some insights into the higher efficiency of the co-rotating configuration are provided by the analysis of the static pressure profiles shown on Fig. 4-5 for the design point ($CMF = 1.65kg.s^{-1}$). Results for the three VG configurations tested are shown, along with the baseline and "screen on" cases. As can be seen, the counter-rotating configuration profile still features a plateau characteristic of a separation bubble. However, this plateau has been moved considerably downstream compared to the "screen on" uncontrolled case. It can be deduced that the counter-rotating configuration managed to delay separation, resulting in the pressure recovery improvements discussed earlier. But on the co-rotating configuration profiles, no clear plateau can be seen, and a linear static pressure increase is kept in the S-duct.

It can therefore be deduced that the co-rotating configuration was successful in greatly reducing the separation blockage (effective area reduction) effect. The secondary flows, which the co-rotating configuration was designed to manage, thus prove to have an important role in the occurrence and importance of the separation.

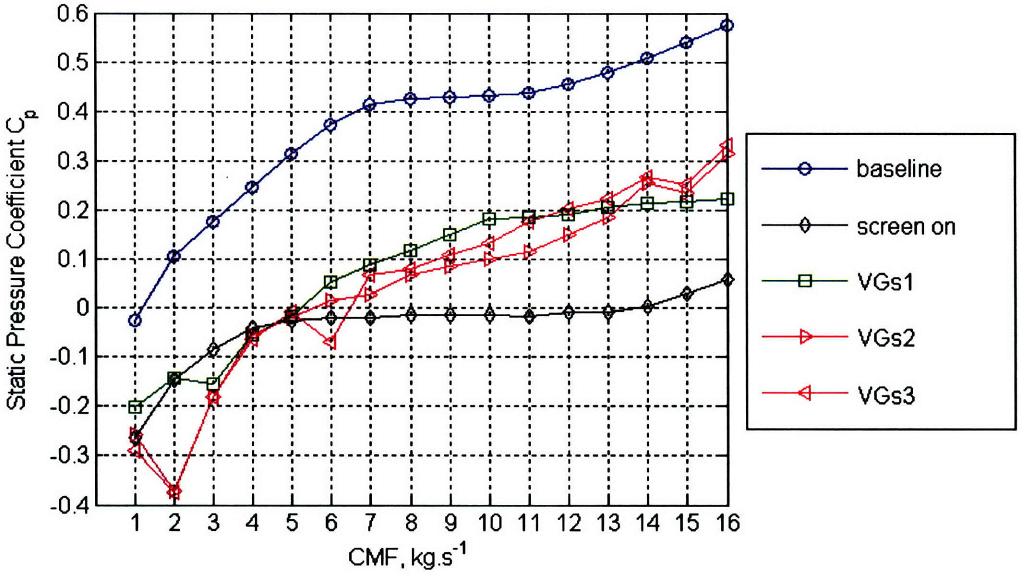

Figure 4-5: Pressure profiles at $CMF = 1.67kg.s^{-1}$ for the VG-controlled cases

The total pressure maps displayed on Fig. 4-6 also indicate a significant difference in the flow structure at the AIP. The counter-rotating configuration still features a low-total pressure area in the bottom part of the AIP, very similar to that of the "screen on" case. However, this low pressure region has reduced both in area and intensity. This is consistent with the previous observation that the counter-rotating configuration delayed the separation: the vortical structures that arise from it have consequently less time to develop before reaching the AIP, and thus have a lower impact on the AIP flow properties.

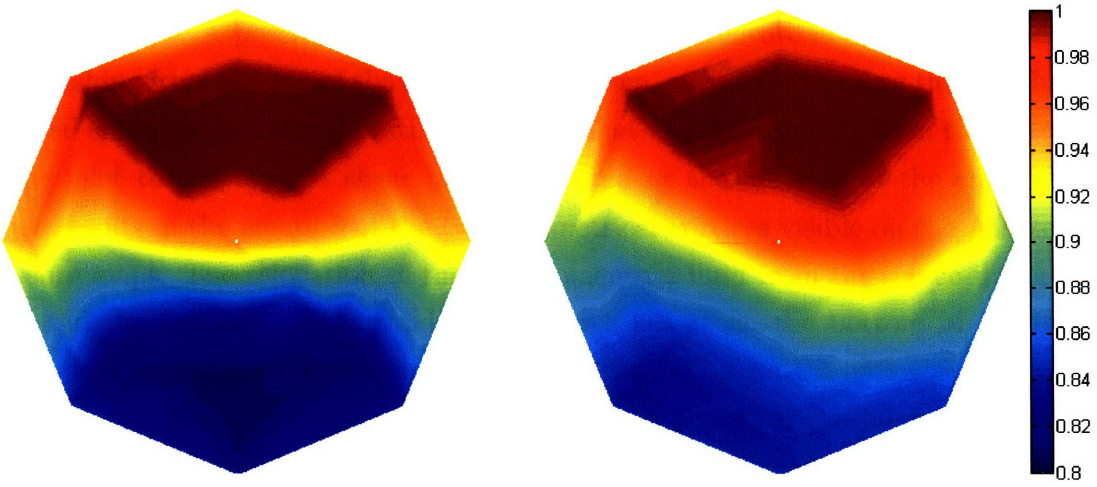

(a) "screen on" case

(b) VG1 (counter-rotating)

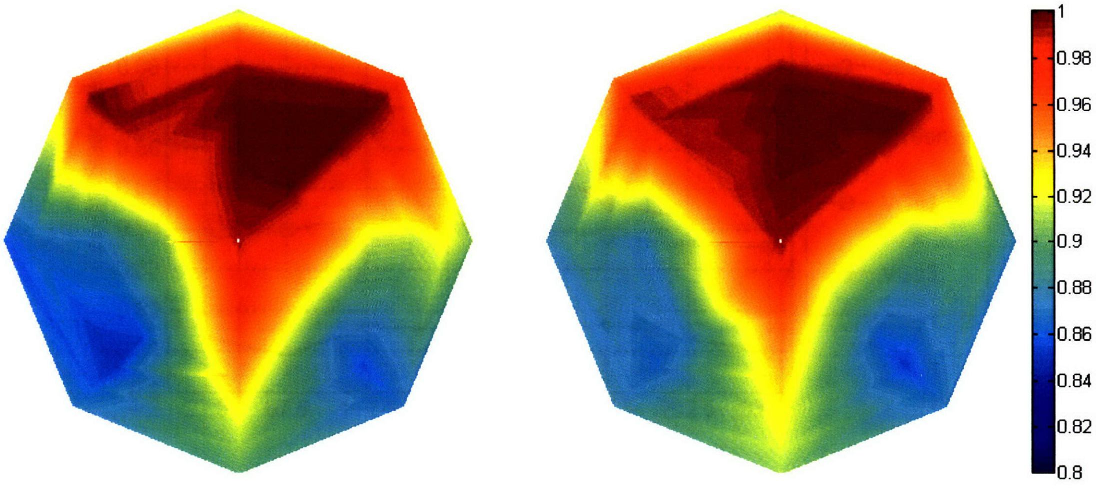

(c) VG2 (co-rotating)

(d) VG3 (co-rotating)

Figure 4-6: AIP total pressure maps for the VG-controlled cases

The co-rotating configurations exhibit a rather different flow structure. The low pressure region at the bottom of the AIP has split in two and has moved away from the centerline and a high pressure region remains at the centerline, across the entire AIP diameter. This explains the higher pressure recovery with comparison to the counter-rotating configuration. The two low pressure regions have much smaller extent and intensity than that of the "screen on" case, and they appear to be the due to vortical structures as their core, at the lowest total pressure, detaches clearly from the rest of the structure. A possible explanation for this flow structure is that the secondary flows rushing from the top of the inlet to the bottom, encounter the flow that has been diverted sideways by the co-rotating VGs and that are thus rushing from the bottom of the inlet to the top. A shear layer is created at the location of the encounter, which results in the creation of the two symmetrical vortices visible on the AIP total pressure maps. The relocation of the low-momentum fluid from the screen-distorted area and the fact that the secondary flow does not reach the bottom of the inlet apparently prevents the flow from separating. This interpretation indicates that with further optimization and addition of VGs on the top part of the inlet, even better performance could be obtained.

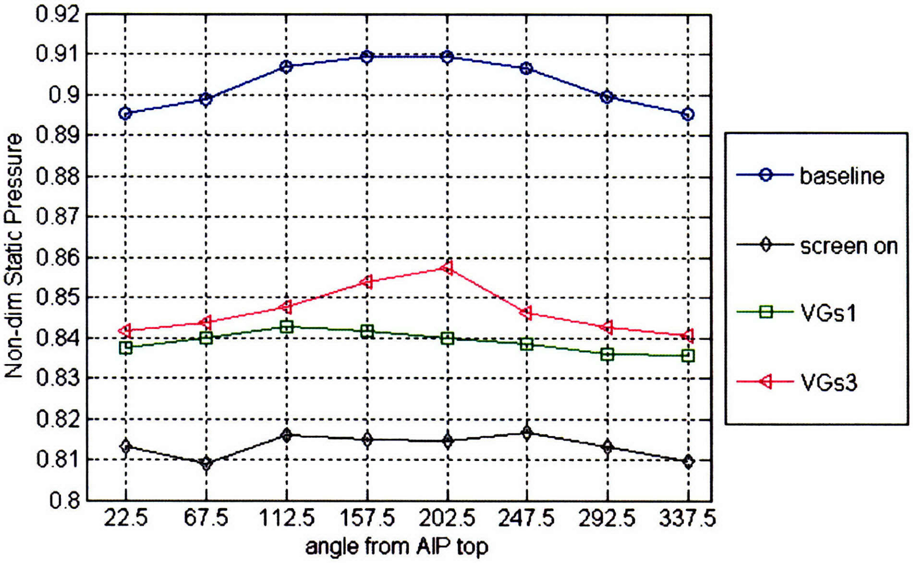

Figure 4-7: AIP circumference static pressure for the VG-controlled cases

Figure 4-7 shows the static pressure at the AIP circumference as a function of the angle from the top, at the design CMF, for four cases: (1) the baseline case, (2) the "screen on" case, and (3&4) the VG configurations 1 and 3. The second configuration results are not presented because of a failure of 4 of the scanivalve ports that were dedicated to the concerned measurements. The immediate conclusion is that, as expected, the use of VGs results in an increase in static pressure at the AIP, the largest being achieved by the third co-rotating configuration. It is interesting to note that the high total pressure region present at the centerline and at the bottom of the inlet for the VG3 configuration is also marked by a high static pressure.

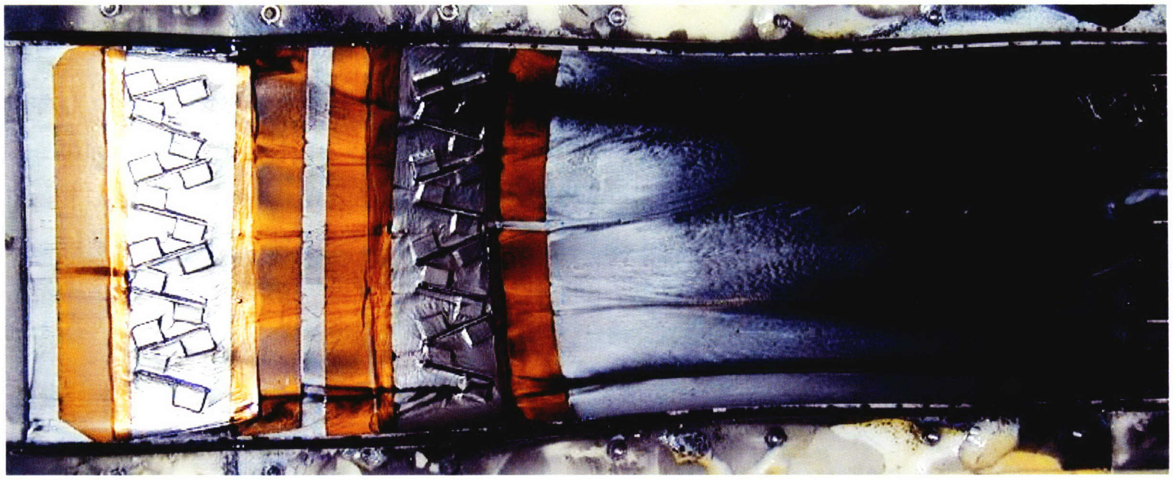

Figure 4-8: Oil flow visualization results for the VG1-controlled case

An oil flow visualization experiment was carried out on the VG1 configuration. The results (inlet lower part only) are displayed in Fig. 4-8. The flow structure is divided into several cells separated by the traces of the trailing vortices shed by the VGs. No clear reversed flow region could be pointed out on the oil flow visualization. However, there is a large pool of dye that was left downstream close of the AIP, which suggests that the flow in this region had a low velocity, and may have been reversed. The asymmetry in the flow structure, which appears to be shifting upwards on the photograph, may be the results of a slight asymmetry in the VG arrangement. It may also be caused by unsteadiness. Sometimes, also, as explained in [1], high sensitivity structures such as separated flow structures can be more stable when in an asymmetric configuration.

As a partial conclusion, the co- and counter-rotating configurations seem to have very different impact on the flow properties. The co-rotating one, which was designed to act by redirecting the secondary flows, proved more efficient than the counter-rotating one, which was designed to act mainly by mixing the low-momentum fluid from the BLI and the high momentum fluid from the freestream. This shows again the importance of the effect of secondary flows on the inlet performance, and that by managing those parasite flows, substantial performance improvements can be achieved.

4.2 Injection

The active control technique tested consisted in steady and pulsed injection. It consisted in injecting a given mass flow through a single slot positioned tangentially to the inlet wall in order to benefit from the Coanda effect. Various injectors with different slot positions and shapes, and different injection mass flow rates have been tested. This section describes in a first part the setup used to generate the necessary injection flow. The results are then discussed.

4.2.1 Injection setup

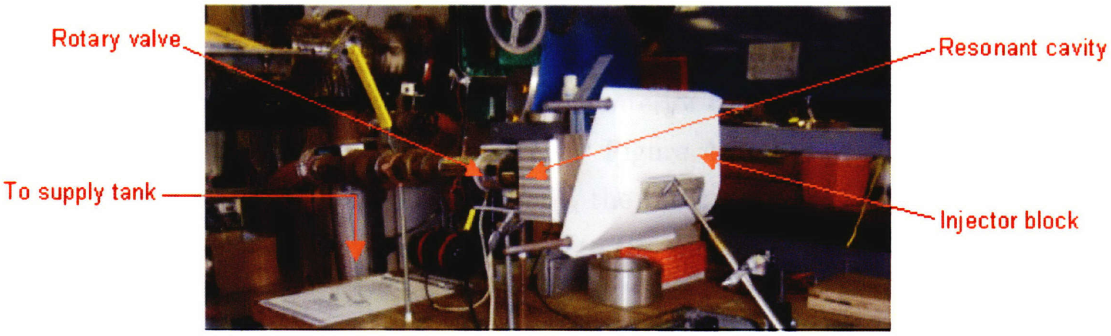

Figure 4-9: The injection setup on test bench

The injection setup made use of an independent compressed air source, namely the GTL high pressure air system. A high pressure compressor maintains large air storage tanks at a pressure of $700kPa$, which are used as a high pressure source for the injection setup. This high pressure line feeds a flow regulator that permits to set the feeding pressure to any pressure lower than the supply value. In line are then a flow-meter, a second valve used to regulate the mass flow, a third on/off valve, the rotary valve body, the resonator and the injector itself, which brings the flow up to the inlet wall. These components are connected by either rubber or copper tubing.

Figure 4-9 shows the injection setup mounted on test bench. The white plastic piece is a 2-D curved piece that was used as a substitute for the inlet wall during the injector tests.

The rotary valve produces pulsations in the flow. It consists of a bulk aluminum block (the valve body) encasing a rotor driven by an electric motor. A CAD view of the rotary valve body is shown in Fig. 4-10.

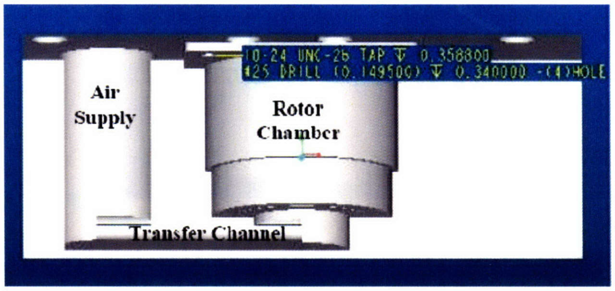
10-24 UNC-2B TAP ↧ 0.358800
#25 DRILL (0.149500) ↧ 0.340000 -(4)HOLE
Air Supply
Rotor Chamber
Transfer Channel

Figure 4-10: CAD view of the rotary valve body [51]

The copper tube feeding the rotary valve body screws into a threaded hole, which feeds internal tubing machined in the valve body, denoted as transfer channel in the sketch, which in turn connects to the center of the rotor chamber. The center of the rotor itself is empty, so that the flow fills the interior of the rotor and passes through the slots machined in the rotor side walls. Figure 4-11 shows a CAD view of the rotor. As the rotor spins in the valve body, the rotor slots align periodically to slots machined in the valve body, which connect to the exit of the valve body and feed the resonator.

The result is a forcing oscillatory pressure on the resonator cavity. By adjusting the power voltage and thus varying the DC motor frequency, the frequency of the forcing pressure can be adjusted. The resonator is just a block of aluminum with a rectangular cavity machined in it. Its dimensions were chosen in order to place the first harmonic at $1100Hz$: its length is $8.9cm$, height $0.8cm$ and width $10.15cm$. The cavity then feeds the injector block, whose role is to reduce the flow path area so that the fluid velocity is maximum at the injector exit slot, and to redirect the flow so that it is delivered tangentially to the inlet wall.

On the bench test, the system (cavity+injector) was found to resonate at a frequency of $1880Hz$, which was the frequency used in the pulsed injection control experiments. When steady flow was required, the slots of the rotor were aligned with the slot in the valve body. The axis of the motor was then locked in position so that

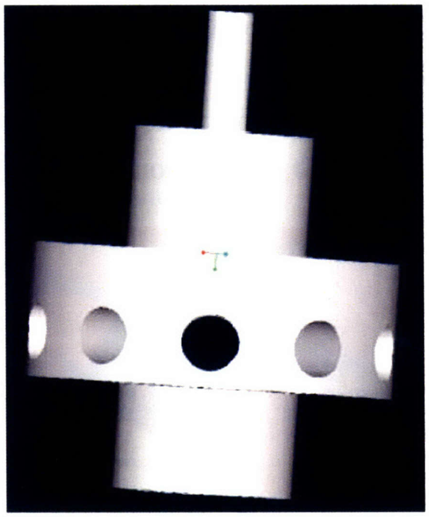

Figure 4-11: CAD view of the rotary valve rotor [51]

it would not rotate and shut the air flow off during the experiments.

4.2.2 Injector blocks

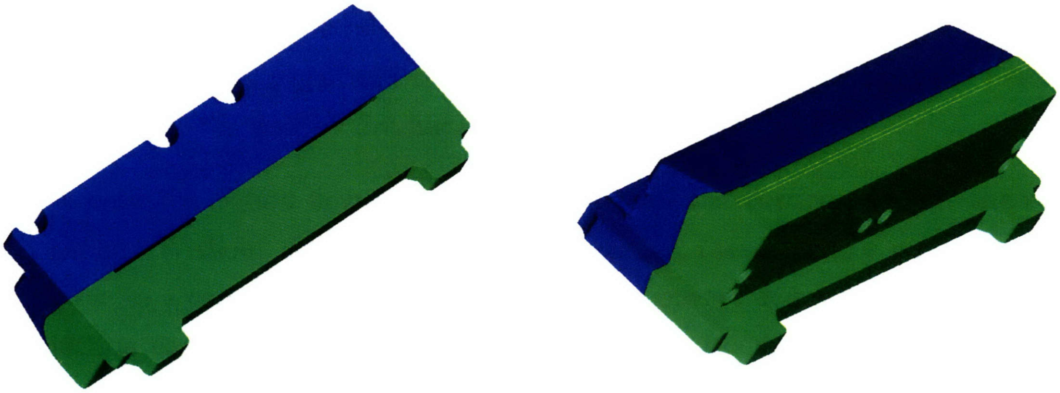

(a) bottom view

(b) top view

Figure 4-12: CAD view of an injector [41]

Three injectors have been used. A CAD view of one of the injectors is shown on Fig. 4-12. The injectors, which sit flush with the inlet inner surface, are designed to introduce flow into the inlet near the point of separation. The injectors take advantage of the Coanda effect, which states that fluid flow from a nozzle will tend to follow a nearby curved surface if the curvature of that surface is not too sharp. When inserted into the inlet, the injector block is centered at the point of flow separation. High-velocity air from the injection line is introduced through the injector block. This creates a "wall-jet" near the separation point in the inlet. Figure 4-13 shows a cross-sectional view of the injector mounted on the inlet wall.

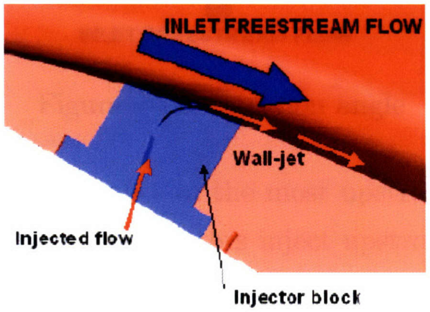

Figure 4-13: CAD cross-sectional view of the injector mounted on the inlet wall

The jet introduced by the injector can have three possible effects on the flow:

- if the injection occurs upstream of the flow separation, it can serve to energize the boundary layer and prevent the separation.
- the high-velocity flow at the injector exit creates a lower static pressure region that serves to entrain the flow from the freestream and thus can possibly "reattach" the flow by driving it towards the wall.
- A pulsed injection flow can change the size of the vortices shed at the separation. Without actuation, and as seen earlier, these vortices naturally form, grow to a certain size, and then detach and convect downstream. Periodic injection can cause these vortices to detach more frequently, meaning the shed vortices will be smaller with actuation than they would naturally be. This dynamic forcing effect has been explained by Wygnanski [52] and demonstrated by McCormick [18, 19].

The two first effects can be obtained with steady injection. The last one is particular to periodic injection.

Three injector blocks were tested in this study. From one injector to the other, three parameters were varied: the slot position upstream of the separation line, the width of the slot and the injection angle. Table 4.2 sums up the injectors geometries tested, and Fig. 4-14 illustrates the definition of injection angle.

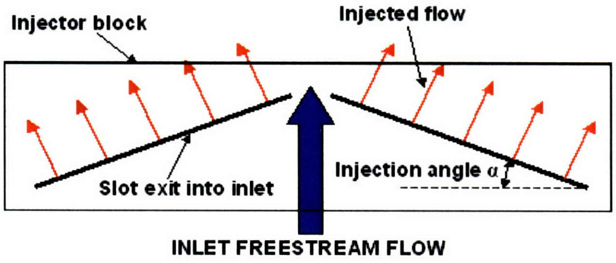

Figure 4-14: Injection angle

The position is given with respect to the most upstream point of the separation line, in the upstream direction (all injectors inject upstream of the separation line). These numbers are based on the best results of a parametric study undertaken at MIT in a previous project [34], with a different inlet, but with sensibly the same injection mass flows. All injectors were tested both in steady and pulsed injection. The injection mass flow was set from 0% to 2.5% of the inlet mass flow, as 2% was chosen as the upper limit.

Table 4.2: The injectors tested

	Position	Slot width	Injection angle
Injector# 1	$5.1mm$	$0.381mm$	0^o
Injector# 2	$7.6mm$	$0.254mm$	0^o
Injector# 3	$2.5mm$	$0.254mm$	12^o

These injectors were designed and fabricated in SLA as part of a previous project at MIT, which included a parametric study of the injectors [34]. Eight injectors were consequentially available for this project, and the 3 most representative and efficient injectors out of the 8 originally fabricated were used in this current project. The injectors also had to be adapted to the MBDA inlet wall. The inlet wall surface of these injectors has a 2-D profile (surface curved along a single direction), meaning it is not curved in the spanwise direction. This was consistent with the previous experiment, but in the current experiment the inlet wall is actually slightly curved in the spanwise direction as well (surface curved along two main directions). This was easily corrected using automotive body filler ("body putty"). Automotive body filler is a very malleable chemical product that can be given any shape, which hardens and sticks strongly when dried. It was used to fill the gap between the surface of the injectors and the inlet wall. A latex mold of the inlet wall was created before cutting the slot for the injector, and was used to ensure the automotive filler had the exact shape of the inlet wall. As the dry automotive filler comes out somewhat rough, it had to be sanded using fine sand paper.

A major concern was that the injectors would choke, as the mass flows used in this study are slightly higher than the mass flows for which these injectors were originally designed. But experiments carried out on the test bench and during the inlet runs showed that although the injectors were indeed close to choking, choking actually only occurred for injection mass flows of about 2.5% to 4% of the inlet mass flow, depending on the feeding total pressure, which is above the 2% acceptable upper limit set in this project. Actually, this was considered to be an advantage as the flow at the exit of the injector flow would be closer to Mach 1 if the injector was close to choking, thus producing higher exit momentum.

4.2.3 Injection setup mass flow measurement

The injection mass flow rate is measured by an ABB [37] 10A4500 variable area flow meter, tube number FP-2-27-G-10, float number 2-GSVGT-98A, mounted downstream of the regulator. It is shown on Fig. 4-15.

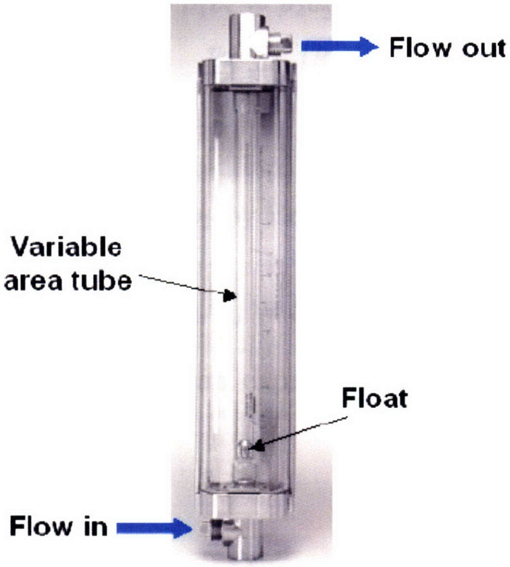

Figure 4-15: The variable area flowmeter

It consists of a vertical tube of increasing area (from bottom to top) encasing a metallic, cone-shaped float. Because the tube area increases, the fluid velocity decreases, and so does the drag exerted on the float. The fluid flowing from the bottom to the top pushes the float up, until it reaches a position where the drag exactly compensates its weight. Along the tube are gradations in percentage of the maximum mass flow. The maximum flow rate for air at standard source conditions ($P_T = 70Psi$ and $T_T = 70F$) is given by the manufacturer [38] as $scfm_{Air\ eq.} = 99.0feet^3.min^{-1}$. When using the flowmeter with a fluid at different conditions, the reading in percentage of the maximum mass flow at standard conditions has to be converted to physical mass flow. Let S_f be the cross-sectional area of the float, v_1 the velocity of the fluid at one particular height in the tube and ρ_1 its density, then the drag D_f it exerts on the float is expressed by Eq. 4.1:

$$D_f = C_{D_f} S_f \frac{1}{2} \rho_1 v_1^2 \tag{4.1}$$

where C_{D_f} is the drag coefficient of the float. In order to push the float at the same height in the tube, that is in order to exert the same drag, air at standard source conditions would need to have a velocity v_2 and its density would be ρ_2. The equality of drag leads to Eq. 4.2:

$$\begin{aligned} \rho_1 v_1^2 &= \rho_2 v_2^2 \\ \frac{v_2}{v_1} &= \sqrt{\frac{\rho_1}{\rho_2}} \end{aligned} \tag{4.2}$$

The gradation reading gives the standard air equivalent mass flow $\dot{m}_{Air\ eq.}$, which can be expressed in terms of ρ_2 and v_2 by Eq. 4.3:

$$\dot{m}_{Air\ eq.} = S_f \rho_2 v_2 \tag{4.3}$$

Combining Eq. 4.3 with Eq. 4.2 an expression for the actual mass flow can be derived and is given by Eq. 4.4:

$$\dot{m}_{actual} = S_f \rho_1 v_1 = S_f \frac{\rho_2 v_2^2}{v_1} = \dot{m}_{Air\ eq.} \frac{v_2}{v_1} = \dot{m}_{Air\ eq.} \sqrt{\frac{\rho_1}{\rho_2}} = \dot{m}_{Air\ eq.} \sqrt{\frac{P_{T_1} T_{T_2}}{P_{T_2} T_{T_1}}} \tag{4.4}$$

where P_{T_1} and T_{T_1} are the actual operating total pressure and temperature. With the manufacturer's units, this becomes:

$$\dot{m}_{actual} = \dot{m}_{Air\ eq.}\frac{1}{13.34}\sqrt{\frac{P_{T_1}530}{14.7T_{T_1}}} \tag{4.5}$$

where $\dot{m}_{actual}$ is expressed in $lb.min^{-1}$, P_{T_1} in Psi and T_{T_1} in ^oR (Rankine), which is the conversion formula provided by the manufacturer [39].

4.2.4 Steady injection results

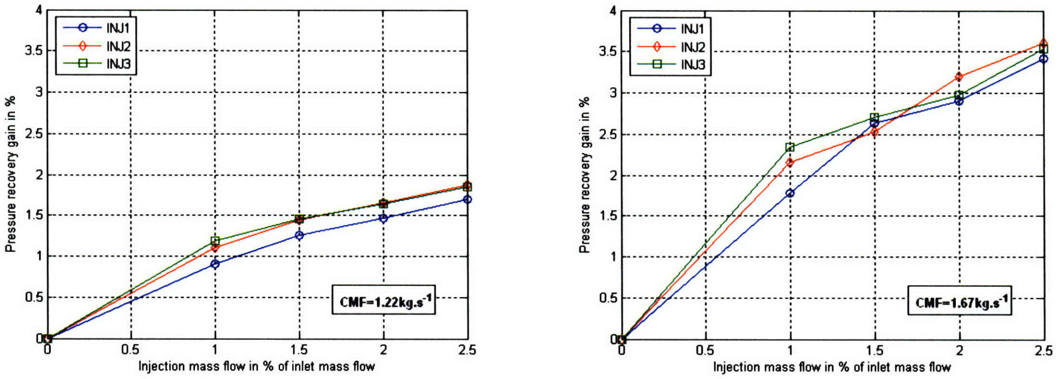

(a) $CMF = 1.22kg.s^{-1}$

(b) $CMF = 1.67kg.s^{-1}$

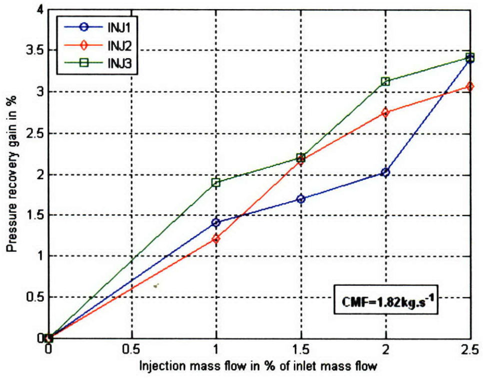

(c) $CMF = 1.82kg.s^{-1}$

Figure 4-16: Pressure recovery as a function of steady injection mass flow

Figure 4-16 shows the pressure recovery gain in percentage, $\%\Delta PR$, as a function of the injected mass flow, for operating points of $CMF = 1.22kg.s^{-1}$, $CMF = 1.67kg.s^{-1}$ and $CMF = 1.82kg.s^{-1}$. The gain in pressure recovery ΔPR is nondimensionalized by the free stream total pressure P_{T0}, so that it is simply given by Eq. 4.6:

$$\%\Delta PR = \frac{\Delta PR}{P_{T0}} = PR_{controlled} - PR_{screen\ on} \tag{4.6}$$

It is therefore necessary to recall that the higher the mass flow, the smaller the non-controlled case pressure recovery. At $CMF = 1.22 kg.s^{-1}$, $CMF = 1.67 kg.s^{-1}$ and $CMF = 1.82 kg.s^{-1}$, the "screen on" case pressure recoveries were respectively 96.6%, 91.4% and 86.2%.

The first result drawn from Fig. 4-16 is that steady injection does improve pressure recovery, whatever the inlet mass flow, injection mass flow or injectors. The absolute gain in pressure recovery is best at the design operating point $CMF = 1.67 kg.s^{-1}$.

It is interesting to note that the injector 3, which injects at a 12^o angle with respect to the streamwise direction, leads to the highest pressure recovery for almost all conditions. This is true for all inlet mass flows, and in particular at $CMF = 1.67 kg.s^{-1}$ for which, at a 1% injection mass flow, the pressure recovery gain is 2.3%, from 91.4% 93.7%. Injector 3 is slightly less effective than injector 2 at the highest injection mass flows, at the inlet condition $CMF = 1.67 kg.s^{-1}$. As it is believed that injecting at an angle has a stronger impact on the secondary flows, this result supports the hypothesis previously stated that secondary flows are the primary cause of distortion. Injector 1 leads to the poorest overall results. This perhaps could have been expected, as it features the largest slot width, and therefore injects flow at a lower velocity for the same injection mass flow than the other injectors. This is in accordance with the literature, where the importance of injection momentum, commonly described in terms of momentum coefficient C_μ, is discussed in several references [20, 21, 22, 24].

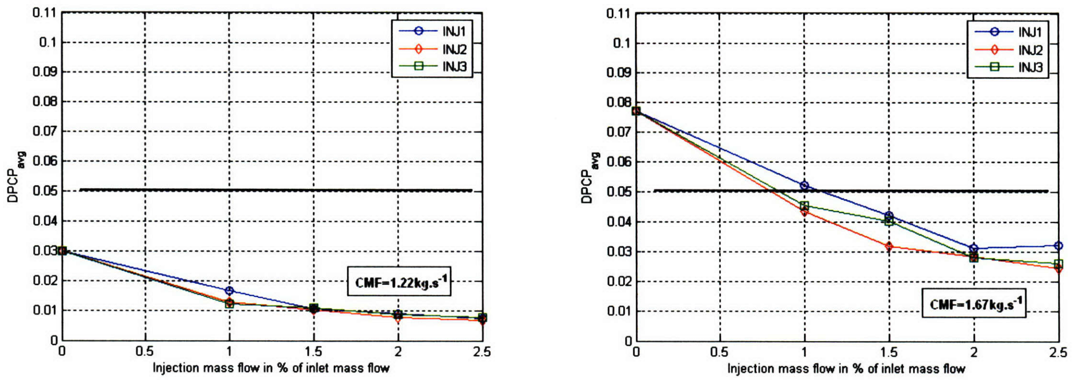

(a) $CMF = 1.22kg.s^{-1}$

(b) $CMF = 1.67kg.s^{-1}$

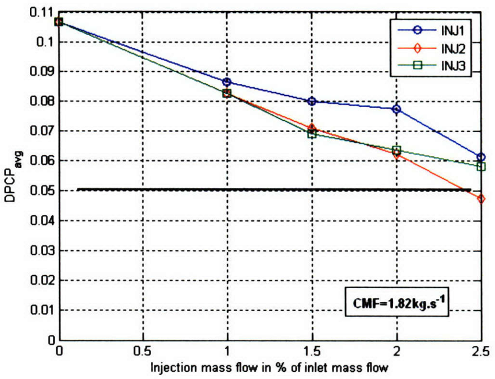

(c) $CMF = 1.82kg.s^{-1}$

Figure 4-17: Circumferential distortion as a function of steady injection mass flow

Figure 4-17 shows the circumferential distortion, expressed in terms of $DPCP_{avg}$ as a function of the injected mass flow. As can be seen, steady injection does reduce the distortion. For the inlet mass flow $CMF = 1.22kg.s^{-1}$, the distortion level, which is already acceptable without injection, becomes comparable to that of the baseline case for the lowest injection mass flows. For $CMF = 1.67kg.s^{-1}$, the result is a nice decrease of the distortion from $DPCP_{avg} = 0.077$, above the 0.05 limit, to $DPCP_{avg} = 0.045$, below the 0.05 limit, and that for injection mass flows as low as 1%. For $CMF = 1.82kg.s^{-1}$, the result is also a significant decrease of the distortion level. However, it gets below the 0.05 limit only for an injection mass flow of 2.5% and only for the injector 2. Injector 3 clearly appears as the most efficient injector, as it realizes the best reduction in distortion level for all inlet mass flows.

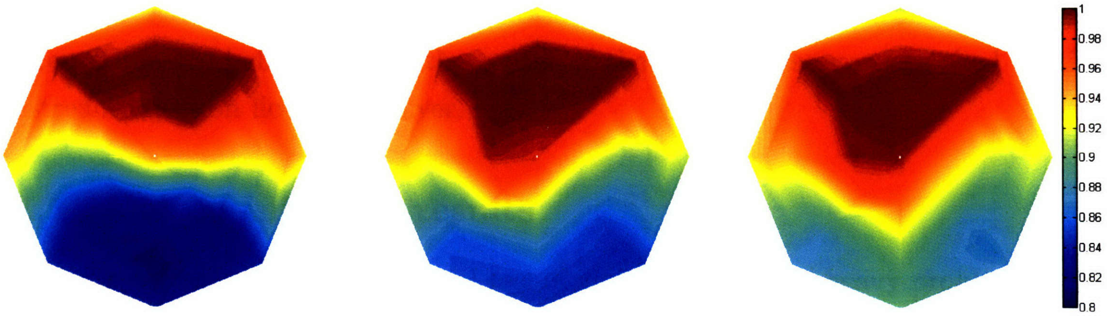

(a) INJ1: no injection (b) INJ1: 1% injection (c) INJ1: 2% injection

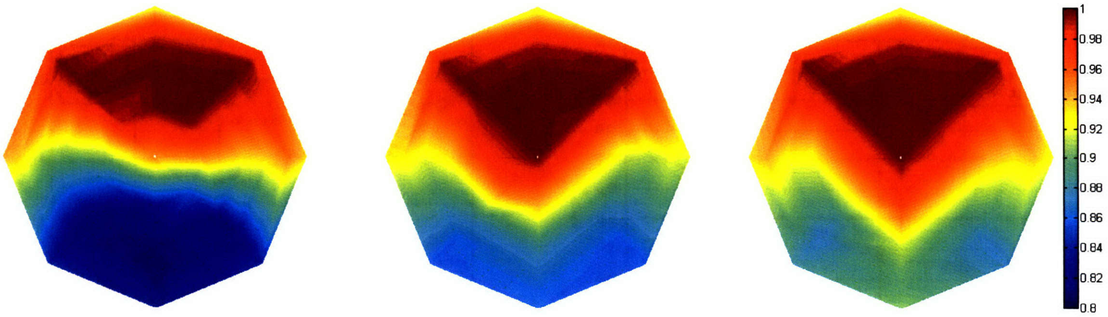

(d) INJ2: no injection (e) INJ2: 1% injection (f) INJ2: 2% injection

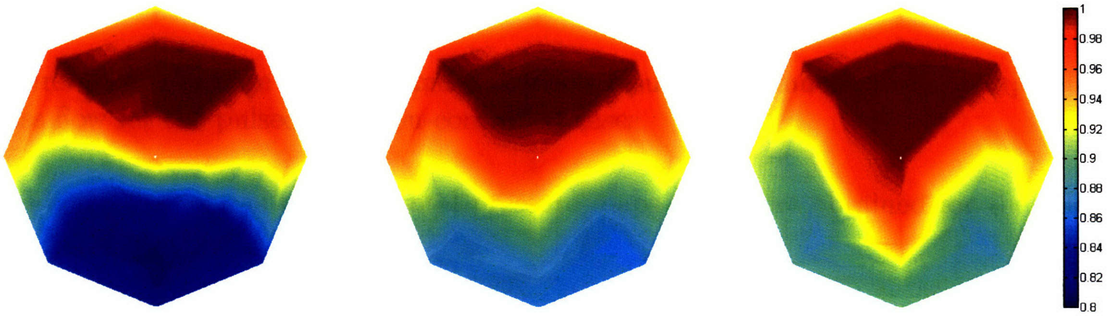

(g) INJ3: no injection (h) INJ3: 1% injection (i) INJ3: 2% injection

Figure 4-18: AIP total pressure maps at $CMF = 1.67kg.s^{-1}$ for the steady injection-controlled cases

Figure 4-18 shows the total pressure maps obtained at the design operating point $CMF = 1.67kg.s^{-1}$ with various steady injection mass flows, for injector 3 and 2. The effect of the steady injection on the extent and intensity of the low total pressure area at the AIP is quite clear. The two low-total pressure region on each side of the centerline are believed to be the center of the stream wise vortices shed by the freestream-injection flow shear layer.

4.2.5 Pulsed injection results

Periodic injection was the last control technique tested. Due to heavy problems with the motor, the runs had to be shortened to the essential, and periodic injection was run only for the inlet mass flow $CMF = 1.67kg.s^{-1}$. The pressure recovery and distortion results are shown on Fig. 4-19.

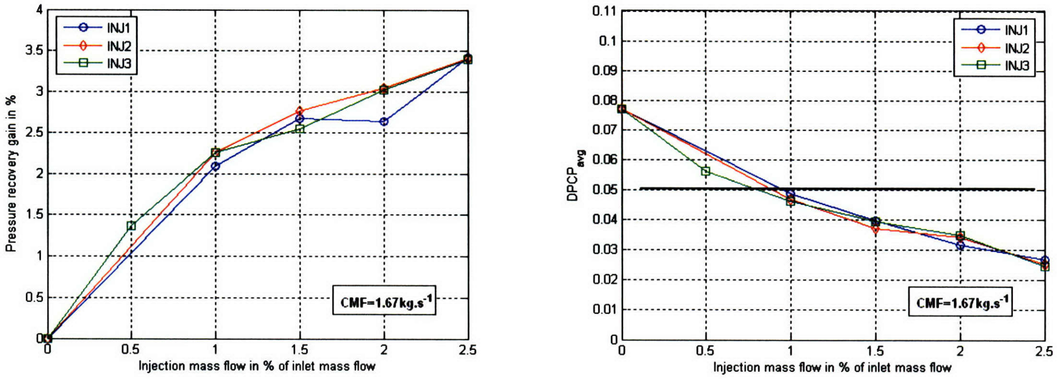

(a) Pressure recovery

(b) $DPCP_{avg}$

Figure 4-19: Pressure recovery and distortion results as a function of the injection mass flow for the pulsed injection-controlled cases

Figure 4-20 shows the AIP total pressure maps that were obtained for the inlet mass flow of $CMF = 1.67kg.s^{-1}$.

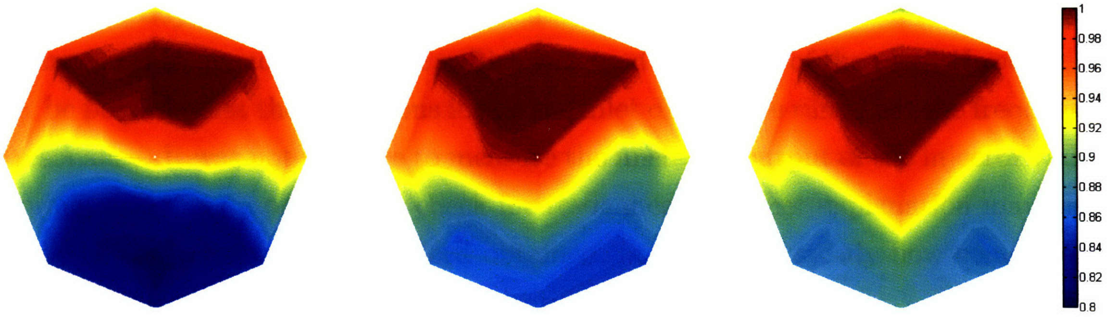

(a) INJ1: no injection (b) INJ1: 1% injection (c) INJ1: 2% injection

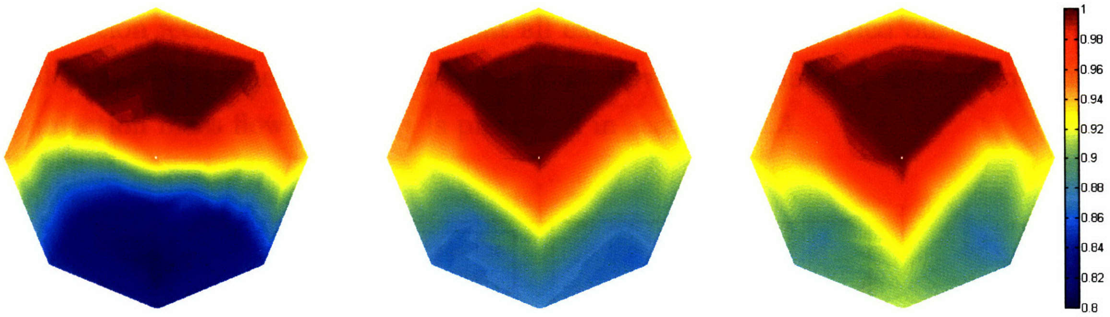

(d) INJ2: no injection (e) INJ2: 1% injection (f) INJ2: 2% injection

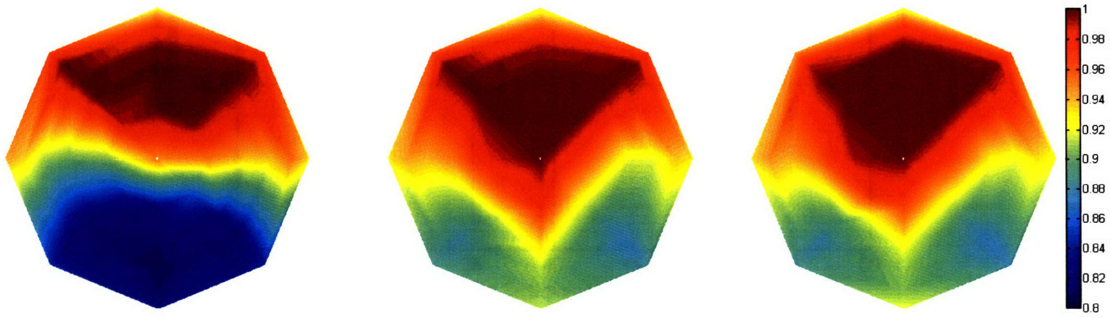

(g) INJ3: no injection (h) INJ3: 1% injection (i) INJ3: 2% injection

Figure 4-20: AIP total pressure maps at $CMF = 1.67kg.s^{-1}$ for the pulsed injection-controlled cases

Unfortunately, the periodic injection results show very little difference from the steady injection results. The output of the pulsating injector remains an unknown in the conditions of the runs. The injection flow was characterized on the test bench, by taking unsteady total pressure measurements. It was clearly shown that resonance was obtained at a frequency of $1880 Hz$, which was used during all of the runs. However, it may be possible that the conditions inside the inlet during the run affect the frequency of resonance. It was not possible to measure the unsteady output of the injector while running, and thus impossible to check for resonance. Another explanation may also simply be that resonance was indeed obtained, but that the steady flow component was sufficient and overshadowed the pulsation beneficial impact.

The goal of pulsed injection is to reduce the injection mass flow, while maintaining the same improvement than steady flow injection. In this setup, it was simply impossible to measure injection mass flows lower than 1% for most of the inlet mass flow, at the injection feeding total pressure that all experiments were carried out with. This problem is a consequence of the way the mass flow meter that was used to measure the injection mass flow works. It is presented in section 4.2.3.

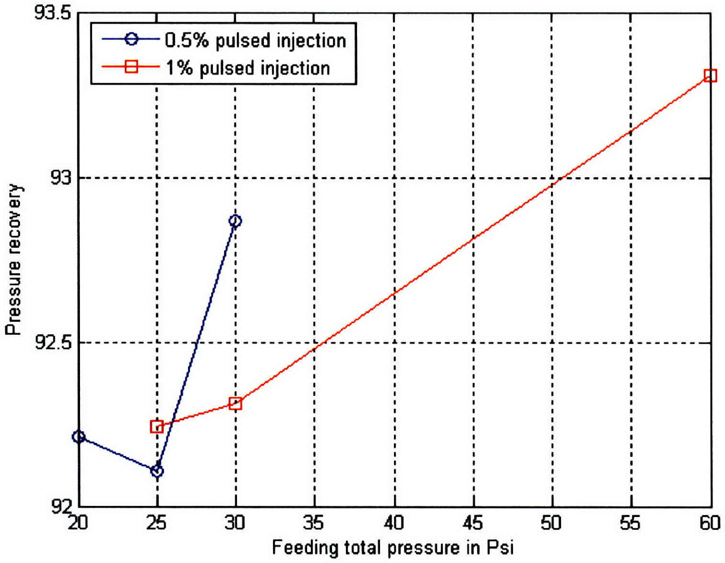

Figure 4-21: Pressure recovery as a function of the injection feeding total pressure

In order to correct for that, the solution experimented was to lower the injection feeding total pressure, in order to enable the measurements of lower injection mass flows. However, it was also expected that by lowering the feeding total pressure, the mass flow capacity of the injector would decrease, and the injector would choke at a lower physical mass flow, making the obtention of larger mass flows impossible. Pulsed injection runs were therefore conducted at injection feeding total pressure of

$138kPa$, $172kPa$, $207kPa$ and $414kPa$, respectively $20Psi$, $35Psi$, $30Psi$ and $60Psi$ the latter being the pressure at which all runs were conducted. The results are shown in Fig. 4-21. As expected, with feeding total pressure lower than $30Psi$, it was not possible to obtain injection mass flows larger than 0.5%, so not direct comparison with the previous pulsed injection results is possible. Moreover, the trend in the results is clearly an increase of the pressure recovery with increasing feeding total pressure.

Clearly, these series of experiments are in need for more unsteady characterization of the pulsating injection, and more thoroughly assessment of whether the flow is or is not pulsating. A better knowledge of the losses in the injection setup would also have greatly helped.

4.3 Control techniques comparisons

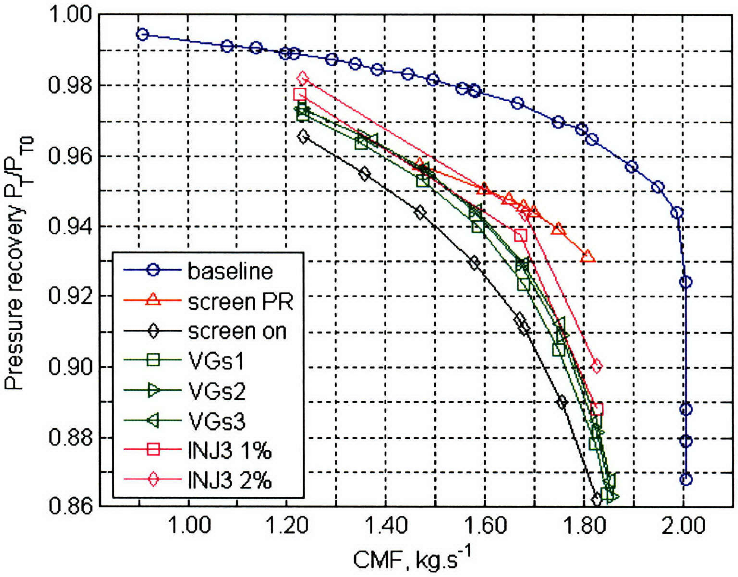

Figure 4-22: Pressure recovery as a function of inlet mass flow for the VG- and injection-controlled cases

Figure 4-22 shows the pressure recovery for the 3 VG configurations tested and the best injector (INJ3) with injection mass flow of 1% and 2%. All of the control techniques tested lead to some improvement of the pressure recovery. At $CMF = 1.67kg.s^{-1}$, the pressure recovery gain with the VGs is 1.82% with the best co-rotating configuration, to be compared with the 2.6% and 3.2% achieved with the 1% and 2%

injection mass flow (injector 3).

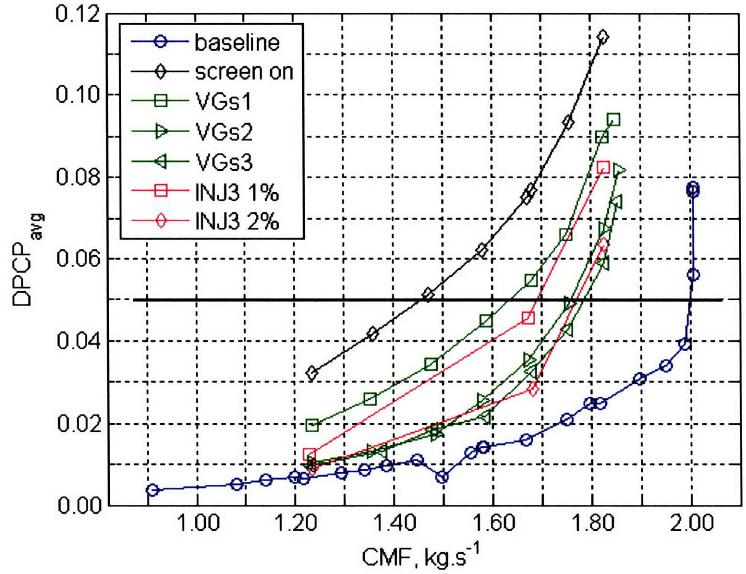

Figure 4-23: Circumferential distortion as a function of inlet mass flow for the VG- and injection-controlled cases

The distortion level is also reduced by all of the control techniques tested, as shown on Fig. 4-23. The gain achieved by the 1% mass flow injection is comparable to the worst VG configuration, and the 2% mass flow injection is comparable to the best one.

Chapter 5

Conclusions

In response to industrial needs for a comparative evaluation of flow control techniques as a way to maintain inlet efficiency at off-design conditions, an experimental setup has been developed for testing flow control techniques on a thick boundary layer ingesting transonic inlet, at flow conditions representative of typical transonic ($M = 0.6$) cruise missile flight conditions. Using this setup, a baseline has been characterized, a distortion device has been designed and added to simulate forebody layer ingestion and two flow control techniques, based on Vortex Generators and injection upstream of the separation line, were then implemented in an attempt to improve the deteriorated flow properties at the AIP. They were evaluated in terms of pressure recovery gain and distortion reduction at the AIP. Oil flow visualizations was used to reveal key features of the flow structure.

The designed inlet geometry, presented in chapter 2 and characterized in chapter 3 exhibited good performance, with high pressure recovery, 97.5%, and low circumferential distortion level $DPCP_{avg} = 0.0160$. Oil flow visualizations revealed that the flow separated on the suction side of the inlet in a closed structure characterized as "owl face of the second kind", and that strong secondary flows rushed from the top to the suction side, interacting with the separated flow.

The distortion device used to simulate forebody boundary layer ingestion consisted in a screen of selected solidity, and produced a total pressure loss of 15% on 20% of the inlet height. The inlet was shown to greatly amplifies the loss introduced by the screen: the pressure recovery lowered to 91.1%, the distortion level increased to $DPCP_{avg} = 0.0769$. The flow structure was profoundly affected: the separation line moved upstream, and grew in size over $^{3}/_{4}$ of the inlet length. The low total pressure area concentrated in the lower part of the AIP, where the vortices shed at the separation impact and where low momentum fluid brought by the secondary flows accumulated.

The VGs in use were rectangular, low-profile VGs, scaled to the boundary layer ingested by the inlet. They were used in two configurations:

- a counter-rotating configuration, designed to enhanced mixing the low momentum fluid from the boundary layer with the high momentum fluid from the freestream,
- and a co-rotating configuration, designed to redistribute the low momentum fluid accumulated on the suction side of the inlet by the secondary flows.

Both configurations proved efficient at reducing distortion and improving pressure recovery. The co-rotating configuration was proved the most efficient, with a pressure recovery gain of 1.82% and a distortion level of $DPCP_{avg} = 0.0326$. The results suggested that if separation was only delayed with the counter-rotating configuration, it was suppressed in the co-rotating one, highlighting the importance of the secondary flows as a source of distortion.

Steady injection upstream of the separation line was then tested. Three Coanda-type injectors were used, in order to study the influence of slot width and injection flow angle. Decreasing the slot width increases the injected flow velocity, injecting at an angle is supposed to increase the interaction of the injected flow with the secondary flows, and redistribute the low-momentum fluid accumulated on the suction side of the inlet. The results obtained with steady injection indicate that a larger injection velocity is beneficial, which is thought to be due to the lower pressure associated with a higher injection velocity, that keeps the flow attached to the wall. Injecting with an angle proved more efficient, confirming once again the secondary flows as a primary source of distortion. At 1% and 2% injection mass flow, the best injector led to a pressure recovery gain of respectively 2.6% and 3.3%, and reduced the distortion level to respectively $DPCP_{avg} = 0.0455$ and $DPCP_{avg} = 0.0282$. Overall, the pressure recovery gain increased, and the distortion level significantly decreased with increasing injection mass flow. Oil flow visualization results suggested that injection suppressed the separation, the remaining distortion being due to the vortex generation in the shear layer between the injected flow and the freestream.

Pulsed injection was finally implemented. The same injectors and the same range of injection mass flow than the steady injection study were tested. Flow was excited at a frequency of $1880Hz$. Unfortunately, pulsed injection did not improve the results obtained with steady injection. A more in-depth characterization of the injection flow and a deeper parametric study, which were not possible in this project, would have been required.

Based on the experimental results of this study, the main characteristics of the flow in this transonic S-duct have been described. This investigation experimentally proved that VGs and steady injection could improve the pressure recovery and reduce the distortion at the AIP, and quantified the potential benefits. Insights on the way these effectors act on the inlet flow and their specifications (dimensions, disposition, injection mass flow) have been provided. Items that would be of interest for further work include:

- An in-depth characterization of the pulsed injection flow. The injection flow was characterized in terms of exit total pressure on the test bench at atmospheric pressure, and resonance was obtained at the actuation frequency, but further investigation is required to fully characterize the injected flow in terms of injection velocity and momentum coefficient C_μ in the tests conditions. A systematic analysis of the losses in the injection setup would also greatly help improve the setup.
- More generally, a deeper parametric study of the flow control effectors. The purpose of this study was to compare flow control techniques implemented based on previous studies and the literature, not to fully optimize them to this inlet geometry. However, it is believed that better results can be obtained with a systematic study of the influence of the flow control effectors parameters, such as the VGs geometry, their disposition, the injector geometry, and the injection flow properties.

Bibliography

[1] Délery J., "Topologie des écoulements tridimensionnels stationnaires: points singuliers, séparatrices et structures tourbillonaires", ONERA technical report# RT 1217078 DAFEN.

[2] Perry, A. E. and Chong, M. S., "A series expansion study of the Navier-Stokes equations with applications to three-dimensional separation patterns", *Journal of fluid mechanics*, vol. 173, 1986, pp. 207-223.

[3] Greitzer, E. M. and Longley, J. P., "Inlet Distortion Effects in Aircraft Propulsion System Integration", AGARD lecture, 1992.

[4] Wellborn S. R., Reichert B. A., Okiishi T. H., "An Experimental Investigation of the Flow in a Diffusing S-Duct", AIAA 1992-3622.

[5] Harloff, G. J., Reichert B. A., Wellborn S. R., "Navier-Stokes Analysis and Experimental Data Comparision of Compressible Flow in a Diffusing S-Duct", AIAA 1992-2699.

[6] Vakili, A., Wu, J. M., Liver P. and Bhat M. K., "Measurements of Compressible Secondary Flow in a Circular S-Duct", AIAA 83-1739.

[7] Vakili, A., Wu, J. M., "Comparison of Experimental and Computational Compressible Flow in a S-Duct", AIAA $22^n d$ Aerospace Sciences meeting, 9-12 January 1984.

[8] Bradshaw, P., Bandsod, P., "The flow in S-Shaped Duct", Aeronautical Quaterly, May 1972.

[9] Tindell, R. H., "Highly Compact Inlet Diffuser Technology", AIAA 87-1747.

[10] Brear, M. J., Warfield, Z., Magnus, J. F., Cpt. Braddom, S., Paduano, J. D., Philhower, J. S., "Flow separation within the engine inlet of an uninhabited combat air vehicle", FEDSM2003-45579.

[11] Klausmeyer, S. M., Papadakis, M., Lin, J. C., "A Flow Physics Study of Vortex Generators on a Multi-Element Airfoil", AIAA 96-0548.

[12] Allan, B. G., Yao, C.-S., Lin, J. C., "Numerical Simulations of Vortex Generator Vanes and Jets on a Flat Plate", AIAA 2002-3160.

[13] May, N. E., "A New Vortex Generator Model for Use in Complex Configuration CFD Solvers", AIAA 2001-2434.

[14] Wendt, B. J., "Initial Peak Vorticity Behavior for Vortices Shed from Airfoil Vortex Generators", AIAA 97-?.

[15] Panitz, T. and Wasan, D. T., "Flow Attachment to Solid Surfaces: The Coanda Effect", *American Institute for Chemical Engineers*, Vol. 18, No. 1, January 1972, pp. 51.

[16] Lee, C. Y. and Goldstein, D. B., "Two-dimensionnal Synthetic Jet simulation", *AIAA Journal*, Vol. 40, No. 3, March 2002.

[17] McCormick, D. C., "Two-dimensionnal Synthetic Jet simulation", AIAA 2000-0519.

[18] McCormick, D. C., "Boundary layer separation control with directed synthetic jets", AIAA-2000-519.

[19] Lorber, P. F., McCormick, D. C., Anderson, T. J., Wake, B. E., MacMartin, D. G., Corke, T. C., "Rotorcraft retreating blade stall control", AIAA-2000-2475.

[20] Amitay, M., Barton, L., and Glezer, A., "Aerodynamic Flow Control Using Synthetic Jet Technology", AIAA 98-0208.

[21] Smith, D. R., Amitay, M., Kibens, V., Parekh, D., Glezer, A., "Modification of Lifting Body Aerodynamicas Using Synthetic Jet Actuators", AIAA 98-0209.

[22] Müller, M. O. et al. and Parviz, B. A. et al., "Thrust Performance of Micromachined Synthetic Jets", AIAA 200-2404.

[23] Grosjean, C., Lee, G., Hong, W., Tai, Y. C. and Ho, C. M., "Micro-Balloon Actuators for Aerodynamic Control", *Proceedings, 1998 IEEE Micro Electro Mechanical Systems Workshop (MEMS' 98, Heidelberg, Germany)*, 1998.

[24] Chen, F.-J., Yao, C., Beeler, G. B., Bryant, R. G. and Fox, R. L., "Development of Synthetic Jet Actuators for Active Flow Control at NASA Langley", AIAA 200-2405.

[25] Washburn, A. E., "NASA Micro-Aero-Adaptive Control", *Proceedings of SPIE*, Vol. 4332, 2001.

[26] Grossman, K. R., Cybyk, B. Z. and VanWie, D. M., "Sparkjet Actuators for Flow Control", AIAA 2003-57.

[27] Tsao, T., Liu, C., Tai, Y.-C., "Micromachined Magnetic Actuators for Active Fluid Control", AFOSR University Research Initiative and Advanced Research Projects Agency project report, (*no further reference*).

[28] Hamstra, J. W., Miller, D. N., Truax, P. P., Anderson, B. A. and Wendt, B., J., "Active Inlet Flow Control Technology Demonstration", *The Aeronautical Journal*, Oct. 2000, pp. 473.

[29] Anderson B. H. and Gibb, J., "Vortex generator installation studies on steady state and dynamic distortion", *Journal of Aircraft*, Vol. 35, No. 4, July-August 1998.

[30] Gibb J. and Anderson B. H., "Vortex Flow Control Applied to Aircraft intake ducts", AIAA 95-40104.

[31] Anderson B. H. and Gibb J., "Study on Vortex Generator Flow Control for the Management of Inlet Distortion", *Journal of Propulsion an Power*, Vol. 9, No. 3, May-June 1993.

[32] Warfield, Z., "Active Control of Separation Induced Distortion in a Scaled Tactical Aircraft Inlet", M.S. thesis, Aeronautics and Astronautics Dept., Massachusetts Institute of Technology, Cambridge, MA, Sept. 2001.

[33] Tournier, S., "Design d'une entree d'air subsonique en S par CAO parametrique", *notes de service MBDA*, August 2003.

[34] Luers, A. S., "Flow control techniques in a serpentine inlet: an enabling technology to increase the military viability of unmanned air vehicles", M.S. thesis, Aeronautics and Astronautics Dept., Massachusetts Institute of Technology, Cambridge, MA, June 2003.

[35] Anabtawi, A. J., Blackwelder R. F., Lissaman, P. B. S., Liebeck, R. H., "An Experimental Study of the Effect of Offset on Thick Boundary Layers Flowing Inside Diffusing Ducts", AIAA 99-3590.

[36] Anabtawi, A. J., Blackwelder R. F., Lissaman, P. B. S., Liebeck, R. H., "An Experimental Investigation of Boundary Layer Ingestion in a Diffusing S-Duct With and Without Passive Flow Control", AIAA 99-0739.

[37] *ABB website*
[http://www.abb.com/] .

[38] Anon., "Instruction manual 10A4500/4600 V/A Master Flowmeter", capacity table.

[39] Anon., "ABB Data Sheet D-FV-10A4500_1", gas conversion.

[40] Berrier, B. L. and Morehouse, M. B., "Evaluation of Flush-Mounted S-Duct Inlets with Large Amounts of Boundary Layer Ingestion".

[41] Paduano, J. D., *personal communication.*

[42] Anon., "Aerospace recommended practice", SAE ARP1420 Rev. B.

[43] Beale, D.K., Hand, T. L., and Sebourn, C. L., "Development of a Bellmouth Airflow Measurement Technique for Turbine Engine Ground Test Facilities", AIAA 2001-3676.

[44] *Rapid Prototyping: SLA*
[http://www.efunda.com/processes/rapid_prototyping/sla.cfm] .

[45] Anon., "Practical guide to the evaluation of the metering performance of differential producers", 2/76 Supersedes MS-36, Ref. 180.21-5

[46] Anon., "Metering Performance Investigation and Substantiation of the "Universal Venturi Tube" (UVT)", 3/77 Supersedes 11/73, Ref. 180.21-4

[47] *Bifwater website*
[http://www.bifwater.com] .

[48] Beale, D. K., Cramer, K. B. and Dr. King, P. S., "Development of improved methods for simulating aircraft inlet distortion in turbine engine ground tests", AIAA 2002-3045.

[49] Bruce, E. P., "Design and evaluation of screens to produce multi-cycle ±20% amplitude sinusoidal velocity profiles", AIAA 74-623.

[50] Koo, J.-K. and James, D. F., "Fluid flow around and through a screen", *Journal of Fluid Mechanics*, vol. 60, part 3, pp. 513-538, March 1973.

[51] McElwain, B. D., "Unsteady Separation Point Injection for Pressure Recovery Improvement in High Subsonic Diffusers", M.S. thesis, Aeronautics and Astronautics Dept., Massachusetts Institute of Technology, Cambridge, MA, June 2002.

[52] Seifert, A., Eliahu, S., Greenblatt, D. and Wygnanski, I., "On the Use of Piezoelectric Actuators for Airfoil Separation Control", *AIAA Journal*, No. 36, pp. 1535-1537, 1998.

Appendix A

MBDA Inlet Geometric Details

This Appendix presents some geometric details of the MBDA inlet. The dimensions are that of the scaled inlet model, as fabricated and used in the experiments. All dimensions are in mm.

Figure A-1 shows the shape of the inlet entrance, and the points that were used to construct it under Pro/Engineer. All edges are straight. The corners are circular fillets tangent to the adjacent edges. Only the right part of the geometry is shown, as it is symmetrical with respect to the vertical symmetry plane. Table A.1 shows the entrance construction points coordinates in a self-referencing frame. The exit of the inlet is a circle of diameter $D = 137.60mm$.

Figure A-2 shows a cut of the inlet geometry along the vertical symmetry plane, which shows the shape of the upper and lower centerlines. It also gives the notations chosen for the centerlines definition points: L_0 to L_{10} for the lower centerline definition points, and U_0 to U_{10} for the upper centerline definition points. Table A.2 gives the X and Y coordinates of the lower centerline definition points $(L_0, L_1 \ldots, L_{10})$, in a self-referencing frame. Table A.3 gives the X and Y coordinates of the lower centerline definition points $(U_0, U_1 \ldots, U_{10})$, in the same frame.

On table A.4 are reported the cross-sectional area of the inlet at the construction points axial position. Figure A-3 shows 6 intermediary slices of the geometry at equally spaced axial position (X). The subfigures are on the exact same scale. Figure A-3.(g) shows the reference chosen for X.

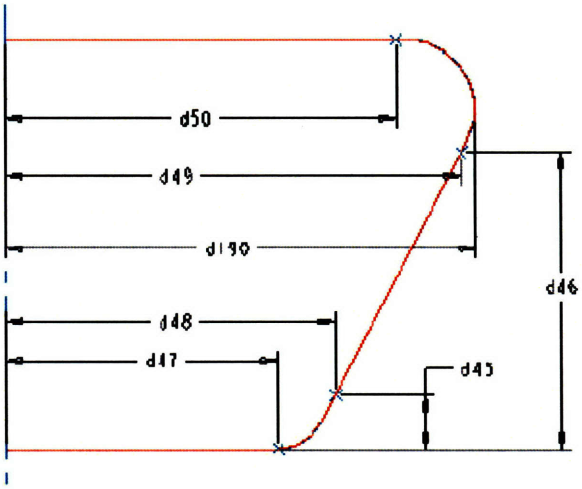
d50
d49
d190
d46
d48
d47
d45

Figure A-1: Trapezoidal entrance definition points

Table A.1: Lower centerline definition points coordinates

dimension	d_{45}	d_{46}	d_{47}	d_{48}	d_{49}	d_{50}	d_{190}
value (mm)	8.86	48.89	44.32	53.77	74.41	63.88	76.81

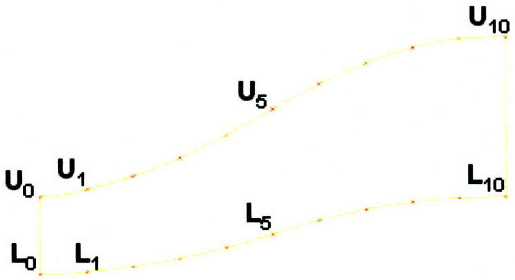
U10
U5
U0
U1
L10
L5
L0
L1

Figure A-2: Centerlines definition points

Table A.2: Lower centerline definition points coordinates

	L_0	L_1	L_2	L_3	L_4	L_5	L_6	L_7	L_8	L_9	L_{10}
X (mm)	0.00	39.78	79.55	119.33	159.11	198.88	238.66	278.43	318.21	357.99	397.76
Y (mm)	0.00	2.29	6.99	14.13	23.57	35.21	47.27	56.49	62.89	66.39	67.34

Table A.3: Upper centerline definition points coordinates

	U_0	U_1	U_2	U_3	U_4	U_5	U_6	U_7	U_8	U_9	U_{10}
X (mm)	0.00	39.78	79.55	119.33	159.11	198.88	238.66	278.43	318.21	357.99	397.76
Y (mm)	67.34	73.71	85.14	100.89	120.24	142.39	164.24	181.81	195.22	202.87	204.50

Table A.4: Cross sectional area as a function of axial distance

X (mm)	0.00	39.78	79.55	119.33	159.11	198.88	238.66	278.43	318.21	357.99	397.76
A (mm^2)	8806.43	9455.21	10259.27	11111.20	11945.78	12724.49	13385.20	13964.10	14519.13	14828.74	14775.07

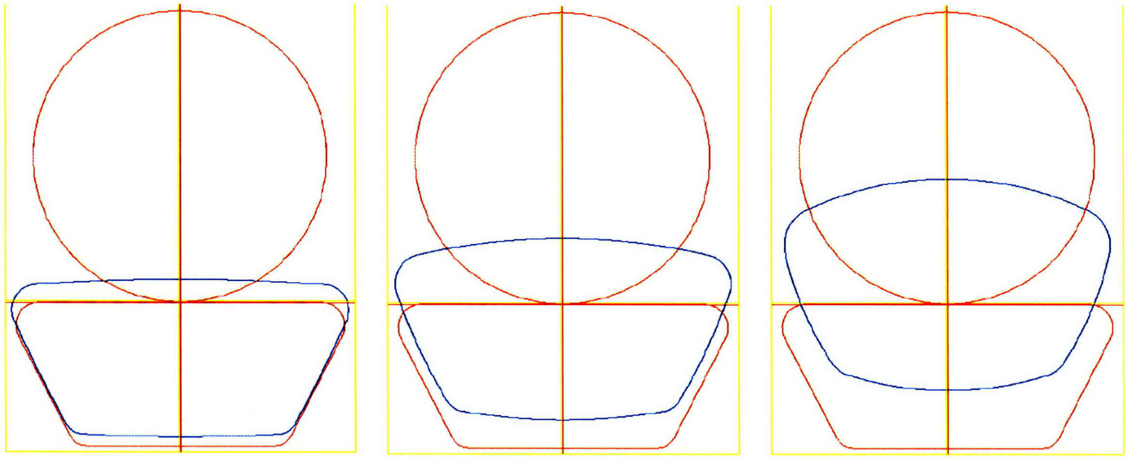

(a) $X = 56.9mm$ (b) $X = 113.8mm$ (c) $X = 170.7mm$

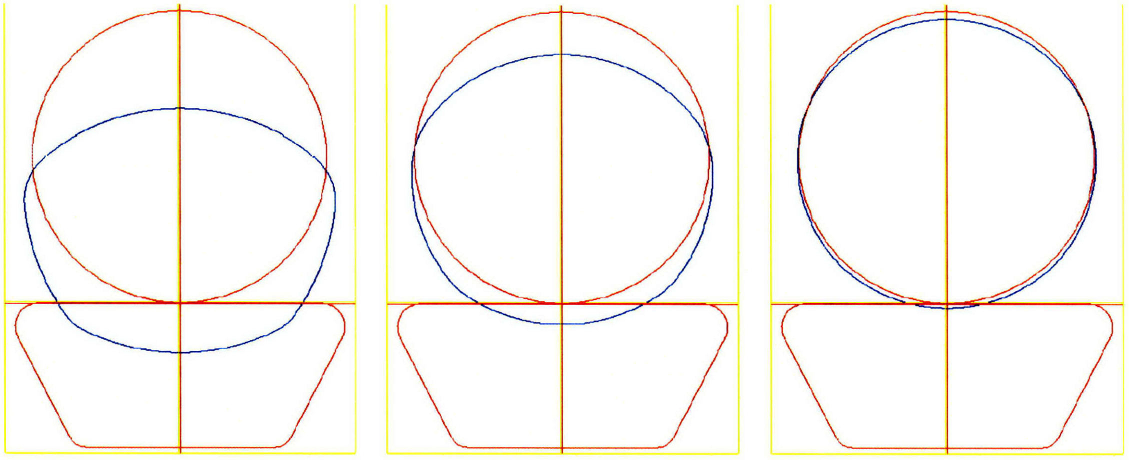

(d) $X = 227.6mm$ (e) $X = 284.48mm$ (f) $X = 341.4mm$

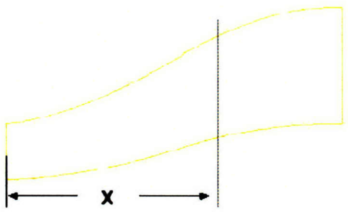

(g) X-reference

Figure A-3: CAD view of 6 intermediary slices of the MBDA inlet geometry

Appendix B

MBDA Presentation

B.1 History

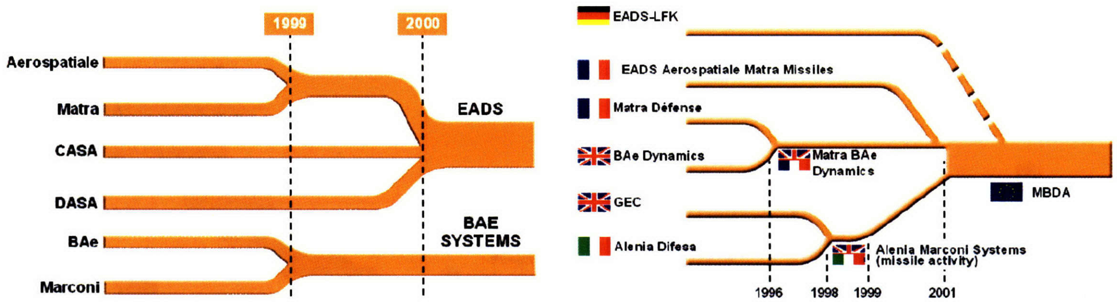
1999
2000
Aerospatiale
Matra
CASA
DASA
BAe
Marconi
EADS
BAE SYSTEMS
EADS-LFK
EADS Aerospatiale Matra Missiles
Matra Défense
BAe Dynamics
Matra BAe Dynamics
GEC
Alenia Difesa
Alenia Marconi Systems (missile activity)
MBDA
1996
1998
1999
2001

(a) Restructuring of the European Aerospace and Defense Industry

(b) Restructuring of the Guided Weapons Industry

Figure B-1: Restructuring of the European Defence Industry

MBDA was definitively created on December 18^{th}, 2001, after a series of mergers of the missile activities of EADS (European Aeronautics Defence and Space company), Finmeccanica (Italian), and BAE (British Aerospace). This unification constituted the first large-scale European merger in the armament and defence sector and was an unavoidable response to the reorganization process of the US defence industry launched in 1994. MBDA then became the world third company in the field of defence, with a more than 2 billions dollars turnover. MBDA's 3 shareholders, EADS, Finmeccanica and BAE, own respectively 37.5%, 25% and 37.5% of MBDA, with equal decision rights.

B.2 Geographical situtation

B.2.1 In the world

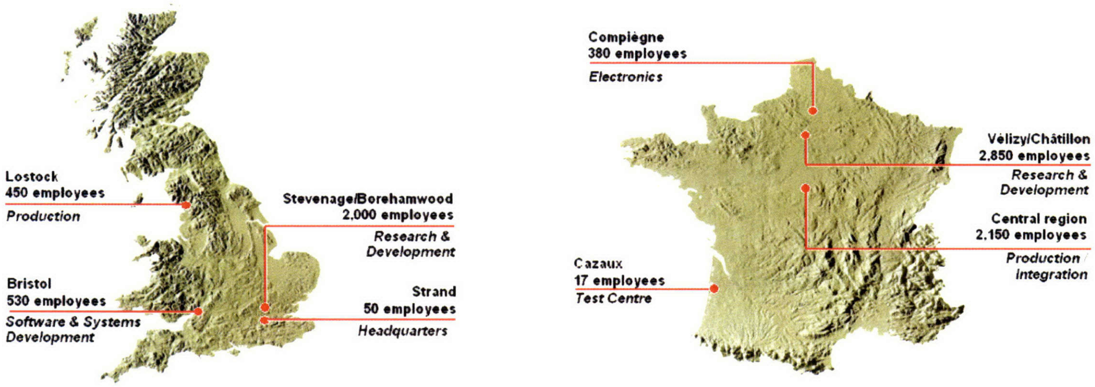
Lostock
450 employees
Production
Bristol
530 employees
Software & Systems Development
Stevenage/Borehamwood
2,000 employees
Research & Development
Strand
50 employees
Headquarters
Compiègne
380 employees
Electronics
Vélizy/Châtillon
2,850 employees
Research & Development
Central region
2,150 employees
Production / Integration
Cazaux
17 employees
Test Centre

(a) MBDA-UK locations (b) MBDA-France locations

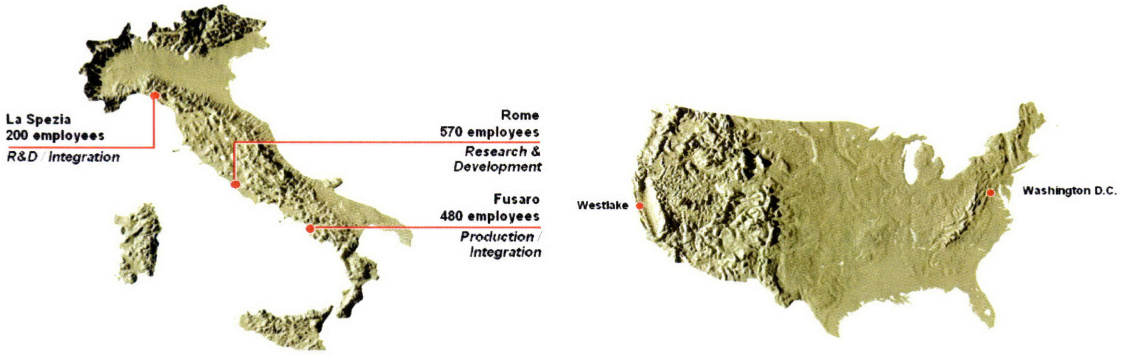
La Spezia
200 employees
R&D / Integration
Rome
570 employees
Research & Development
Fusaro
480 employees
Production / Integration
Westlake
Washington D.C.

(c) MBDA-Italy locations (d) MBDA-USA locations

Figure B-2: MBDA locations

MBDA technological and industrial capacities are spread in three countries:

- France, with 5400 employees,
- Italy, with 1200 employees,
- United Kingom, with 3000 employees.

Each of these countries hosts a research and development center, as well a production site. This organization gives each country some independence from its European partners. Although MBDA is a European company, it is also implanted in the US, in

Washington D.C., where it opened a representation office two years ago, and in Westlake, California, where a factory owned by MBDA-UK employs a hundred persons, in order to establish collaborations with the American industry.

The long term goal is to become a major player in the American defence market, which represents today 50% of the world defence market.

B.2.2 In France

France hosts six sites:

- 2 research and development center, in Vélizy and Châtillon, which employ 2800 persons,
- 2 integration and production centers, in Bourges and Selles-Saint-Denis, which employ 2150 persons,
- a test center in Cazaux, which employs 17 persons.

B.3 Activities

MBDA's main activities are research, development and production of missiles, covering most of the demand in tactical missiles with anti-tank, anti-ship, ground-to-air, air-to-ground air-to-air and nuclear missiles, but also target vehicles and countermeasure systems. MBDA also has a few activities in the civil area.

B.3.1 Anti-tank missiles

The Eryx missile is the first of a third generation anti-tank missiles, and remains without competitors in the world up to this date. It is the only missile that can be fired from a closed space and in any position: lying, on one's knees, standing up or on the shoulder. It is efficient against any armor, any type of building: bunker, blockhaus, entrenched positions...

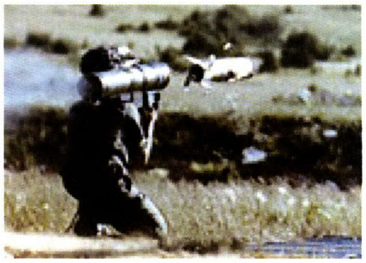

Figure B-3: The Eryx missile

B.3.2 Anti-ship missiles

The Exocet missiles remains one of the most feared anti-ship missiles because of its precision and efficiency. Launched from a ship, a truck, and in its latest version from a submarine, it flies close to the surface at a speed of $1100km.h^{-1}$. It is in service in the French navy and had lots of success in south-eastern Asia and south Europe.

Figure B-4: The Exocet missile

B.3.3 Ground-to-air missiles

The notation “ground-to-air” indicates the environment from which the missile is launched and the environment in (or on) which the target stands. Here, the Aster missile, which has a $70km$ range and maximum flight altitude of $20000m$, is considered as a average range, vertically launched defence system. It was developed by France and Italy, whose armies it equips since 1999.

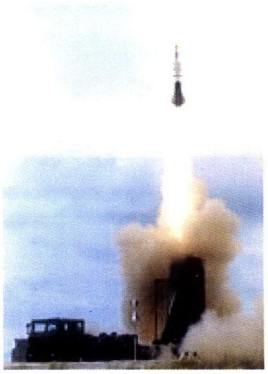
Figure B-5: The Aster missile

B.3.4 Air-to-ground missiles

Figure B-6: The AS30 LASER missile

The AS30 LASER is a weapon designed for the attack of the most defended and armored objectives. Thanks to a auto-guidance system based on the laser-illumination technology, it offers a sub-meter precision. I was largely used during the IRAN/IRAK conflict of 1991, during operation “Desert Storm” and during the 2003 war in Irak. This missile is in service since 1998 and its efficiency is now established.

B.3.5 Air-to-air missiles

The MICA missile, ("Auto-defence and Combat Interception Missile" in French), constitutes the only air-to-air weaponry of the Rafale fighter and of the latest versions of the Mirage 2000 fighter. Two versions of the MICA exist: the MICA-EM, an interception missile guided by an electromagnetic guidance system and the MICA-IR, a short range combat missile guided by an infrared guidance system.

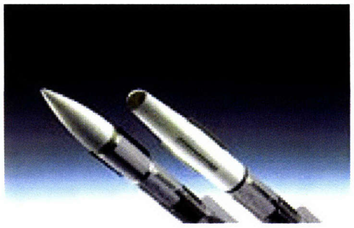

Figure B-7: The MICA-EM and MICA-IR missiles

B.3.6 Nuclear missiles

The ASMP is the French mid-range nuclear missle. It is in service since 1986 on the Mirage IV fighters of the French strategic aerial forces and since 1988 on the Mirage 2000N fighters of the French tactical aerial force. It is currently being adapted to the Super Etendard fighter of the French navy.

Figure B-8: The ASMP nuclear missile

B.3.7 Target vehicles

The C-22 function is to simulate in a realistic manner the diverse aerial threats in order to help in the testing of air-to-air interception systems and to train the military forces. Reusable, it lands using a parachute at the end of its mission. Several C-22 can also fly in formation. In

Figure B-9: The C-22 target vehicle

service since 1992, it has already fulfilled more than 200 flights.

B.3.8 Other products

MBDA production is not limited to missiles. Indeed, MBDA also designs counter-measure systems for aiplaines, decoy systems and missile-alert systems. MBDA also has activities in the civil area: it manufactures certain parts of the Airbus A310 and the ATR AR72-210A, such as the wings, or the landing gears which are manufactured on the Bourges site. It also develops equipments for helicopters such as the Atam Gazelle and the Écureuil.

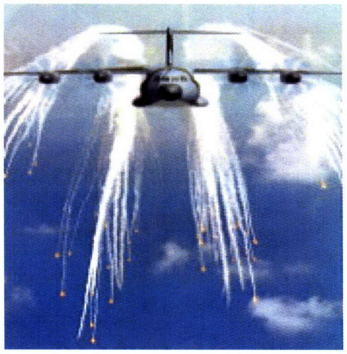

Figure B-10: Counter-measure systems

B.4 Key-figures

Besides satisfying the needs of the European armies, MBDA exports its armament systems all over the world under state control, as can be seen on Fig. B-11.

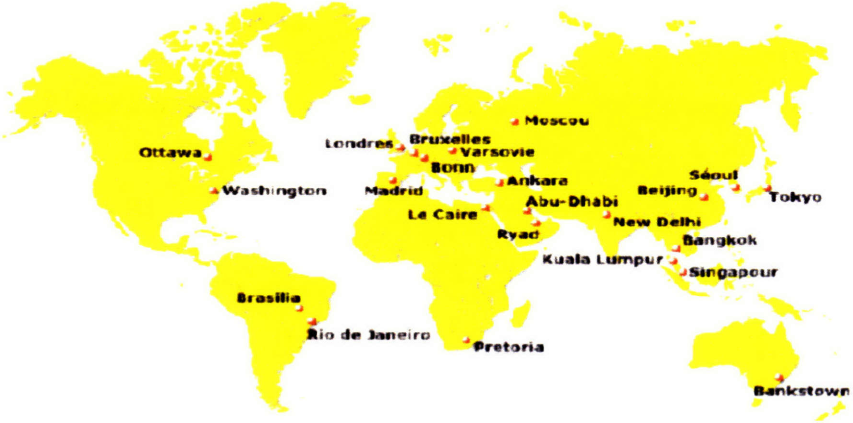
Moscou
Londres
Bruxelles
Varsovie
Ottawa
Bonn
Ankara
Séoul
Washington
Madrid
Abu-Dhabi
Beijing
Tokyo
Le Caire
New Delhi
Ryad
Bangkok
Kuala Lumpur
Singapour
Brasilia
Rio de Janeiro
Pretoria
Bankstown

Figure B-11: MBDA main clients

The defence market is dominated by American companies: However, thanks to

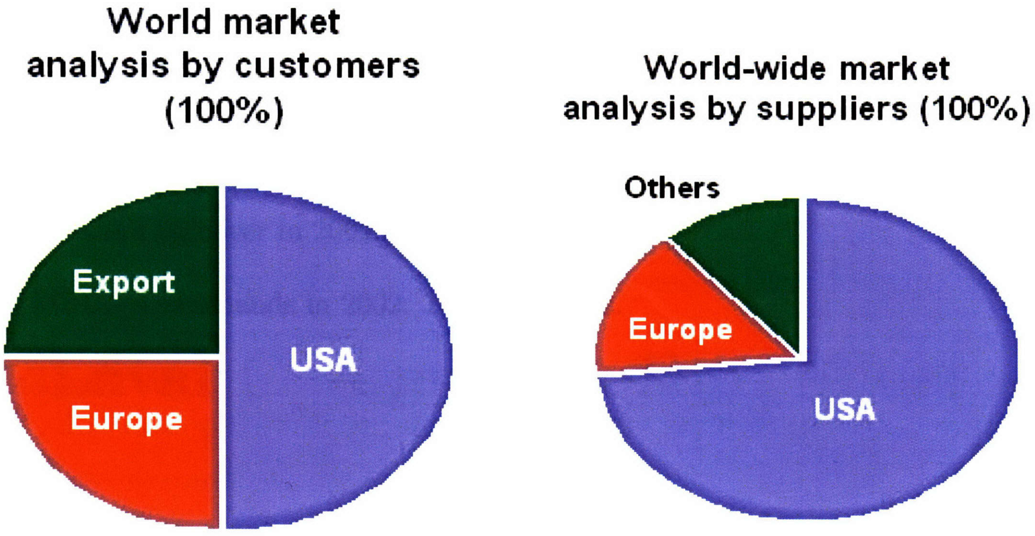

(a) MBDA main clients

(b) MBDA main clients

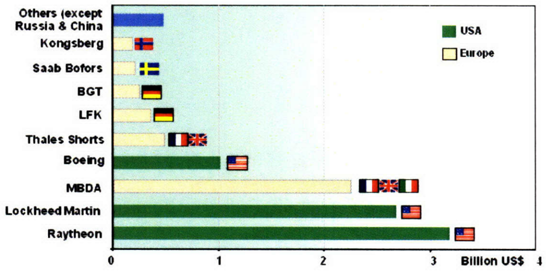

(c) Sales by prime contractor

Figure B-12: The missile market and sales

its great implantation in Europe, MBDA is the world third company in armament production.

A few key-figures:

- Global defence market: ≈ 10 billions €/year for the 2003-2005 period.
- American defence market: ≈ 7 billions €/year.
- American position in the global defence market:
  - 100% of the American market,
  - 70% of the global market,

  - 50 to 60% of the European market.
- European position in the global defence market:
  - 40 to 50% of the European market.
- MBDA's turnover in 2002: 3.3 billions €.
- MBDA's commands in 2002: 13.3 billions €.

Appendix C

DeLaval Compressor Run Sheet

Revised:	03/24/2004
Check Off	8/18/2005

Section 1

- ☐ Call Wright Brothers Wind Tunnel (Richard Perdichizzi ☎3-4924) to coordinate run times.
- ☐ Call Power Plant ☎3-4753 (or ☎3-0963). Tell them you are going to run the 2300 Volt MG Set in Bld. 31.
- ☐ Start Oil Free Compressor if needed (It takes 20-25 minutes to charge tanks up to full pressure).

Ground Floor:

- ☐ Check in and around the MG Set and DeLaval Compressor to ensure they are clear of all junk (especially the shafts).
- ☐ Unlock 25 kV Excitation MG set and MG oil pump electrical boxes.
- ☐ Check the Building DC Breaker is switched on.
- ☐ Check oil level in DeLaval Compressor oil tank. Gauge should align with mark.
- ☐ Check that the breaker is on for the 2 kVA control voltage, on column near men's room.

Motor Generator:

- ☐ Check oil level in MG oil tank. Sight gage should read 1/2 to 3/4.
- ☐ Turn Oil Filter Scraper lever, located on top of the filter, seven full rotations (clockwise).
- ☐ Turn on MG Oil Pump power switch on electrical box.
- ☐ Press start button below electrical box, and listen for the oil pressure switch to click on.
- ☐ Check press 10-15Psi at gage.
- ☐ Check sight gauges for oil flow. Must see good flow before start of MG (Takes 5-10 minutes for good flow).

Basement (Room 0011):

At the DeLaval auxiliary oil pump:

- ☐ Open H_20 Inlet Ball valve on oil pump heat exchanger. Check that the second valve on chill water line is open outside of room.
- ☐ Check H_20 Drain Ball valve on oil pump heat exchanger is open.
- ☐ Switch on pump: Red switch on wall.
- ☐ Turn on Compressor Discharge, Air Cooler Heat Exchanger inlet water valve.
- ☐ Check that the Compressor Discharge Air Cooler Heat Exchanger outlet valve is open.
- ☐ Set DeLaval tunnel butterflies valves as required for the particular experimental program involved. To open or closed positions as necessary.

  Inlet Experiment: 3 Closed, 1 Open
  Supersonic Tunnel: 2 Closed, 2 Open
  Inlet Bell Mouth Test: All Butterflies Closed

Ground Floor:

- ☐ At DeLaval gage panel check oil pressure (9-10Psi).
- ☐ Check all sight gauges for oil flow on the DeLaval Compressor.
- ☐ Plug in Floor Fan for Cooling the Compressor.

Section 2:

Motor Generator:

- ☐ Turn on Ball valve for H_20 cooling for M.G. and DeLaval. Ball valve is on the backflow preventor to the right of the electrical boxes. Check Gate valve on piping near the ceiling should be open.
- ☐ Feel outlet pipes on both heat exchangers for water flow. Should be cold to the touch.
- ☐ Check water pressure at switch on ceiling should be 10Psi.
- ☐ Turn the 25 kV Excitation MG Set coupling over by hand, check that it is free of all obstacles and rotates freely. It is in front of the large MG Set.
- ☐ Turn on exciter gen power switch on electrical box.
- ☐ Press start button and check that the 25 kV Excitation MG set comes up to speed.

At 25 kV Excitation MG Control panel:

- ☐ Set selector switch to #2 position. (2nd floor Console).
- ☐ Adjust 25 kV Excitation rheostats to 250 Volts (Red mark).
- ☐ Turn the 25 kV excitation breaker. Bottom lever to close. (Red Flag indicates the breaker is closed).
- ☐ In 2nd cabinet in the back open door and switch the electrical box lever to on.
- ☐ Check for white light at the 2300-volt switchgear panel.
- ☐ If no white light check that there is DC Voltage at the DC Building breaker box.
- ☐ On Sloan Auto Lab Wall to the left of the door switch both voltage supply boxes to 2300V.

2300 Switch gear panel:

- ☐ At 2300 switch gear panel. Check all phases of the 2300 volts AC via. The switch is on the upper right of the panel.
- ☐ Call Power Plant ☎3-0963 Tell them that building 31 will be switching the 2300-volt service to start the MG set.

☐ Lock all doors.

☐ Check MG set sight gauges for oil flow. If good flow is seen, continue with procedure to start MG, if not wait for good flow indication.

☐ Tip Hg switch inside switchgear panel (1^{st} door on left bottom left of panel). With non-conducting rod flip switch to left should lock and stay in left position.

☐ Turn the motor field rheostat to back to start position.

☐ Press start button to start MG Set. (Lots of noise). MG Set starts on the Starting Breaker, and then, don't be surprised by the Running Breaker slamming closed, listen for it to switch over from the Starting Breaker. If not check the Hg switch and try again.

☐ Adjust Amps to 19.3A using the motor field rheostat. White light goes out.

☐ Check all voltage and current phases.

☐ Adjust 25 kV Excitation rheostats to 250 Volts (Red Mark)

Time: __:__ ☐ Allow MG to warm up 5-10 minutes before starting Compressor.

☐ Observe operation of the unit, including oil flow thru sight gages.

Section 3:

1^{st} Floor: In the 3-stage compressor area.

☐ Check black DeLaval tunnel valve (blue handle) to the GE rig is closed or open as may be the case for the test run.

Inlet Experiment: Closed

☐ Check black DeLaval discharge tunnel valve is open or closed as may be the case for the test run.

Inlet Experiment: Open

1^{st} Floor control console:

☐ Set control to station #2 (Controlled in Cage Area of GE Run Panel)

☐ Fully Open (100%) Bypass Valve using station #2 Controls, and Indicator.

☐ Turn LC switch, on top left of panel, to on position.

☐ Switch on 115 VAC supply (on right of panel).

☐ Turn the generator vernier field rheostat all the way in a clockwise direction to its min position.

☐ Set generator field rheostat to the minimum field position.

This is done by turning the knob clockwise (or lower) direction. When minimum field position is reach the Min. (green light) will turn on.

☐ Set the compressor motor field rheostat to the max field position.

This is done by turning the switch counter-clockwise (or raise) direction until the blue equipment ready light comes on.

☐ Need equipment ready light to run. If no light get help.

☐ Turn generator breaker to close. Should have red flag and lights should change from green to red.

☐ Turn motor breaker to close. Should have red flag and lights should change from green to red.

☐ The DeLaval compressor should now rotate and the Rpm's should read up to a minimum of 400-600Rpm.

The motor voltage should be about 80-100V
The motor current should be about 150-200A

Time: __:__ ☐ Allow Compressor unit to warm up at min speed for five minutes.

☐ Fill out DeLaval Run Sheets during test.

To run DeLaval:

☐ Set Speed.

☐ Close or Open Bypass valve as conditions require.

☐ The compressor speed may be increased by turning the generator main field rheostat control switch in a counter-clockwise direction, or toward its max position which raises the voltage.

Do this a little at time, keeping and eye on the compressor amperage (max 200A). It is slow to respond so give it a little time to react.

Fine adjustment of speed is done by turning the generator venier field rheostat counter-clockwise, remember to turn it back when you go to the next speed setting or you will run out of its adjustment.

You can increase speed higher when you max out generator main field voltage to 415V by turning the compressor motor field rheostat clockwise or toward its min position. There is no fine adjustment so be careful.

Section 4:

Shut Down:

- ☐ Fully Open (100%) Bypass Valve using station #2 Controls, and Indicator.
- ☐ Turn motor breaker to trip position. Should have green flags and lights should change from red to green.
- ☐ Turn generator breaker to closed position. Should have green flag and lights should change from red to green.
- ☐ Turn LC Switch on top left of panel, to off position.
- ☐ Switch off 115V AC supply (on right of panel).
- ☐ Shut down MG Set at white light panel.
- ☐ Trip 25 kV Exciter breaker. Flag should go red to green.
- ☐ Turn breaker inside 2^{nd} cabinet to off position.
- ☐ Press stop button and check that the 25 kV Excitation MG set shuts down.
- ☐ Turn off exciter generator power switch on electrical box and lock.
- ☐ Let oil systems cool approximately 1.5 Hours.

After Cool down:

- ☐ Shut down Oil Lube Pump to MG Set, (and lock electrical box).
- ☐ Turn off Ball valve for H_20 heat exchanger cooling for M.G. Set and DeLaval.
- ☐ Shut down Oil Lube Pump to DeLaval boost pump, and shut the Inlet and Outlet water valves to the Oil Lube pump heat exchanger.
- ☐ Turn off the Compressor Outlet Air Cooler Heat Exchanger inlet water valve.

Appendix D

Matlab Codes and Data Structure

This appendix presents some of the Matlab codes and the data structure used in this project.

D.1 Data structure

After a run, formatted .text files containing the experimental results were generated automatically by the labview interface. For each run, these included:

"run date"_Scani_zero_a.txt : contains the shift-correction calibration results of the 3 Scanivalve DSA units.

"run date"_Scani_zero_b.txt : contains the shift-correction calibration results of the large SCANCO Scanivalve unit.

"run date"_Scani_atm_a.txt : contains the slope-correction calibration results of the 3 Scanivalve DSA units.

"run date"_Scani_atm_b.txt : contains the slope-correction calibration results of the large SCANCO Scanivalve unit.

"run date"_Results_a.txt : contains the data measured by the 3 Scanivalve DSA units during the experiments themselves.

"run date"_Results_b.txt : contains the data measured by the the large SCANCO Scanivalve unit during the experiments themselves.

These data were then processed by a Matlab code, named “data_treatment_BASELINE”, “data_treatment_VGx” or “data_treatment_INJx”, depending on the experiments, and where x is a number between 1 and 3 (three VGs configurations, three injectors). The code “data_treatment_BASELINE” follows and is sufficiently commented. These codes produce a Matlab array of data structures dp“run date” of length the number of operating points measured (inlet mass flow, injection mass flow...) and the following fields:

time: contains the time at which the 3 DSA units took each measurement sample.

Z: contains the 41 IC probes total pressure measurements.

CL: contains the inlet centerline static pressure measurements.

Circum: contains the inlet exit circumference static pressure measurements.

BellCL: contains the bellmouth centerline static pressure measurements.

Bellflg: contains the bellmouth exit flange static pressure measurements.

Inleflg: contains the inlet entrance flange static pressure measurements.

IC: contains the IC static pressure port measurements.

hole_E: contains the IC 5-hole probe center hole total pressure measurement.

hole_C: contains the IC 5-hole probe top hole (in the streamwise direction) total pressure measurements.

hole_D: contains the IC 5-hole probe right hole total pressure measurements.

hole_A: contains the IC 5-hole probe bottom hole total pressure measurements.

hole_B: contains the IC 5-hole probe left hole total pressure measurements.

Comp_in: contains the compressor inlet static pressure measurements.

Comp_out: contains the compressor outlet static pressure measurements.

Tatm: contains the measured atmospheric temperature.

Tin: contains the measured compressor inlet temperature.

RPM: contains the measured compressor rotation speed.

CMF: contains the computed inlet corrected mass flow.

Mach: contains the computed inlet throat Mach number.

recovery: contains the computed AIP pressure recovery.

CpCL: contains the computed inlet centerline static pressure coefficient profile.

CpCircum: contains the computed inlet exit circumference static pressure coefficient profile.

CpBellCL: contains the computed bellmouth centerline static pressure coefficient profile.

DPCP_avg: contains the computed AIP circumferential distortion.

DPRP_max: contains the computed AIP radial distortion.

speed: contains the computed flow velocity at the inlet throat.

Rey: contains the computed Reynolds number at the throat based on the inlet throat hydraulic diameter.

map: contains the index of operating conditions.

D.2 data_treatment_BASELINE code

```
%this script reduces the data obtained on the baseline configuration setup:
    %no screen, no control device, bare inlet. It provides the baseline
    %performances of the S-duct.

    clear dp06_30_04 mean_shift mean_shift_b pressure pressure_b beta_Scani beta_Scani_b alpha_Scani alpha_Scani_b;

    data_treatment_final;

    clear dp06_30_04 mean_shift mean_shift_b pressure pressure_b beta_Scani beta_Scani_b alpha_Scani alpha_Scani_b;

    close all

    gamma=1.4;
    r=287;
    Tref=288.1667; %reference temperature in Kelvin
    Pref=101307.1166; %reference pressure in Pa
    nu=.000014; %air viscosity
    Hd=0.090689; %Hydraulic diameter at the throat in m

    S=load(’../Results/06_30_04Scani_atm_a.txt’);
    Z=load(’../Results/06_30_04Scani_zeros_a.txt’);
    M=load(’../Results/06_30_04Results_a.txt’);

    [sizea sizeb]=size(M);
    Patm=mean(M(:,50));
    Patm06_30_04=convert(Patm,’psi’,’pa’);

    %data format:
    %time 48xpressures PAtm Tatm Pcomin pcompout Tinlet RPM

    Sb=load(’../Results/06_30_04Scani_atm_b.txt’);
    Zb=load(’../Results/06_30_04Scani_zeros_b.txt’);
    Mb=load(’../Results/06_30_04Results_b.txt’);
    [sizeab sizebb]=size(Mb);
```

```
ports([11:15 21:25 31:35 41:45 51:55 61:65 71:75 81:85])=[1:1:40];
%port# dedication
%41 5-hole probe 1
%42 5-hole probe 2
%43 5-hole probe 3
%44 5-hole probe 4
%45 5-hole probe 5
%46 IC wall static pressure probe
%47 Comp in
%48 Comp out

clear alpha_Scani mean_shift pressure dp06_30_04;

%computation of alpha_Scani
mean_shift=mean(S(301:400,2:49));
var_shift=sqrt(var(S(301:400,2:49)));
std_shift=sqrt(var(S(301:400,2:49)));
mean_zero=mean(Z(:,2:49));
var_zero=sqrt(var(Z(:,2:49)));
std_zero=sqrt(var(Z(:,2:49)));

mean_shift_b=-mean(Sb(13:14,39));
var_shift_b=sqrt(var(Sb(13:14,39)));
std_shift_b=sqrt(var(Sb(13:14,39)));
mean_zero_b=mean(Zb(:,:));
var_zero_b=sqrt(var(Zb(:,:)));
std_zero_b=sqrt(var(Zb(:,:)));

Z=[];

for i=1:48
alpha_Scani(i)=Patm/(mean_shift(i)-mean_zero(i));
beta_Scani(i)=Patm-alpha_Scani(i)*mean_shift(i);
end;

for i=1:38
alpha_Scani_b(i)=Patm/(mean_shift_b-mean_zero_b(i));
beta_Scani_b(i)=Patm-alpha_Scani_b(i)*mean_shift_b;
end;

for i=1:48 pressure(:,i)=M(:,i+1)*alpha_Scani(i)+beta_Scani(i); end;

for i=1:38 pressure_b(:,i)=Mb(:,i)*alpha_Scani_b(i)+beta_Scani_b(i); end;

%conversions
pressure=convert(pressure+Patm,'psi','pa');
pressure_b=convert(pressure_b+Patm,'psi','pa');
M(:,50)=convert(M(:,50),'psi','pa');

for i=1:24
```

```
%measures:

K=1+100*(i-1);
L=100*i;

Kb=1+2*(i-1);
Lb=2*i;

pres=mean(pressure(K:L,:))/Patm06_30_04;
pres_b=mean(pressure_b(Kb:Lb,:))/Patm06_30_04;

dp06_30_04(i).time=M(K:L,1);

for j=1:8
Z(6:-1:2,j)=(pres((j-1)*5+1:j*5))';%building the pressure map in the can
end

Z(1,:)=pres_b(34);%probe at the center of the can

dp06_30_04(i).Z=Z;
dp06_30_04(i).CL=pres_b([1 2 4 5 7:18]);
dp06_30_04(i).Circum=pres_b([19:26]);
dp06_30_04(i).BellCL=pres_b([27:33]);
dp06_30_04(i).Bellflg=pres(41);
dp06_30_04(i).Inleflg=pres(42);
dp06_30_04(i).IC=pres(43);
dp06_30_04(i).hole_E=pres_b(34);
dp06_30_04(i).hole_C=pres_b(35);
dp06_30_04(i).hole_D=pres_b(36);
dp06_30_04(i).hole_A=pres_b(37);
dp06_30_04(i).hole_B=pres_b(38);
dp06_30_04(i).Comp_in=pres(47);
dp06_30_04(i).Comp_out=pres(48);
dp06_30_04(i).Tatm=mean(M(K:L,51));
dp06_30_04(i).Tin=mean(M(K:L,54));
dp06_30_04(i).RPM=mean(M(K:L,55));

%computations:
[CMF Mach]=Bell_CMF(pres(41)*Patm06_30_04,Patm06_30_04);
dp06_30_04(i).CMF=CMF;
dp06_30_04(i).Mach=Mach;

dp06_30_04(i).recovery=(sum(sum(Z(2:6,:)))+Z(1,1))/41;

dp06_30_04(i).CpCL=(dp06_30_04(i).CL-dp06_30_04(i).Bellflg)/(1-dp06_30_04(i).Bellflg);
dp06_30_04(i).CpCircum=(dp06_30_04(i).Circum-dp06_30_04(i).Bellflg)/(1-dp06_30_04(i).Bellflg);
dp06_30_04(i).CpBellCL=(dp06_30_04(i).BellCL-dp06_30_04(i).Bellflg)/(1-dp06_30_04(i).Bellflg);

[DPCP_avg,DPRP_max] = distortion_descriptors(dp06_30_04(i).Z);
dp06_30_04(i).DPCP_avg = DPCP_avg;
dp06_30_04(i).DPRP_max = DPRP_max;
```

```
speed = Mach*sqrt(gamma*r*Tref/(1+(gamma-1)/2*Mach^2)); %speed at throat
dp06_30_04(i).speed = speed;
dp06_30_04(i).Rey = speed*Hd/nu;
%dp06_30_04(i).rop=(max(dp06_30_04(i).rake5_outer)-min(dp06_30_04(i).rake5_outer))*100;

end

disp('BASELINE: bare inlet, no screen, no control device')
disp(' ')
disp('Results obtained on June 16th, 2004')
disp(' ')
%reorder for increasing Mach number (and CMF)
mi = [20 19 7 8 18 9 17 10 16 11 5 12 6 13 14 4 15 21 22 23 3 24 2 1];
dp06_30_04=dp06_30_04(mi);
```

D.3 Bell_CMF code

The Bell_CMF functions computes the inlet Corrected Mass Flow and the inlet throat Mach number using the calibration curve saved in CalibPoly.mat.

```
function [CMF,Mach]=Bell_CMF(Ps,Patm)
%this function computes the Corrected Mass Flow and the Mach
%using the calibration curve saved in CalibPoly.mat

gamma=1.4;

load 'D:\Fichiers\Work files \Matlab\CalibPoly.mat';

[n1 n2]=size(p);
n=n2-1;

PR=Ps./Patm;

Mach=sqrt(2/(gamma-1)*(PR.^((1-gamma)/gamma)-1));

CMF=p(1);
for i=1:n
CMF=PR.*CMF+p(i+1);

end;
```

D.4 distortion_descriptors code

This function computes the $DPCP_{avg}$ and the $DPRP_{max}$ of a total pressure AIP map Z.

```
function [DPCP_avg,DPRP_max] = distortion(Z)

recovery = (sum(sum(Z(2:6,:)))+Z(1,1))/41;

%Z(j,i) is the value of the Total pressure read by the probe on angular
%location j and ring i.
Z=Z([2:6],:);

for i=1:5

a=[0:8]*45;
b=Z(i,:);
b(9)=b(1);

da = a(length(a))-a(1);

PAV(i) = trapz(a,b)/da;

theta=[];
for j=1:length(b)-1
if (PAV(i)¡max([b(j) b(j+1)]))*(PAV(i)¿min([b(j),b(j+1)]))
theta=[theta interp1([b(j) b(j+1)],a([j j+1]),PAV(i))];
end
end

theta_min = min(theta);
theta_max = max(theta);
dtheta = theta_max - theta_min;

a_low = [theta_min a(floor(theta_min/45)+2:floor(theta_max/45)+1) theta_max];
b_low = [PAV(i) b(floor(theta_min/45)+2:floor(theta_max/45)+1) PAV(i)];

PAVLOW(i) = 1/dtheta*trapz(a_low,b_low);

extent(i)=theta_max-theta_min;
PAV(i);
PAVLOW(i);
Intensity(i)=(PAV(i)-PAVLOW(i))/PAV(i);
DPRP(i) = (recovery-PAV(i))/recovery;

end

DPCP_avg = mean(Intensity);

DPRP_max = max(DPRP);
```

D.5 make_map code

This functions plots the total pressure map obtained from the total AIP pressure measurements Z.

```
function make_map(Z)

close

Z(1,:)=Z(1,1);

%definition of cylindrical coordinates of probes locations

R=1;
radius=[0.01 0.3123 0.5562 0.7124 0.8390 0.9486]*R;

angle=[2 1 0 -1 -2 -3 -4 -5]*pi/4.;

%definition of x and y coordinates of probes locations

for j=1:length(angle)
for i=1:length(radius)
X(i,j)=radius(i)*cos(angle(j));
Y(i,j)=radius(i)*sin(angle(j));
end;
end;

counter=length(angle)+1;

for i=1:length(radius)
X(i,counter)=X(i,1);
Y(i,counter)=Y(i,1);
Z(i,counter)=Z(i,1);
end

figure(1)
h1=pcolor(X,Y,Z);
shading interp
%h=surf(X,Y,Z,'FaceColor','flat');
colormap(jet)
caxis([0.8 1.])
colorbar
axis off
return
hold on

%cosmetics:

d=1;
```

```
r(6)=R;

N=41;
As=R2̂*pi/N;

for i=1:5
r(i)=sqrt(As*d/pi);
d=d+8;
end;

t(1:9)=2;

theta=[0:2*pi/100:2*pi];
beta=[2*pi/16:2*pi/8:30*pi/16];

%xlim([-R R]*1.05);
%ylim([-R R]*1.05);

%draw the circles encomprising the sections of same area As

for i=1:6
circle(i).x=r(i)*cos(theta);
circle(i).y=r(i)*sin(theta);
T(1:length([circle(i).y]))=2;
plot3([circle(i).x],[circle(i).y],T,’.b’,’MarkerSize’,1)%,’LineWidth’,1);
end;

%draw the lines encomprising the sections of same area As

for i=1:7
line(i).x=[-R*cos(beta(i)):2*R*cos(beta(i))/100:R*cos(beta(i))];
line(i).y=[-R*sin(beta(i)):2*R*sin(beta(i))/100:R*sin(beta(i))];
T(1:length([line(i).y]))=2;
plot3([line(i).x],[line(i).y],T,’.b’,’MarkerSize’,1)%,’LineWidth’,1);
end

%place the points corresponding to the 40 total pressure probes
%numr=’012345’;numt=’12345678’;

for i=2:length(radius)
plot3(X(i,:),Y(i,:),t,’+r’);
end

plot3(0,0,0,’+r’);

hold off
```